NMR AND COMPUTATIONAL STUDIES OF PARAMAGNETIC COMPOUNDS

By

YIZHE DAI

A thesis submitted to the Graduate Program in Chemistry

in conformity with the requirements for the

Degree of Master of Science

Queen's University

Kingston, ON, Canada

October, 2017

Abstract

Unlike diamagnetic compounds, paramagnetic samples are more difficult to study by NMR because they usually exhibit wide chemical shift ranges and broadened signals. These peculiar features are mainly due to the strong hyperfine interactions between magnetic dipoles of unpaired electrons and nuclei. In order to understand experimentally observed NMR signals from paramagnetic molecules, quantum chemical calculations are often desirable. This thesis focuses on two areas of NMR studies of paramagnetic compounds. First, we have examined solution-state ^{1}H, ^{13}C, and ^{17}O NMR spectra of several small paramagnetic vanadium compounds and established the validity of DFT computational approaches for calculating hyperfine shifts on ^{1}H, ^{13}C, and ^{17}O nuclei. We then attempted to study a protein (transferrin) containing V(III) ions by ^{17}O NMR. Second, we used the solid-state NMR data for paramagnetic $Cu(DL\text{-}alanine)_2 \cdot H_2O$ reported in the literature to evaluate a periodic DFT code BAND in computing hyperfine coupling tensors in solids. This is the first time that this kind of test for BAND is carried out for molecular solids.

Acknowledgements

I would like to express my gratitude and appreciation to my supervisor, Dr. Gang Wu for all his assistance and suggestions. It was a great pleasure to work with him. Without his supervision it would be very difficult for me to work on this project. I would also like to thank Dr. Francoise Sauriol for her great help on the NMR experiments and equipment. I also feel grateful to the Center for Advanced Computing (CAC) for the platform they have been provided to use the licensed computational software products I needed. Moreover, I appreciate a lot the generous help from their kind staff, especially Dr. Hartmut Schmider, who had answered my numerous questions by email. I have treasured the wonderful time of working together with the other members in Dr. Wu's group.

I also have to thank the members from Dr. Suning Wang and Dr. Guojun Liu's groups. They were always ready to help when I had problems with the chemicals and the equipment. I could also not forget the guidance and foundations that some previous group members provided.

Finally, I extend my greatest gratitude to my parents. They always believe in me and support my decisions. I also would like to thank my boyfriend. It is impossible for me to finish my study without their mental support.

Table of Contents

Abstract..... II

Acknowledgements III

Table of Contents IV

List of Tables..... VIII

List of Symbols and Abbreviations IX

Chapter 1 Introduction 1
1.1 Overview 1
1.2 A Brief Historical Review of NMR Studies of Paramagnetic Compounds 3
1.3 Organization of the Thesis 8

Chapter 2 NMR theory and Computational Details 9
2.1 Fundamental NMR Theory 9
2.1.1 Nuclear Spins and NMR Signals 9
2.1.2 Relaxations 12
2.1.3 Nuclear Spin Interactions 15
2.1.3.1 The Dipolar Interaction 15
2.1.3.2 The Indirect Spin-Spin Interaction 18
2.1.3.3 Chemical Shift 19
2.1.3.4 The Quadrupolar Interaction 21
2.1.3.5 The Hyperfine Interaction 24
2.2 Basic NMR Spectroscopy 25
2.2.1 Rotating Frame and FID 25
2.2.2 Basic NMR parameters 27
2.2.3 Solution-state NMR 29
2.2.4 Solid-state NMR 31
2.2.4.1 Magic Angle Spinning 32
2.2.4.2 Cross Polarization 33
2.3 Basic Concepts of Paramagnetic NMR Spectroscopy 35
2.3.1 Hyperfine Shifts 35
2.3.2 Relaxation Effects 38
2.4 Computational Details 41
2.4.1 Fundamental Paramagnetic NMR Parameters 41

2.4.2 Quantum Chemical Calculation Software Products 43
2.4.2.1 Basis Sets 44
2.4.2.2 Density Functional Theory 47
2.4.2.3 Algorithms of Hyperfine A-tensor Calculation for Periodic Systems 49
2.4.2.4 Features in BAND for A-tensor Calculations 53

Chapter 3 NMR Studies of Paramagnetic Vanadium Compounds in Solution 56
3.1 Overview 56
3.2 Experimental and Computational Details 59
3.2.1 Preparation of Small Vanadium Compounds 60
3.2.2 Preparation and Characterization of Transferrin Samples 62
3.2.3 Computational Details 66
3.3 Results and Discussion 66
3.3.1 Small Vanadium Compounds 66
3.3.2 Transferrin 78
3.4 Conclusions 80

Chapter 4 NMR Studies of Paramagnetic Compounds in the Solid State 82
4.1 Overview 82
4.2 Computational Details 83
4.3 Results and Discussions 84
4.4 Conclusion 90

Chapter 5 Conclusions and Future Work 91

References 94

Appendix I Calculated Anisotropic A-tensor Components of vanadium compounds A-1
Appendix II Chemical shifts vs. 1/T plots of variable temperature solution-state NMR experiments A-4
Appendix III Calculation results of A_{iso} of Cu(DL-Alanine)$_2$·H_2O A-7
Appendix IV Calculation Results of Anisotropic A-tensor components of Cu(DL-Alanine)$_2$·H_2O A-10

List of Figures

Figure 1. Structure of hemoglobin (left) and the iron binding group (right). (Figures are reproduced from https://en.wikipedia.org/wiki/Hemoglobin). 2
Figure 2. EPR spectrum of $[NH_4]$*trans*-$[RuCl_4(DMSO)_2]$ in the solid state at -160°C (left)[4] and ^{1}H NMR spectrum of $Ni(MeCP)_2$(right).[5] 3
Figure 3. Illustration of PRE and PCS effects in ^{1}H solution-state NMR spectra.[32] 5
Figure 4. Solid state CPMAS ^{13}C NMR spectra of degraded orgnosolv lignin.[43] 6
Figure 5. Experimental (21.1T) and simulated spectra of static (upper) and MAS (lower) ^{17}O solid-state NMR for $K_3V([^{17}O_4]oxalate)_3 \cdot 3H_2O$.[44] 6
Figure 6. Nuclear Zeeman sublevels of ^{1}H and ^{27}Al. 10
Figure 7. Precession of a spin and the two energy states. 11
Figure 8. The recovery of M_z after 90° pulse over time. 13
Figure 9. The loss of $M_{x\text{-}y}$ after 90° pulse. 14
Figure 10. T_1 and T_2 as a function of correlation time (average time cost for molecules to rotate one radian).[52] 14
Figure 11. Geometry of the dipole-dipole interaction. 16
Figure 12. Simulated powder NMR spectrum of a homonuclear system. 18
Figure 13. Description of relative positions across a NMR spectrum. 20
Figure 14. Powder spectra with different CSA tensors (a) low symmetric case (b) axial symmetric case with $\kappa = 1$ (c) axial symmetric case with $\kappa = -1$. 21
Figure 15. Origin of quadrupole moments and EFG. 22
Figure 16. Frequency shifts from the quadrupolar interaction for spin-1 nuclei (left) and first and second order perturbations on the energy levels of spin-3/2 nuclei (right). 23
Figure 17. Simulated solid-state ^{27}Al (I = 5/2) NMR spectra with various η and C_Q values. (Figures are reproduced from http://mutuslab.cs.uwindsor.ca/schurko/ssnmr/ssnmr_schurko.pdf) 24
Figure 18. Magnetization vectors in lab frame (left) and in rotating frame (right). 25
Figure 19. The effect of an RF pulse. 26
Figure 20. Receiving coil and free induction decay. 26
Figure 21. Rotation of magnetization in the y-z plane. (A) At equilibrium; (B) After a 90° pulse; (C) After a 180° pulse. 27
Figure 22. FID (left) and Fourier transformed spectrum (right). 27
Figure 23. One cycle of the RF pulse sequence. 28
Figure 24. General ^{1}H and ^{13}C chemical shift ranges for various chemical functional groups. (Figure was reproduced from https://elearning03.ul.pt/mod/resource/view.php?id=34021) 30
Figure 25. Simulated ^{1}H spectrum of 1,1-dichloroethane. (Figure was reproduced from http://www.chem.ucalgary.ca/courses/350/Carey5th/Ch13/ch13-nmr-5.html) 30
Figure 26. Simulated ^{1}H decoupled ^{13}C spectrum of methyl methacrylate in deuterated chloroform. (Figure was reproduced from

https://chem.libretexts.org/Textbook_Maps/Organic_Chemistry_Textbook_Maps)..... 31
Figure 27. Geometric map of a spinning sample tube. 33
Figure 28. Magnetization and pulse in spin-locking process. 34
Figure 29. The pulse sequence for the CP experiment.[53] 35
Figure 30. STO-3G basis set (left) and a DZP basis set (right) for carbon atoms formatted in Gaussian software style. The first column represents ζ, and the second column are c_i's. 45
Figure 31. An example of the BAND A-tensor calculation output from the gradient approach. 54
Figure 32. An example of the BAND A-tensor output from the density approach. (a) A_{iso} list in a.u. (b) Output section for the traceless part. 55
Figure 33. Plane (left) and stereo (right) structure views of (a) $V(III)(acac)_3$ (b) $V(III)Cl_3(THF)_3$ (THFs have axial and equatorial types) (c) $V(III)Cl_3(MeCN)_3$(MeCNs have axial and equatorial types) (d) $V(IV)O(acac)_2$. 57
Figure 34. (a) Crystal structure of ovotransferrin. (b) Binding site in the N lobe. (c) Binding site in the C lobe. (d) Structure in detail of the N lobe binding site with Fe^{3+} and CO_3^{2-}.[134] 59
Figure 35. UV-vis spectrum of apotransferrin in Tris-HCl buffer solution (pH~7.5). 63
Figure 36. Difference UV spectra upon stepwise addition of Al^{3+} to OTF-HCO_3^- solution (left) and absorbance differences at 240 nm versus molar ratio plot (right). The absorbance of pure Al^{3+} at the same wavelength is also plotted as a slope reference (right). The OTF concentration was around 1μM. 63
Figure 37. Difference UV spectra upon stepwise addition of V^{3+} to OTF-$C_2O_4^{2-}$ solution (left) and absorbance difference at 248.5 nm versus molar ratio plot (right). The OTF concentration was around 10 μM. 65
Figure 38. Plot of signal intensities versus different P1 with PL = 2 dB. 65
Figure 39. ^1H NMR spectra of $V(acac)_3$ in DMSO-d_6. 67
Figure 40. ^{13}C NMR spectra of $V(acac)_3$ in DMSO-d_6. 68
Figure 41. ^{17}O NMR spectrum of $V(acac)_3$ in $CDCl_3$. 68
Figure 42. ^1H (left) and ^{13}C (right) NMR spectra of $VCl_3(THF)_3$ in THF. 68
Figure 43. Mer (left) and fac (right) structures of $VCl_3(MeCN)_3$. 70
Figure 44. ^1H NMR spectra of $VCl_3(MeCN)_3$ in CH_2Cl_2 at (a) room temperature and (b) -35℃. 70
Figure 45. ^{13}C NMR spectrum of $VCl_3(MeCN)_3$ in CH_2Cl_2 at room temperature. 70
Figure 46. ^1H NMR spectra of (a) $VO(acac)_2$ in DMF (b) $VO(acac)_2$ in $CDCl_3$. 71
Figure 47. ^{13}C NMR spectrum of $VO(acac)_2$ in DMF. 72
Figure 48. δ vs. 1/T plot of ^{17}O NMR signal for $V(acac)_3$. 72
Figure 49. δ vs. 1/T plots for ^1H and ^{13}C NMR signals from $V(acac)_3$. 73
Figure 50. Correlation graphs of computational results from G09 with EPR-II (upper) and ADF2016 with jcpl (lower) versus experimental δ results for $V(acac)_3$. 75
Figure 51. Correlation graphs of computational results from G09 (upper) and ADF (lower)

versus experimental δ results for the four compounds shown in Table 8. 76
Figure 52. ^{17}O NMR spectra of OTf-Al^{3+}-$[C_2{}^{17}O_4]^{2-}$ in D_2O under QCT condition on Bruker 600 with (a) 4 times ultrafiltration and (b) 6 times ultrafiltration..... 78
Figure 53. Solid-state ^{17}O NMR spectra of (a) $K_3V(C_2{}^{17}O_4)_3 \cdot 3H_2O$ and (b) OTf-V^{3+}-$[C_2{}^{17}O_4]^{2-}$ obtained at 21.1T. The spectra were obtained by Dr.Victor Terskikh at the National Ultrahigh Field NMR Facility for solids (Ottawa). 80
Figure 54. Molecular structure (left) and crystal structure (right) of Cu(DL-alanine)$_2 \cdot H_2O$ viewing along (A) a axis and (B) c axis.[150] 82
Figure 55. Error of calculated hyperfine shifts in different structure models of Cu(DL-alanine)$_2 \cdot H_2O$.[150] 83
Figure 56. Correlation between experimental vs. computational A_{iso} values for (a) VWN via gradient (b) VWN via density (c) BP86 via gradient (d) BP86 via density. 87
Figure 57. Correlation between experimental vs. computational T_{ii} values for (a) VWN via gradient (b) VWN via density (c) BP86 via gradient (d) BP86 via density. 88

List of Tables

Table 1. Gyromagnetic ratios of some common nuclei and corresponding Larmor frequencies at 14.1T. 11
Table 2. Types of NMR interactions and their typical magnitudes. 15
Table 3. Typical τe values for common paramagnetic systems.[63] 40
Table 4. Absolute shielding constants used in this thesis. 42
Table 5. Frequently used internal basis sets in Gaussian09 and ADF2016. 46
Table 6. Descriptions of common oxidation states of V. 56
Table 7. Testing various computational methods with experimental data obtained for $V(acac)_3$ 74
Table 8. Summary of experimental and computational solution-state NMR results of V compound systems. 77
Table 9. Experimental A-tensor results in MHz obtained from the literature for Cu(DL-alanine)$_2 \cdot H_2O$. 85
Table 10. A summary of slope/R^2 values from correlation graphs for isotropic (A_{iso}) and anisotropic (T_{ii}) A-tensor components. 86

List of Symbols and Abbreviations

Symbols

A	absorbance
$\widehat{A}$	hyperfine coupling tensor
B_o	applied magnetic field
B_1	RF field
C_Q	quadrupole coupling constant
c	speed of light
δ	chemical shift
E	energy
e	charge of electron
ε	molar extinction coefficient
ϵ_0	permittivity of vacuum
η_Q	asymmetry parameter
g	dimensionless magnetic moment
γ	gyromagnetic ratio
$\widehat{\mathcal{H}}$	Hamiltonian
$\hbar$	reduced Planck constant
I	nuclear spin quantum number
k	Boltzmann's constant
M	net magnetization
m	magnetic quantum number
μ	spin magnetic moment
μ_B	Bohr magneton
μ_0	vacuum permeability
ν	Larmor frequency
ω_Q	quadrupole frequency
$\hat{p}$	momentum operator
Q	quadrupole moment
S	total electron spin quantum number
σ	shielding constant
$\hat{\sigma}$	Pauli matrices
T	temperature
$\widehat{T}$	traceless anisotropic hyperfine tensor
T_1	spin-lattice relaxation time
T_2	spin-spin relaxation time
τ	correlation time
τ_e	electron relaxation time
V	potential energy

Abbreviations

AO	Atomic orbital
AQ	Acquisition time
CIF	Crystal information file
COD	Crystallography Open Database
CP	Cross polarization
CS	Chemical shift
CSA	Chemical shift anisotropy
CT	Central transtition
DFT	Density functional theory
EFG	Electric field gradient
EPR	Electron paramagnetic resonance
FID	Free induction decay
FT	Fourier transform
FWHM	Full width at half maximum
GGA	Generalized gradient approximation
GTO	Gaussian-type orbital
LDA	Local density approximation
MAS	Magic angle spinning
MO	Molecular orbital
NMR	Nuclear magnetic resonance
NS	Number of scans
OTF	Ovotransferrin
PAS	Principal axis system
PCS	Pseudocontact shift
PL	Power level
ppm	Parts per million
PRE	Paramagnetic relaxation enhancement
PW	Pulse width
QCT	Quadrupole central transition
RDC	Residual dipolar couplings
RF	Radio frequency
ST	Satellite transition
STO	Slater-type orbital
SW	Sweep width
TD	Number of points
UV	Ultraviolet
XC	Exchange-correlation
ZORA	Zeroth order regular approximation

Chapter 1 Introduction

1.1 Overview

Nuclear Magnetic Resonance (NMR) spectroscopy is an analytical tool which has been widely used in chemical, physical and biological sciences. NMR is a phenomenon in which atomic nuclear spins in a magnetic field absorb and emit electro-magnetic radiation. In chemistry, NMR techniques are powerful ways of obtaining information about molecular structures, dynamics, and chemical activities.

Most chemists use NMR to study diamagnetic compounds where all electrons are paired. Molecules with unpaired electrons exhibit electron paramagnetism. Most common paramagnetic compounds are those containing transition metal centers, such as Fe^{3+} (d^5, high spin S = 5/2, low spin S = 1/2) and Cu^{2+} (d^9, S = 1/2). Paramagnetic molecules are an important clan of compounds that play key roles in many chemical and biological processes. In many reactions, paramagnetic species are formed as intermediates. Many biological macromolecules contain metal ion binding sites. Approximately half of the proteins contain metal ions, which are called metalloproteins. The metalloproteins have many functions, such as storage and transportation. For example, hemoglobin is the principal carrier of oxygen in human bodies.[1] It is a globular protein, and the metal binding site has the structure as illustrated in Fig.1. When hemoglobin has the oxygen atoms attached, the Fe^{2+} ions are in the low spin state which is diamagnetic. However, once the protein loses connection to the oxygen atoms, the Fe^{2+} ions go to the high spin state, which is paramagnetic. The paramagnetism of Fe^{2+} relates to the oxygen

binding states.

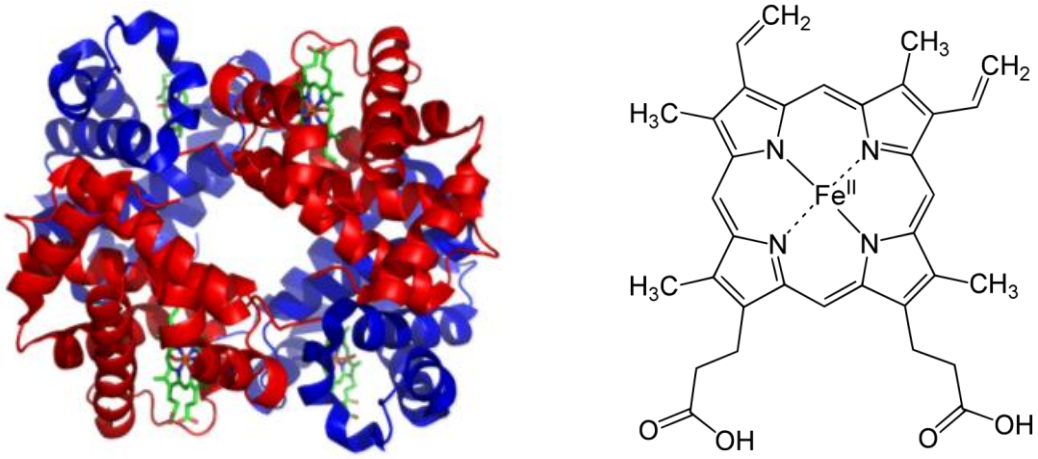

Figure 1. Structure of hemoglobin (left) and the iron binding group (right). (Figures are reproduced from https://en.wikipedia.org/wiki/Hemoglobin.)

The most commonly used technique to study paramagnetic molecules or biomolecules is electron paramagnetic resonance (EPR) spectroscopy. As it is named, EPR signals are from the unpaired electrons in paramagnetic compounds. An example is shown in Fig.2. It follows similar principles with NMR which works on nuclear spins. In some cases, NMR can also be used to study paramagnetic compounds. Among all nuclei with non-zero spin quantum numbers, ^{1}H, ^{13}C, ^{15}N and ^{17}O are most frequently studied. In general, EPR studies are easier than NMR studies. However, in some cases, it is possible to combine them to have a more thorough study on the compounds.[3]

In the context of NMR studies, paramagnetic compounds are much more difficult to study than diamagnetic compounds. The unpaired electrons generate strong hyperfine interactions with nuclear spins, which result in large chemical shifts and great line broadenings for the NMR signals. With such effects, the peaks are hard to assign. Moreover, much more scans

are needed to observe very broad signals. In this case, quantum chemical calculations are always needed to predict, and also to understand the observed NMR signals. Although most NMR studies focus on diamagnetic compounds, applications of NMR to paramagnetic molecules and biomolecules are gaining popularity in recent years.

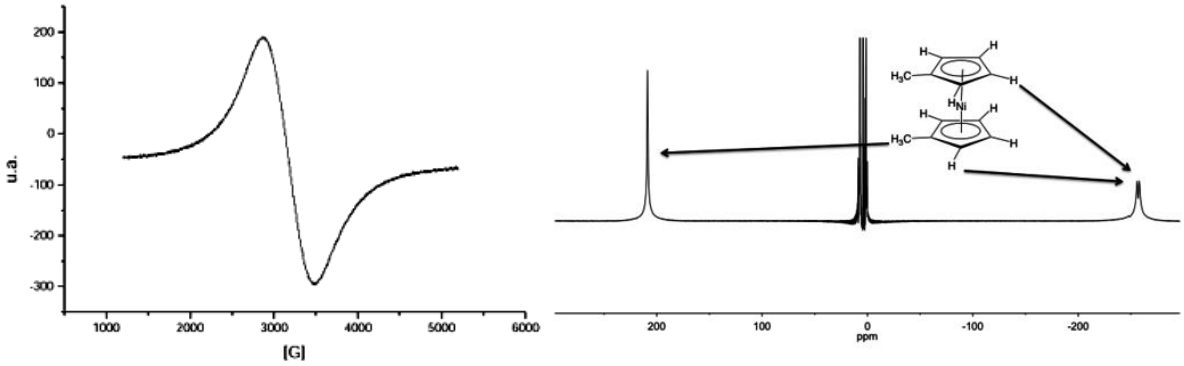

Figure 2. EPR spectrum of $[NH_4]$*trans*-$[RuCl_4(DMSO)_2]$ in the solid state at -160°C (left)[4] and ^{1}H NMR spectrum of $Ni(MeCP)_2$(right).[5]

This thesis is concerned with experimental and computational NMR studies of paramagnetic compounds in both solution and solid states.

1.2 A Brief Historical Review of NMR Studies of Paramagnetic Compounds

The NMR phenomenon was experimentally verified in the late 1940s.[6,7] Shortly after that, the effects that paramagnetic ions brought to solution-state NMR spectra were observed.[8] The early experiments were mainly concerned with the changes in ^{1}H NMR spectra by adding paramagnetic metal ions into H_2O, D_2O and other solutions.[9-15] The early discoveries include the interactions between magnetic moments of unpaired electrons and nuclei,[8-10,13,16,17] and the observed shifts[9-12] as well as relaxation effects.[8,14,17,18] Later, a more comprehensive theory

explaining paramagnetic shifts and relaxations was developed.[19-21]

Paramagnetic NMR has been widely applied to study solutions. For a simple case, by recording the line broadening and the change in shift of a paramagnetic compound relative to a relevant diamagnetic compound, one can obtain information of about the distance between the unpaired electrons and the nuclei. Thus, the molecular structure around the paramagnetic center can be estimated. These effects are known as paramagnetic relaxation enhancement (PRE)[22] and pseudocontact shift (PCS)[23,24], as shown in Fig.3. For example, Gd^{3+} can be used as a PRE probe, while Dy^{3+} is good for PCS to measure nuclei up to 40 Å from the paramagnetic center.[25] The PCS is caused by the anisotropic magnetic susceptibility, which also induces weak alignment of paramagnetic molecules at high magnetic fields. This induces the residual dipolar couplings (RDCs). RDC depends on the relative orientation between the two nuclear spins. Therefore, it can be used as a probe to detect molecular structures and motions. [26,27] In NMR studies of biological molecules, some paramagnetic ions can be incorporated into metalloproteins.[28,29] Such proteins with "paramagnetic tags" can be used as probes. As mentioned in §1.1, these can be used to detect intermediates, especially in some enzymatic reactions. They are also applicable to determine the 3D structures of protein-protein complexes by PCS and RDC.[30] For some proteins, incorporating paramagnetic ions also help to resolve overlapping peaks for the nuclei around the binding sites.[31]

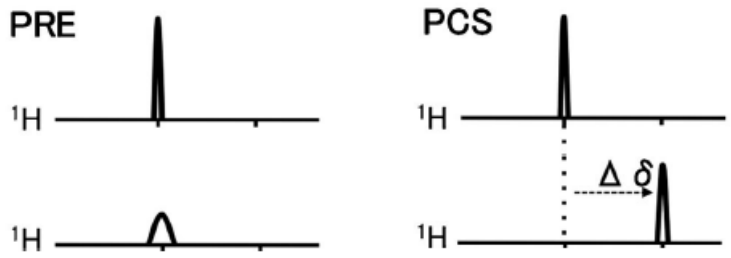

Figure 3. Illustration of PRE and PCS effects in ^{1}H solution-state NMR spectra.[32]

NMR studies of paramagnetic molecules in the solid state are even more challenging. In solid-state, the anisotropic interactions add more difficulties to analyze paramagnetic NMR spectra. Although paramagnetic effects can somehow reduce the relaxation times to accelerate data acquisitions for large biomolecules, the progress of solid-state paramagnetic NMR is rather slow in comparison to solution-state NMR studies. Early works mainly focused on small inorganic molecules.[33-38] Since 2007, solid-state ^{13}C and ^{15}N NMR studies of macromolecules started to appear.[39,40] When dealing with solid-state NMR, some techniques are always needed to minimized part of the anisotropic effects and to strengthen the signals, such as magic angle spinning (MAS)[41] and cross polarization (CP).[42] Fig.4, as an example, shows the effect of MAS through changing the spinning speed.[43] It is clear that with increasing speed of spinning, the side bands are significantly reduced. ^{17}O, a nucleus with a large quadrupolar moment and very low natural abundance, is even more challenging in paramagnetic NMR. The quadrupolar interaction further broadens the NMR peak, and it cannot be completely removed by MAS. ^{17}O NMR always requires very high fields to narrow the quadrupolar broadening. In 2015, it was showed for the first time that ^{17}O NMR signals can be observed from those oxygen atoms directly bonded to the paramagnetic centers.[44] An example is shown in Fig.5. By analyzing the solid-state

NMR spectra, some essential tensors may be obtained such as hyperfine tensors.[45] The tensor components and orientations can contain important structural information, such as symmetry and hydrogen bonding. Solid-state ^{17}O NMR studies of large biomolecules are still on the way.

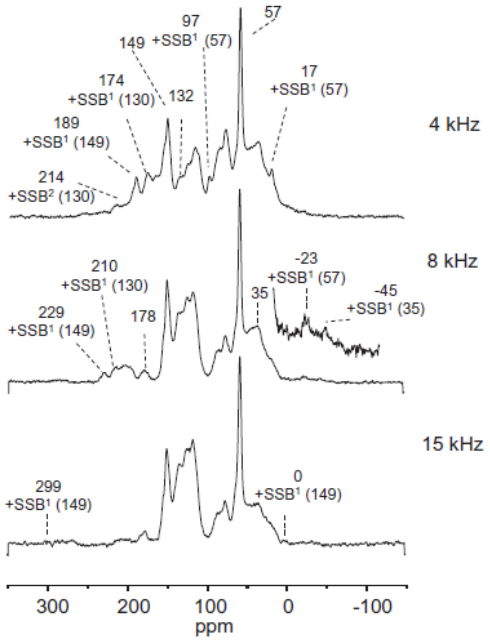

Figure 4. Solid state CPMAS ^{13}C NMR spectra of degraded orgnosolv lignin.[43]

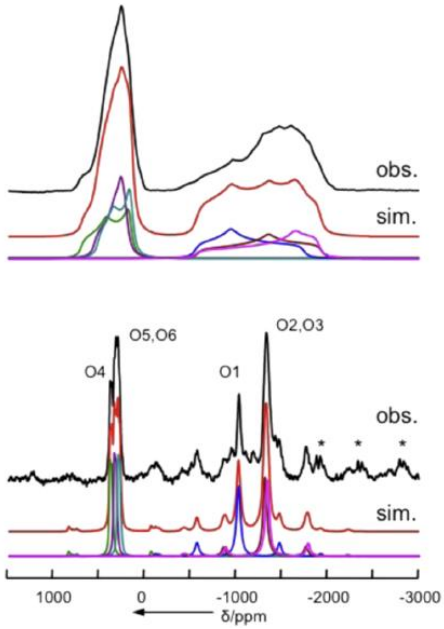

Figure 5. Experimental (21.1T) and simulated spectra of static (upper) and MAS (lower) ^{17}O solid-state NMR for $K_3V([^{17}O_4]oxalate)_3 \cdot 3H_2O$.[44]

Although paramagnetic NMR is a useful technique for study paramagnetic compounds, interpretations or spectra assignments can be challenging. In order to predict and understand such spectra, quantum chemical calculations are necessary in paramagnetic NMR studies. The first nonrelativistic theory for NMR shielding calculations was published by Norman Ramsey in 1950.[46] Several years later, the electron spin Hamiltonian under the effect of nuclei and external magnetic field was derived.[47] It is essential for the calculation of paramagnetic NMR shielding. The formulation of paramagnetic NMR calculations in terms of EPR parameters became complete in 2004.[48] In Vaara's work some relativistic effects were included.[49] In recent years, people have been working on calculating paramagnetic NMR shielding directly, without involving the EPR parameters.[50] Currently most algorithms on paramagnetic shielding and hyperfine tensor calculations used in quantum chemical computational software products are based on hybrid functions of density functional theory (DFT). Computational studies are also important in biomolecular modeling.[51] Computational paramagnetic NMR studies, especially hyperfine tensor calculations, remain as challenges to theoretical chemists and the efforts to improve accuracy are still on-going. In addition, how accurate are DFT calculations in periodic systems is unclear.

Overall speaking, although paramagnetic NMR is difficult, its applications are extending to almost all scientific areas. With the further development of more accurate theoretical treatment, advanced equipment and techniques to aid NMR studies, paramagnetic NMR will have increasing applicability in the future.

1.3 Organization of the Thesis

In this chapter, we have provided brief background information of paramagnetic NMR. In Chapter 2, fundamental NMR theory is explained in detail, including spin systems, relaxation effects and nuclear interactions. Some essential knowledge and techniques of NMR spectroscopy are discussed. Two most important effects in paramagnetic NMR, the hyperfine shift and the relaxation rate, are explained. As the other part of the thesis, some details of quantum chemical computations are introduced, including calculation methods, basis sets, exchange functional and algorithms. In Chapter 3, we focus on solution-state NMR studies of small paramagnetic vanadium compounds and a paramagnetic protein. Experimental procedures are described in detail. ^{1}H, ^{13}C and ^{17}O NMR spectra are reported. Essential parameters are summarized. We also report computational results for comparison and discussion. In Chapter 4 we present a computational solid-state NMR study where we evaluat the accuracy of a periodic DFT code, BAND. By testing the different computational approaches and various exchange functional, we aim to find the optimal method to calculate hyperfine tensors in periodic system. Chapter 5 will provide a summary of conclusion and potential future work.

Chapter 2 NMR theory and Computational Details

2.1 Fundamental NMR Theory

2.1.1 Nuclear Spins and NMR Signals

Spin is an intrinsic non-classical property of all elementary particles. In a simple way, it can be described by its spin quantum number. Usually the nuclear spin quantum number, denoted as *I*, is either an integer (*I* = 0, 1, 2…) or a half integer (*I* = 1/2, 3/2, 5/2…). Isotopes with even atomic mass numbers have integer spins, while those with odd mass numbers have half integer spins. Furthermore, if the isotopes with even mass numbers also have even numbers of protons and neutrons, their *I* values are zero. These isotopes are of no use in NMR studies.

In a strong magnetic field, all spins are quantized. A spin with *I* has a total angular momentum of

$$\left|\vec{I}\right| = \hbar\sqrt{I(I+1)} \tag{1}$$

Assuming the magnetic field is applied along the z axis, the projection of spin angular momentum on the z axis is $I_z = \mathrm{m}\,\hbar$, where m = -*I*, -*I*+1, …, *I*-1, *I* are magnetic quantum numbers. This means a spin with *I* have (2*I*+1) spin quantum states. In the absence of an external magnetic field, all the spin states are degenerate. Once a magnetic field is applied, the degeneracy is broken.

Another intrinsic property of spin is its magnetic moment. The spin angular momentum along the z axis, I_z, and the spin magnetic moment, μ, are related by a constant γ called the

gyromagnetic ratio,

$$\mu = \gamma I_z \tag{2}$$

Table 1 shows a list of gyromagnetic ratios for some common nuclei in NMR. By applying an external magnetic field B_o, the energy levels of the spin system are given by

$$E = -\mu \cdot B_o \tag{3}$$

Assuming the applied magnetic field is along the z axis, then

$$E = -m\hbar\gamma B_o \tag{4}$$

The energy difference between the sublevels is called the Zeeman splitting. Refer to Fig.6 as examples. NMR signals are associated with the nuclear transitions between Zeeman sublevels ($\Delta m = \pm 1$). Therefore, the splitting between two adjacent Zeeman energy levels is

$$\Delta E = \hbar\gamma B_o \tag{5}$$

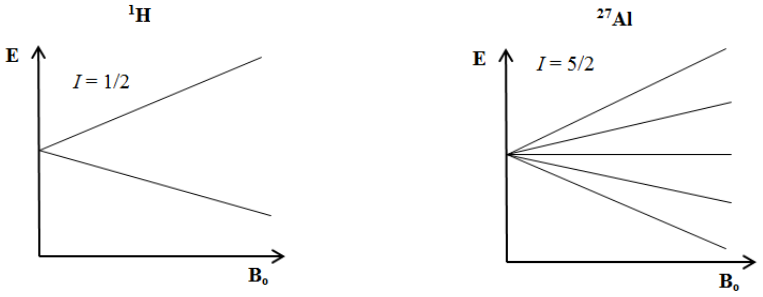

Figure 6. Nuclear Zeeman sublevels of ^{1}H and ^{27}Al.

The resonance frequency (in Hz) can then be expressed as

$$\nu_o = \frac{\Delta E}{h} = \frac{\gamma}{2\pi} B_o \tag{6}$$

This is also called the Larmor frequency, which is the frequency of nuclear spins precessing around the applied magnetic field, as illustrated in Fig.7. Since spins are small magnetic dipoles, they tend to align with the applied field. While a nucleus "spins" around its own axis, it also

rotates around the magnetic field at a fixed angle. This latter rotation is named as precession. A spin with I = 1/2 has two energy levels depending on its direction relative to the magnetic field ($m = \pm\frac{1}{2}$). The lower energy level is the spin aligning with the field.

Table 1. Gyromagnetic ratios of some common nuclei and corresponding Larmor frequencies at 14.1T.

Nuclei	Spin number I	$\gamma(10^6$ rad s^{-1} $T^{-1})$	γ(MHz T^{-1})	ν_o at14.1T(MHz)
^{1}H	1/2	267.513	42.577	600.130
^{2}H	1	41.065	6.536	92.124
^{13}C	1/2	67.262	10.705	150.903
^{14}N	1	19.331	3.077	43.367
^{15}N	1/2	-27.116	-4.316	60.834
^{17}O	5/2	-36.264	-5.772	81.356
^{31}P	1/2	108.291	17.235	242.938

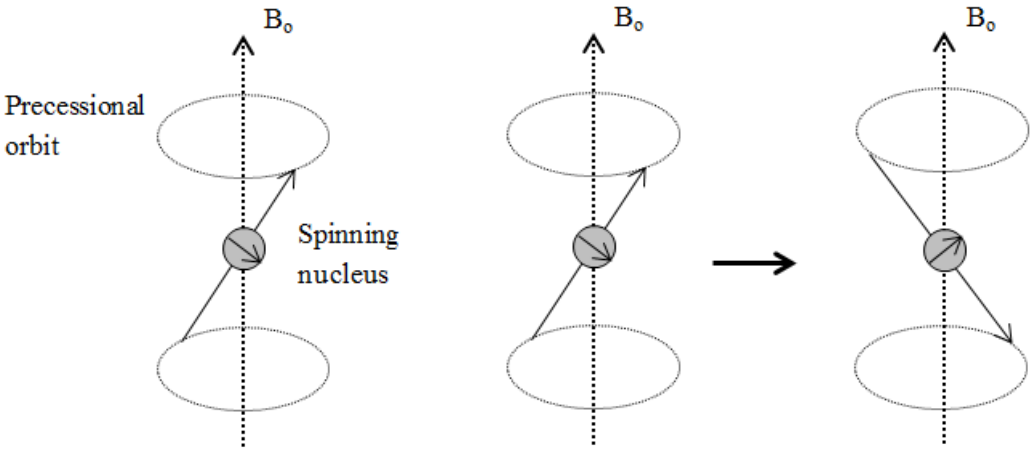

Figure 7. Precession of a spin and the two energy states.

If electromagnetic radiation at the Larmor frequency is applied, a spin would be "flipped" to its higher energy level. Since the Larmor frequencies usually fall into the radio-frequency (RF) range, the pulses in NMR are called RF pulses. If the gyromagnetic ratio γ and the magnetic field strength B_o are known, the pulse frequency can be calculated using Eq.6. Table 1 also shows some common Larmor frequencies at 14.1 T. After a RF pulse excites the spin into its higher energy state, the spin would go through relaxation processes back to the lower energy states over time.

2.1.2 Relaxations

In an external magnetic field, there are more spins occupying the lower energy state than the higher one at thermal equilibrium. The population ratio can be described by the Boltzmann distribution:

$$\frac{N_{higher}}{N_{lower}} = e^{-\frac{\Delta E}{kT}} = e^{-\frac{\gamma B_o}{kT}} \quad (7)$$

If the magnetization is viewed as a vector, this gives a net magnetization along the +z axis. When a RF pulse is applied, the magnetization is disturbed. The recovery of the magnetization along the +z axis is known as the T_1 relaxation, and the loss of magnetization in the x-y plane is known as the T_2 relaxation.

The T_1 relaxation, also called spin-lattice relaxation or longitudinal relaxation, is generally caused by the field fluctuation at the nuclei. The field fluctuation could come from nuclear spin interactions such as dipolar interactions and quadrupolar couplings when they are coupled with molecular motions. The energy released from the relaxation goes into the

surroundings. At the equilibrium, the net magnetization is along the +z axis, and its magnitude is defined as M_o. After a 90° pulse brings the magnetization into the x-y plane, the magnetization along the z axis M_z is zero. The re-growing of M_z, as seen in Fig.8, over time is described by:

$$M_z = M_o(1 - e^{-\frac{t}{T_1}}) \tag{8}$$

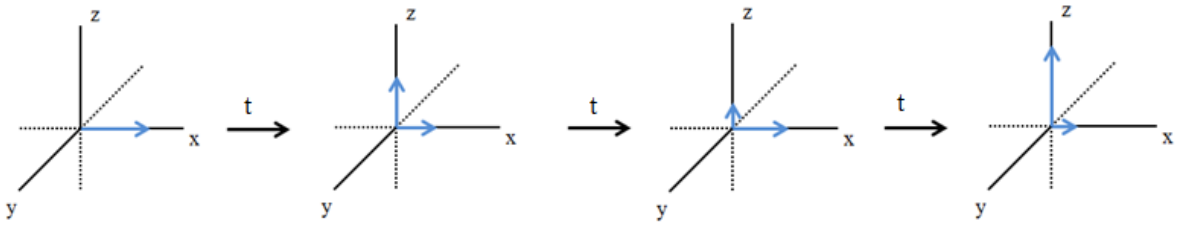

Figure 8. The recovery of M_z after 90° pulse over time.

T_1 usually reaches a minimum when the average rate of molecular motion is around the Larmor frequency. In the liquid state, the rate of small molecular motion is very fast. With a relatively high solvent viscosity or a large molecule size, the molecular motion becomes slower, often resulting in shorter T_1values.

The T_2 relaxation is known as spin-spin relaxation or transverse relaxation. It describes the loss of magnetization coherence, or the decaying of the net magnetization in the x-y plane. Assuming a 90° pulse is applied along the y-axis, the magnetization is brought along the x-axis initially. The nuclear spin interactions would cause different spins to experience different local magnetic fields. Consequently, as depicted in Fig.9, different spins have slightly different Larmor frequencies, and the magnetization dephases over time, in the following fashion:

$$M_{x-y}(t) = M_{x-y}(t = 0)e^{-\frac{t}{T_2}} \tag{9}$$

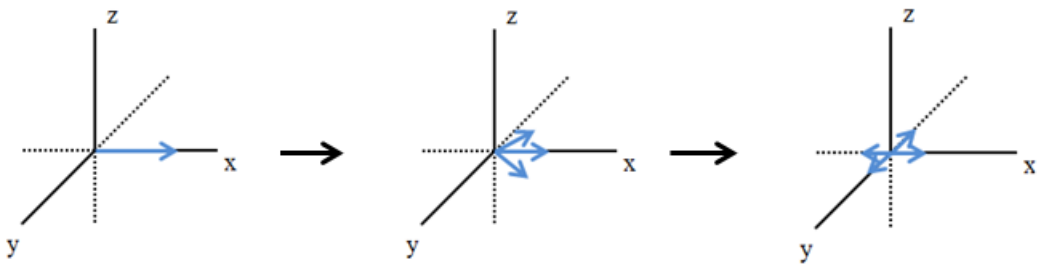

Figure 9. The loss of $M_{x\text{-}y}$ after 90° pulse.

Unlike T_1, T_2 keeps decreasing with the increasing of molecular size as seen in Fig.10. The dephasing of $M_{x\text{-}y}$ is along with the recovery of M_z. After the $M_{x\text{-}y}$ averages out, M_z could still be growing. Therefore, it is not hard to understand that T_2 should always be less than or equal to T_1. It is also worth mentioning that the applied magnetic field is not ideally uniform. The inhomogeneity of B_o also contributes to the spin-spin relaxation, giving a combined time constant called T_2^*. It can be expressed as:

$$\frac{1}{T_2^*} = \frac{1}{T_2} + \frac{1}{T_{2\,\text{inhomo}}} \tag{10}$$

T_2^* is always shorter than T_2.

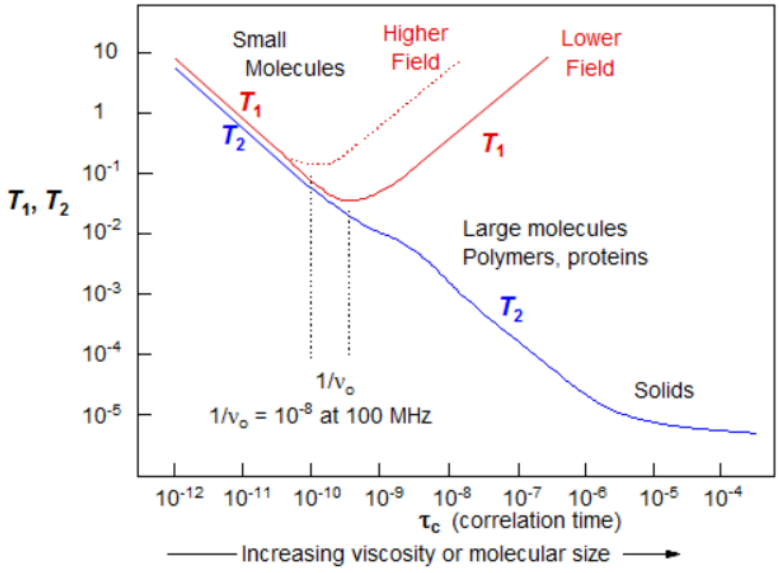

Figure 10. T_1 and T_2 as a function of correlation time (average time cost for molecules to rotate one radian).[52]

2.1.3 Nuclear Spin Interactions

As mentioned in the previous section, the energy levels of nuclei in an external magnetic field display Zeeman splittings. In the context of NMR, the Zeeman interaction contributes most in the energy level differences. Beside this, there are also other types of interactions between nuclear spins between nuclear and electron spins. Table 2 shows the typical orders of magnitude for these nuclear spin interactions. The total NMR Hamiltonian is then written as:

$$\widehat{H} = \widehat{H_z} + \widehat{H_D} + \widehat{H_J} + \widehat{H_{CS}} + \widehat{H_Q} + \widehat{H_{hf}} \tag{11}$$

Table 2. Types of NMR interactions and their typical magnitudes.

Type	Interaction Symbols	Magnitudes
Zeeman interaction	$\widehat{H_z}$	100 MHz
Dipolar coupling	$\widehat{H_D}$	50 kHz
J-coupling	$\widehat{H_J}$	100 Hz
Chemical shift	$\widehat{H_{CS}}$	20 kHz
Quadrupolar interaction	$\widehat{H_Q}$	10 MHz
Hyperfine interaction	$\widehat{H_{hf}}$	100 MHz

2.1.3.1 The Dipolar Interaction

Dipolar coupling is also known as the dipole-dipole interaction. As its name suggests, it describes how nuclear magnetic dipoles influence each other. The dipolar couplings could

come either from homonuclear or heteronuclear dipole-dipole interactions. The potential energy between the two interacting dipoles is written as:[53]

$$V = \frac{\mu_0}{4\pi}\left(\frac{\vec{\mu_1}\cdot\vec{\mu_2}}{r^3} - \frac{3(\vec{\mu_1}\cdot\vec{r})(\vec{\mu_2}\cdot\vec{r})}{r^5}\right) \quad (12)$$

where μ_0 is the vacuum permeability or magnetic constant, and $\vec{r}$ is the vector connecting the two centers of magnetic dipoles, as illustrated in Fig.11. Further in detail, the potential energy is a function of both internuclear distance and angles:[53]

$$V = -\frac{\mu_0\mu_1\mu_2}{4\pi r^3}(3\cos\theta_1\cos\theta_2 - \cos\theta_{12}) \quad (13)$$

where θ_{12} is the angle between two dipoles, and $\theta_{1,2}$ are the angles between dipoles and $\vec{r}$. Clearly, the strength of dipolar interactions depends on both distance and directions. In solution, the dipolar coupling effect is averaged out by fast tumbling motions of the molecules. In solids or liquids of high viscosity, molecules have low mobility so that dipolar couplings will contribute to the shape of spectra.

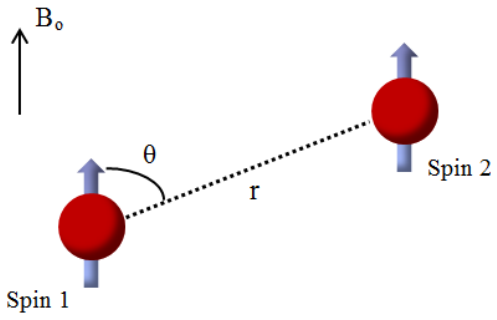

Figure 11. Geometry of the dipole-dipole interaction.

Considering a two-spin system in the solid state, the potential energy of the dipolar coupling is given by Eq.12. To express it quantum mechanically, the Hamiltonian is written as:[53]

$$\widehat{\mathcal{H}}_{\mathrm{dd}} = \gamma_1\gamma_2\hbar^2\left\{\frac{\hat{\boldsymbol{I}}_1\cdot\hat{\boldsymbol{I}}_2}{\mathrm{r}^3} - 3\frac{(\hat{\boldsymbol{I}}_1\cdot\mathbf{r})(\hat{\boldsymbol{I}}_2\cdot\mathbf{r})}{\mathrm{r}^5}\right\}\frac{\mu_0}{4\pi} \tag{14}$$

Expand the equation and put it into polar coordinates, it becomes

$$\widehat{\mathcal{H}}_{dd} = \mathrm{r}^{-3}\gamma_1\gamma_2\hbar^2[\mathrm{A}+\mathrm{B}+\mathrm{C}+\mathrm{D}+\mathrm{E}+\mathrm{F}]\frac{\mu_0}{4\pi} \tag{15}$$

where

$$\mathrm{A} = -\hat{I}_{1z}\hat{I}_{2z}(3\cos^2\theta - 1) \tag{16}$$

$$\mathrm{B} = -\frac{1}{4}[\hat{I}_{1+}\hat{I}_{2-} + \hat{I}_{1-}\hat{I}_{2+}](3\cos^2\theta - 1) \tag{17}$$

$$\mathrm{C} = -\frac{3}{2}\left[\hat{I}_{1z}\hat{I}_{2+} + \hat{I}_{1+}\hat{I}_{2z}\right]\sin\theta\cos\theta\exp(-\mathrm{i}\phi) \tag{18}$$

$$\mathrm{D} = -\frac{3}{2}[\hat{I}_{1z}\hat{I}_{2-} + \hat{I}_{1-}\hat{I}_{2z}]\sin\theta\cos\theta\exp(\mathrm{i}\phi) \tag{19}$$

$$\mathrm{E} = -\frac{3}{4}\hat{I}_{1+}\hat{I}_{2+}\sin^2\theta\exp(-2\mathrm{i}\phi) \tag{20}$$

$$\mathrm{F} = -\frac{3}{4}\hat{I}_{1-}\hat{I}_{2-}\sin^2\theta\exp(2\mathrm{i}\phi) \tag{21}$$

Here $\hat{\boldsymbol{I}} = (\hat{I}_x, \hat{I}_y, \hat{I}_z)$ is the spin operator. $\hat{I}_+ = \hat{I}_x + i\hat{I}_y$ and $\hat{I}_- = \hat{I}_x - i\hat{I}_y$ are the raising and lowering operators. The common factor $\mathrm{R} = \frac{\mu_0\hbar}{8\pi^2}\mathrm{r}^{-3}\gamma_1\gamma_2$ is known as the dipolar coupling constant. Considering only dipolar coupling in a two-spin AX heteronuclear system, the Zeeman energy dominates in the interaction so that the Hamiltonian is:[53]

$$\mathrm{h}^{-1}\widehat{\mathcal{H}}_{dd} = -\left(\nu_{\mathrm{A}}\hat{I}_{Az} + \nu_{\mathrm{X}}\hat{I}_{Xz}\right) - \mathrm{R}\hat{I}_{Az}\hat{I}_{Xz}(3\cos^2\theta - 1) \tag{22}$$

which means the potential energy is:

$$\mathrm{h}^{-1}\mathrm{U} = -(\nu_{\mathrm{A}}\mathrm{m}_{\mathrm{A}} + \nu_{\mathrm{X}}\mathrm{m}_{\mathrm{X}}) - \mathrm{R}\mathrm{m}_{\mathrm{A}}\mathrm{m}_{\mathrm{X}}(3\cos^2\theta - 1) \tag{23}$$

Therefore the transitions of A are:

$$\nu = \nu_{\mathrm{A}} \pm \frac{1}{2}\mathrm{R}(3\cos^2\theta - 1) \tag{24}$$

and so is X. For a homonuclear pair of A's, the Zeeman energy states are same. Then the second term of dipolar coupling expansion also contributes. The Hamiltonian becomes:

$$h^{-1}\hat{\mathcal{H}}_{dd} = -\nu_0(\hat{I}_{1z} + \hat{I}_{2z}) - R(3\cos^2\theta - 1)[\hat{I}_{1z}\hat{I}_{2z} - \frac{1}{4}(\hat{I}_{1+}\hat{I}_{2-} + \hat{I}_{1-}\hat{I}_{2+})] \quad (25)$$

The transitions are:

$$\nu = \nu_0 \pm \frac{3}{4}R(3\cos^2\theta - 1) \quad (26)$$

In a single crystal, the vectors are aligned so θ is the same for all A's. The spectrum of A shows two single lines separated by R for AX and (3/2)R for A_2. In a powder sample, the nuclei are randomly orientated so θ could have any possible value. Then the spectrum of A shows a powder pattern, known as the Pake doublet as shown in Fig.12. The separations are, again, R for the AX system and (3/2)R for the A_2 system.

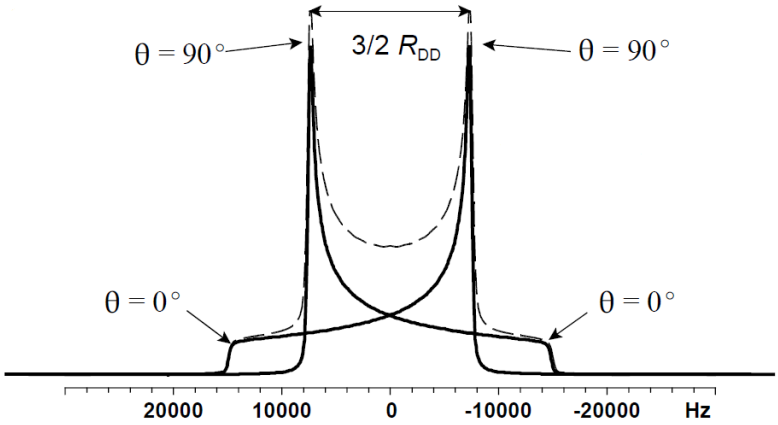

Figure 12. Simulated powder NMR spectrum of a homonuclear system.

2.1.3.2 The Indirect Spin-Spin Interaction

The indirect spin-spin interaction is also called J-coupling. The J-coupling between nuclear magnetic dipoles is through chemical bonds. The spin states of one nucleus affect the bonding electron spins, and hence the neighbouring nucleus is also affected by the bonding electrons. This causes splitting of peaks in NMR spectra. J-coupling constant could be determined from the width of splitting. The J-coupling effect is about 1000 times weaker than the

dipolar coupling, and is field independent. In solution-state NMR, J-coupling provides crucial molecular structural information including bond distances and angles.

2.1.3.3 Chemical Shift

As is known, NMR spectra are plots of absorbance versus frequency. The frequency of a signal on the spectrum is called the chemical shift. In an applied magnetic field, moving electrons produce their own magnetic fields which will slightly alter the field strength at nuclei. In this case nuclei acquire different Larmor frequencies, and thus different chemical shifts. The chemical shift (δ) is defined relative to a reference compound, for ^{1}H and ^{13}C it is tetramethysilane (TMS, $Si(CH_3)_4$). It is independent of the strength of the applied field, and is expressed in parts per million (ppm):

$$\delta = \frac{\nu_{sample} - \nu_{ref}}{\nu_{ref}} \times 10^6 \tag{27}$$

The reference signal is always at 0 ppm as stated. When electrons orbiting around the nucleus, they are described as to provide shielding. As illustrated in Fig.13, shielded nuclei have small chemical shifts in the spectra. Correspondingly, nuclei with large chemical shifts are said to be deshielded.

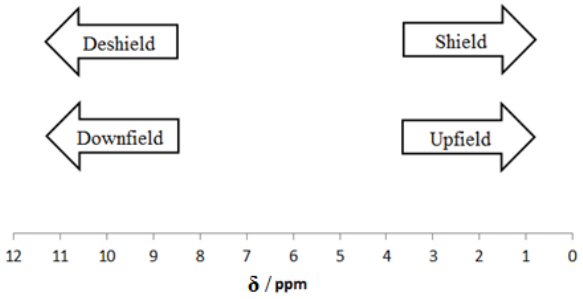

Figure 13 . Description of relative positions across a NMR spectrum.

Similar to dipolar coupling, the shielding that nuclear spins experience are not isotropic. The anisotropic interaction is described by the shielding tensor $\hat{\sigma}$ depending on the molecular symmetry. It is called the chemical shielding anisotropy (CSA). It could be diagonalized into three principal components in the principal axis system (PAS), which is written as:

$$\hat{\sigma}^{\mathrm{PAS}} = \begin{pmatrix} \sigma_{11} & 0 & 0 \\ 0 & \sigma_{22} & 0 \\ 0 & 0 & \sigma_{33} \end{pmatrix} \tag{28}$$

The three components are assigned in the way that $\sigma_{11} \leq \sigma_{22} \leq \sigma_{33}$. There are a few concepts relating to these:

$$\sigma_{\mathrm{iso}} = \frac{1}{3}(\sigma_{11} + \sigma_{22} + \sigma_{33}) = \frac{1}{3}\mathrm{Tr}(\hat{\sigma}) \tag{29}$$

$$\Omega = \sigma_{33} - \sigma_{11} \tag{30}$$

$$\kappa = \frac{\sigma_{\mathrm{iso}} - \sigma_{22}}{\Omega} \tag{31}$$

σ_{iso} is the isotropic shielding constant. In solutions, only the isotropic chemical shielding is observed. Ω is called the span, describing the range of the CSA on the powder spectrum. κ is called the skew, and it describes the asymmetry of the CSA pattern.

If a molecule is spherical symmetric, such as CH_4, the shielding is the same from all orientations so no anisotropic interaction is seen in the ^{13}C spectrum. However, in general spins have asymmetric CSA tensors, as seen in Fig.14 (a). There are also cases when the molecules are axial symmetric like C_2H_2 and $CHCl_3$, as shown in Fig.14 (b) and (c).

In a general case, the observed shielding constant is denoted as σ_{zz}, and it consists of the principal components of CSA:[53]

$$\sigma_{zz} = \sum_{j=1}^{3} \sigma_{jj} \cos^2\theta_j \tag{32}$$

where θ_j is the angle between σ_{jj} and the applied field B_0. Rewrite Eq.32 to include the isotropic term:

$$\sigma_{zz} = \frac{1}{3}\mathrm{Tr}(\hat{\sigma}) + \frac{1}{3}\sum_{j=1}^{3} \sigma_{jj}(3\cos^2\theta_j - 1) \tag{33}$$

In an axial symmetric case, such as Fig.14 (b), $\mathrm{Tr}(\hat{\sigma})$ is $(\sigma_{\parallel} + 2\sigma_{\perp})$, and the span becomes $(\sigma_{\parallel} - \sigma_{\perp})$. Then the shielding constant is:

$$\sigma_{zz} = \frac{1}{3}\mathrm{Tr}(\hat{\sigma}) + \frac{1}{3}(3\cos^2\theta_{\parallel} - 1)(\sigma_{\parallel} - \sigma_{\perp}) \tag{34}$$

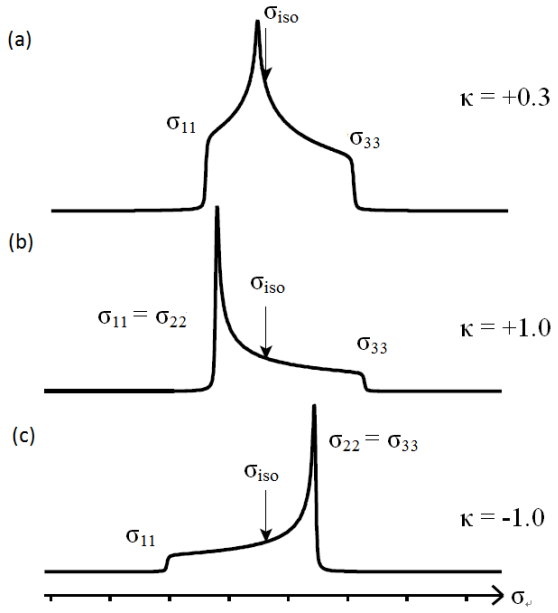

Figure 14. Powder spectra with different CSA tensors (a) low symmetric case (b) axial symmetric case with $\kappa = 1$ (c) axial symmetric case with $\kappa = -1$.

2.1.3.4 The Quadrupolar Interaction

Quadrupolar interactions occur for nuclei with $I > 1/2$. Such spins have non spherical positive charge distribution, as illustrated in Fig.15, and so they possess the quadrupole moments

Q. The quadrupole moment would interact with the electric field gradient (EFG) of the nuclear site, which is caused by asymmetric electron density around the nucleus. The magnitude of EFG depends on the symmetry of the molecule and chemical bonding, and EFG tensors are always traceless. Therefore in solution, the quadrupolar interactions are averaged to zero.

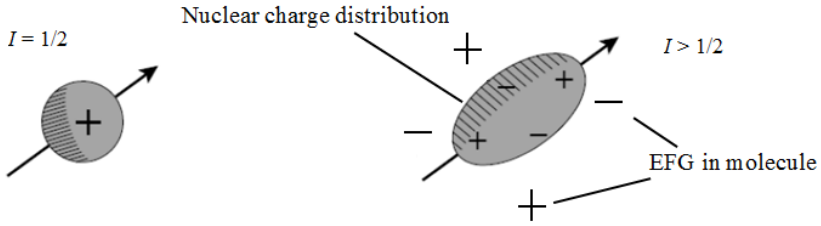

Figure 15. Origin of quadrupole moments and EFG.

In solid-state NMR, the quadrupole moments (eQ) interact with the electric field gradient at the nuclear site to broaden the spectra significantly. Similar to the shielding tensor, EFG tensor in PAS is:

$$\widehat{V}^{PAS} = \begin{pmatrix} V_{XX} & 0 & 0 \\ 0 & V_{YY} & 0 \\ 0 & 0 & V_{ZZ} \end{pmatrix} \tag{35}$$

where $|V_{ZZ}| > |V_{YY}| > |V_{XX}|$. The nuclear quadrupole coupling constant is defined as:[54]

$$C_Q = \frac{eQV_{ZZ}}{h} \tag{36}$$

Also there is the asymmetry parameter:

$$\eta_Q = \frac{V_{XX} - V_{YY}}{V_{ZZ}} \tag{37}$$

where $0 \leq \eta_Q \leq 1$. If $\eta_Q = 0$, the EFG tensor is said to be axially symmetric. The Hamiltonian is written as the sum of first and second order perturbation to the Zeeman interaction: [55,56]

$$\mathcal{H}_Q = \mathcal{H}_Q^{(1)} + \mathcal{H}_Q^{(2)} \tag{38}$$

The first order perturbation is proportional to C_Q, of which the Hamiltonian is:

$$\mathcal{H}_Q^{(1)} = \frac{1}{2}\frac{\omega_Q}{2}\left[3\cos^2\theta - 1 - \eta_Q \sin^2\theta \cos 2\varphi\right]\left[\hat{I}_Z - \hat{\boldsymbol{I}}(\hat{\boldsymbol{I}}+1)/3\right] \tag{39}$$

θ and φ are the polar coordinates of the applied magnetic field in the PAS of the EFG, and,

$$\omega_Q = \frac{3eV_{ZZ}Q}{2I(2I-1)\hbar} \tag{40}$$

is called the quadrupole frequency. It is the shift that the quadrupolar interaction made to the energy levels as shown in Fig.16(a). The first order perturbation is proportional to C_Q while the second order perturbation is proportional to ${C_Q}^2/\nu_o$. If the EFG increases so that the quadrupolar interaction becomes strong enough, then the second order term could not be ignored. Perturbation theory can be used to calculate the second order energy shifts:[56]

$$\omega_Q^{(2)} = -\frac{\omega_Q^2}{16\omega_0}\left(I(I+1) - \frac{3}{4}\right)(1-\cos^2\theta)(9\cos^2\theta - 1) \tag{41}$$

when $\eta = 0$. The orientation of EFG tensor also matters.

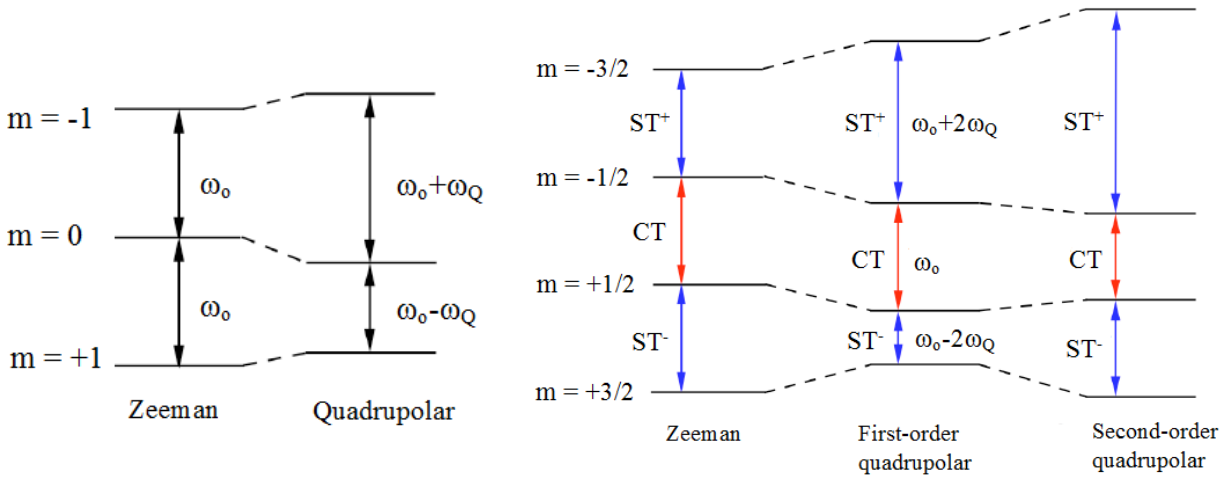

Figure 16. Frequency shifts from the quadrupolar interaction for spin-1 nuclei (left) and first and second order perturbations on the energy levels of spin-3/2 nuclei (right).

In Fig.16, CT means the central transition and ST is the satellite transition. Notice that first order perturbation does not affect the central transition. With large C_Q's, the satellite transitions are broadened and are not observable on the spectra. The peaks of central transitions also have irregular shapes due to the anisotropy, as seen in Fig.17.

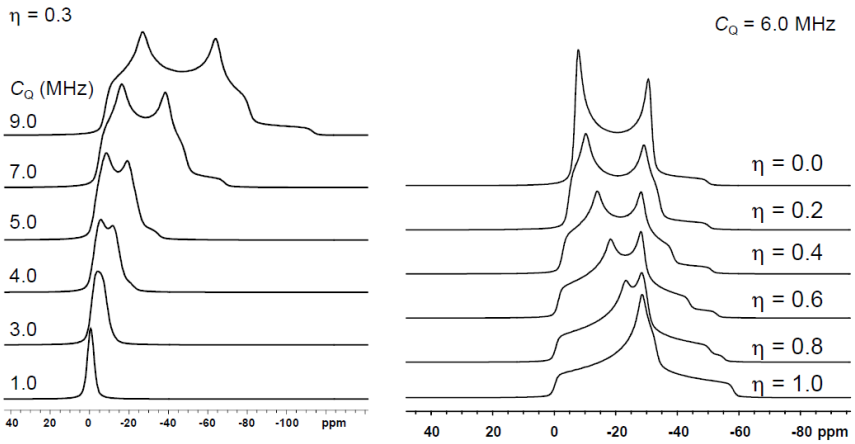

Figure 17. Simulated solid-state ^{27}Al (I = 5/2) NMR spectra with various η and C_Q values. (Figures are reproduced from http://mutuslab.cs.uwindsor.ca/schurko/ssnmr/ssnmr_schurko.pdf.)

2.1.3.5 The Hyperfine Interaction

For molecules with unpaired electrons, there exists the hyperfine interaction. It describes the dipolar interaction between the unpaired electron(s) and the nuclei. The hyperfine interaction is usually much stronger than other nuclear spin interactions discussed in the previous sections, and it contributes significantly to both solution and solid-state NMR spectra. This interaction will be discussed in detail in a later section (§2.3).

2.2 Basic NMR Spectroscopy

2.2.1 Rotating Frame and FID

In NMR spectroscopy, the rotating frame is always used instead of the lab frame in order to simplify the motions of magnetization vectors. In the rotating frame, the x and y axes are rotating constantly in the x-y plane at the Larmor frequency. As a consequence, the precessing magnetization vectors could be seen as stationary in the rotating frame as in Fig.18.

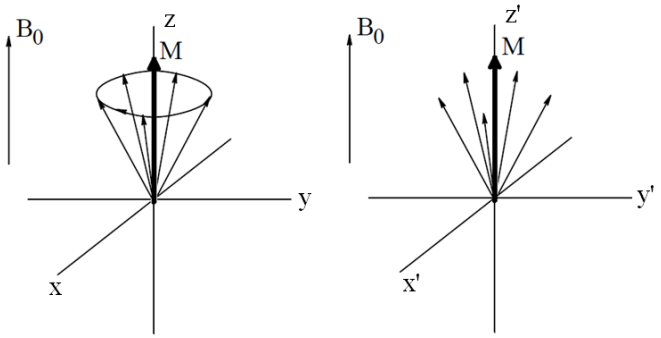

Figure 18. Magnetization vectors in lab frame (left) and in rotating frame (right).

The most common way to generate NMR signals is to apply an RF pulse. In the rotating frame, a perturbing magnetic field B_1 that is oscillating at the Larmor frequency is applied along the x axis. Consequently, spins would precess around B_1, and the net magnetization is tipped toward the y axis in the y-z plane as shown in Fig.19. As mentioned in §2.1.2, the component in the x-y plane would undergo fast dephasing. Therefore a signal would be produced in the receiving coil along the y axis. This signal, as illustrated in Fig.20, is called the free induction decay (FID). It describes the decaying of magnetization along the y axis (M_y)

since it has the tendency to go back to the equilibrium position.

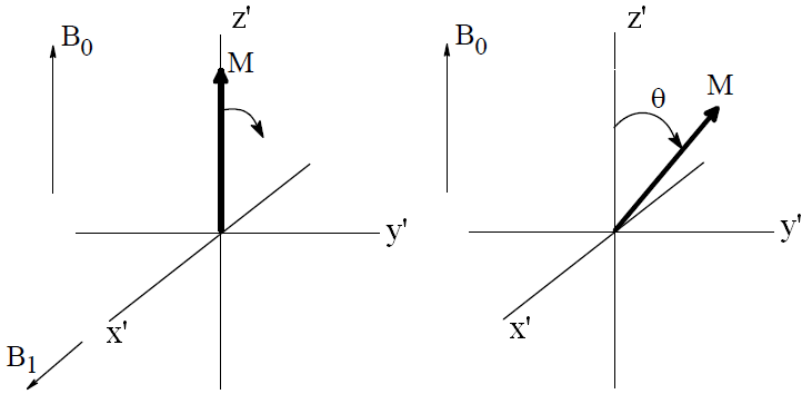

Figure 19. The effect of an RF pulse.

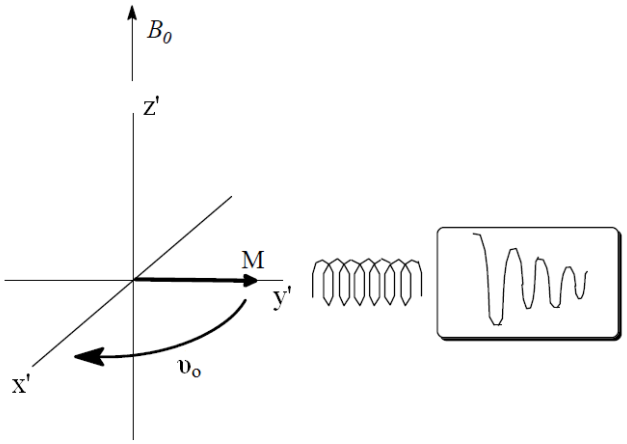

Figure 20. Receiving coil and free induction decay.

Usually the RF pulse covers a range of frequencies that will perturb all nuclei of the same type in the molecule. The flip angle θ is how much the magnetization is tipped during the pulse duration (t_p). They are related by the following equation:

$$\theta = \gamma B_1 t_p \tag{42}$$

where θ is in rad, and γ is in rad•$s^{-1}G^{-1}$. As shown in Fig.21, M_y is the greatest after a 90° pulse, and is zero with a 180° (π) pulse.

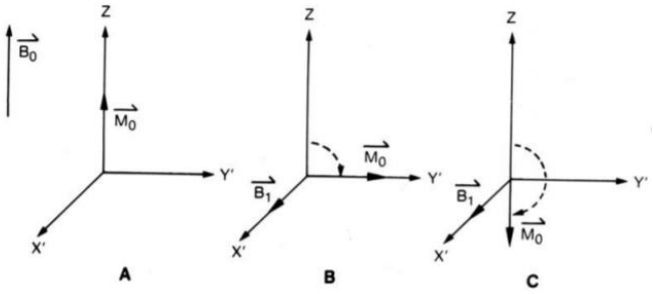

Figure 21. Rotation of magnetization in the y-z plane. (A) At equilibrium; (B) After a 90° pulse; (C) After a 180° pulse.

In NMR experiments, Eq.42 indicates that the FID signal is time dependent. Applying Fourier transform would change the signal from time domain to frequency domain according to:

$$f(\nu) = \int_{-\infty}^{\infty} F(t) \exp(-i2\pi\nu t)\, dt \tag{43}$$

as illustrated in Fig.22.

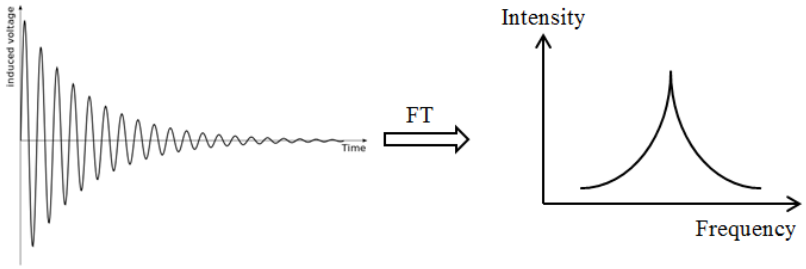

Figure 22. FID (left) and Fourier transformed spectrum (right).

2.2.2 Basic NMR parameters

When performing FT-NMR experiments, there are some common parameters that will affect the strength and quality of signals. As mentioned in the previous section, the duration of the applied RF pulse affects the strength of signal. This is referred as the pulse width (PW). After

the RF pulse, an acquisition time (AQ) is allowed for the coil to acquire the signal. Appropriate AQ needs to be set for the experiments. If the acquisition time is too long, unnecessary noise would be included in the spectrum. If it is too short, wiggles will appear on the bottom of the peaks.

In NMR experiments, the signal to noise ratio (S/N) matters a lot. A high S/N would give a better spectrum. The simplest way to increase S/N is to apply repeated pulses. Before each pulse, there is a recycle delay time (D1). The length of D1 depends on the spin-lattice relaxation time (T_1). Then there comes the pulse width and acquisition time as shown in Fig.23. The number of times that this cycle repeated is called the number of scans (Ns). The signal to noise ratio is proportional to the square root of number of scans ($\sqrt{Ns}$). Increasing Ns would strengthen the signal significantly and average out the noise.

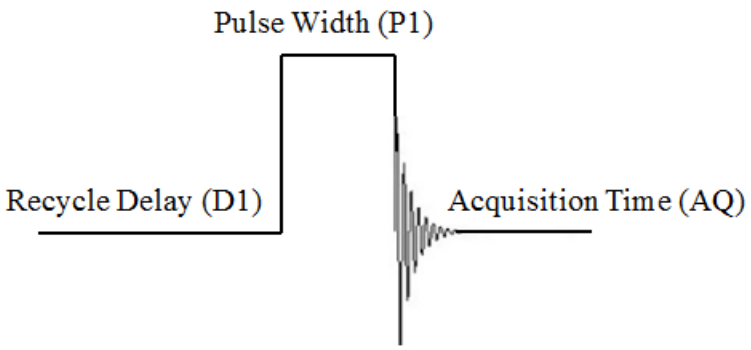

Figure 23. One cycle of the RF pulse sequence.

The series of points used to define the FID signal is described as the number of points (TD). A spectrum would be better defined for a large TD. The sweep width (SW) is the range of frequency (in Hz or ppm) that a spectrum will cover. TD and SW are related to the acquisition

time by:

$$\mathrm{AQ} = \frac{\mathrm{TD}}{2\mathrm{SW}} \tag{44}$$

The digital resolution (DR) of the spectrum is the inverse of acquisition time:

$$\mathrm{DR} = \frac{1}{\mathrm{AQ}} = \frac{2\mathrm{SW}}{\mathrm{TD}} \tag{45}$$

DR is in units of Hz/point. In general, the digital resolution should be less than one half of the width at the half-height of a peak. This requires that the acquisition time should not be so short. Also the power level of the RF pulse is defined as PL in dB. PL1 means the power level for channel 1. Correspondingly P1 is the width of the RF pulse in this channel.

2.2.3 Solution-state NMR

Molecules undergo fast tumbling in isotropic solutions. Most of the anisotropic NMR interactions are averaged out due to these motions, such as nuclear dipolar couplings and quadrupolar interactions mentioned before. Therefore NMR peaks from solution-state samples, especially for spin –1/2 nuclei such as ^{1}H and ^{13}C, are relatively sharp and well resolved in general. For chemical analysis, chemical shifts and J-couplings provide crucial structural information.

Each chemical functional group has an empirical range of CS. Fig.24 shows some general ranges of ^{1}H and ^{13}C chemical shifts of common functional groups in organic molecules. Electronegative groups such as –F will reduce the electron density around neighbouring nuclei causing deshielding. Hydrogen bondings (usually –OH or –NH) will also greatly deshield the nuclei and could be observed over a large range of CS.

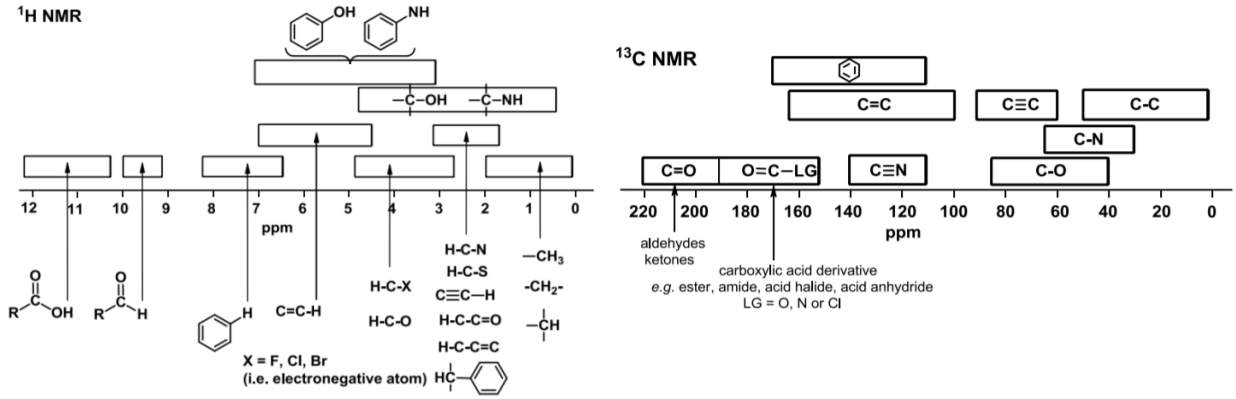

Figure 24. General ^{1}H and ^{13}C chemical shift ranges for various chemical functional groups. (Figure was reproduced from https://elearning03.ul.pt/mod/resource/view.php?id=34021.)

In high resolution solution-state ^{1}H NMR, peaks split due to J-couplings. N equivalent ^{1}H nuclei on the neighbouring carbon atom would cause a signal to split into a multiplet containing N+1 peaks. Since J-coupling is a bond-mediated interaction, it would become weaker as the number of connecting bonds increases. Fig.25 shows a simple case with 1,1-dichloroethane. The doublet around 2 ppm is from the protons on the methyl group, while the quartet around 6 ppm is from $–CHCl_2$.

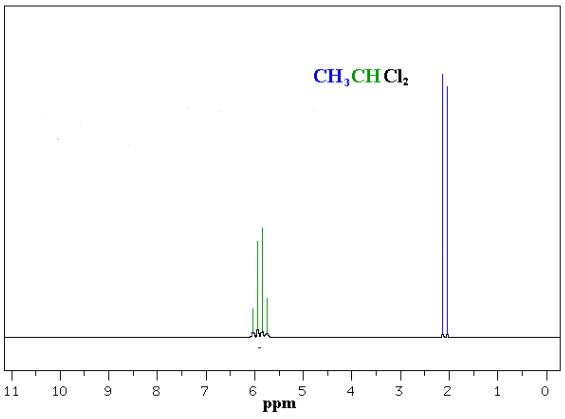

Figure 25. Simulated ^{1}H spectrum of 1,1-dichloroethane. (Figure was reproduced from http://www.chem.ucalgary.ca/courses/350/Carey5th/Ch13/ch13-nmr-5.html.)

Protons are also coupled to ^{13}C. To avoid messy readings, ^{13}C NMR spectra are always decoupled from protons. The principle behind decoupling is that irradiation of the RF field at the specific frequency for protons is kept on when acquiring ^{13}C FIDs. In this case the protons will keep flipping between the two energy states (m = 1/2 and m = -1/2) very rapidly, so that other nuclei only "see" an average state of them. Therefore ^{13}C signals would not split due to the neighbouring protons as seen in the ^{13}C spectrum of methyl methacrylate shown in Fig.26.

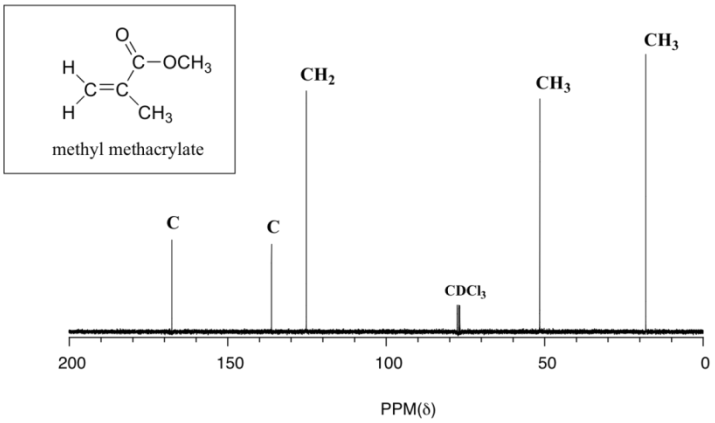

Figure 26. Simulated ^{1}H decoupled ^{13}C spectrum of methyl methacrylate in deuterated chloroform. (Figure was reproduced from https://chem.libretexts.org/Textbook_Maps/Organic_Chemistry_Textbook_Maps.)

2.2.4 Solid-state NMR

Unlike in solution NMR where anisotropic interactions are averaged to zero due to molecular tumbling, solid-state NMR provides an opportunity to measure their anisotropic spin interactions. However, the consequence is that solid-state NMR spectra usually contain very broad and irregularly shaped signals. Such spectra are sometimes difficult to analyze. Several solid-state NMR techniques can be applied to simplify the spectra.

Solid-state NMR is powerful tool in chemical and biological studies. As we discussed in the previous section, large molecules such as proteins have very short T_2 relaxation times in solution, which broaden their NMR peaks. Practically it is difficult to do solution-state NMR studies for molecules over 100 kDa. In solids, molecules are almost static so NMR studies are no longer limited by the molecular tumbling correlation time. In principle, there is no molecular weight limit for solid-state NMR studies. Also, there are chemicals and materials that are insoluble in common solvents so that solution-state NMR is not appropriate. In this case solid-state NMR would be a better choice. With improving techniques, solid-state NMR has become widely applied in increasing number of areas.

2.2.4.1 Magic Angle Spinning

As we saw in previous discussions, many nuclear interactions contain a geometric factor in the form of $(3\cos^2\theta - 1)$. In fact, in isotropic solutions, the dynamic molecular tumbling averages this factor to zero. This is the reason why solution-state NMR spectra often contain narrow lines. If there is a design in solid-state NMR experiments that manually eliminate this factor, it would greatly reduce the line broadening due to anisotropic dipolar shielding and interactions. The trick is called magic angle spinning (MAS).[41]

To understand how MAS works, some math work was done to find the average of the geometric factor. In Fig.27, **r** is the internuclear vector, β is the angle between the sample rotation axis and the applied field, and χ is the angle between **r** and the rotation axis. It is proved that:[57]

$$\langle 3\cos^2\theta - 1\rangle = \frac{1}{2}\langle 3\cos^2\beta - 1\rangle\langle 3\cos^2\chi - 1\rangle \quad (46)$$

Since spins are randomly orientated in a powder sample, θ could have any possible value between 0 and 180º. Notice that if the sample tube is fixed at an angle of β = 54.7º, then $\cos\beta = \frac{1}{\sqrt{3}}$ and so $3\cos^2\beta - 1 = 0$. As a result, $\langle 3\cos^2\theta - 1\rangle = 0$ regardless of the spin orientations in the powder sample. Therefore in principle the effect of the dipolar interaction and shielding anisotropy are eliminated by this technique. The angle of 54.7º is called the magic angle.

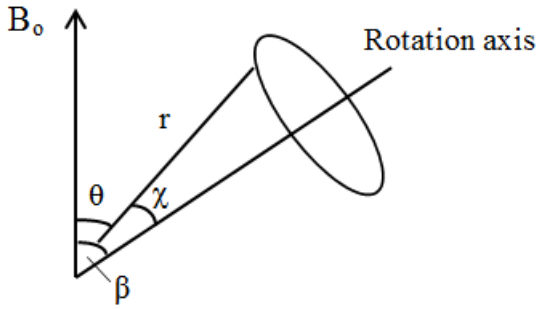

Figure 27. Geometric map of a spinning sample tube.

2.2.4.2 Cross Polarization

For spins with low natural abundance, such as ^{13}C (1.109%) and ^{17}O (0.037%), they are recognized as dilute spins in NMR. Solid-state NMR experiments of dilute spins are usually more difficult. One thing is that they couple with abundant spins to broaden the spectra. This problem could be overcome by decoupling as mentioned. The other thing is that dilute spins, ^{13}C for example, usually have long spin-lattice relaxation times. It takes a long time to acquire the spectra if the usual multipulse sequence is used. The solution to this problem is called cross

polarization (CP).[42]

The first step of CP is to apply a 90° pulse to ^{1}H, and then spin-lock the magnetizaiton on the y-axis in the rotating frame. Simply put, spin-locking is to maintain the coherent magnetization by switching B_1 to the y-axis. In this situation the magnetization will not undergo transverse relaxation, but instead it will stay along the y-axis and decay much slower as shown in Fig.28.

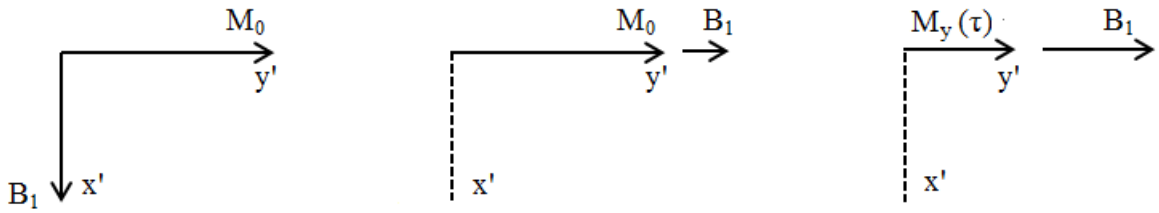

Figure 28. Magnetization and pulse in spin-locking process.

Right after the 90° pulse is applied in the proton channel, another RF pulse in the ^{13}C channel is turned on as seen in Fig.29. The strength of the RF field on ^{13}C is adjusted so that:

$$\gamma_H B_{1H} = \gamma_C B_{1C} \tag{47}$$

This is named as the Hartmann-Hahn matching condition.[58] The condition indicates that ^{1}H and ^{13}C are precessing at the same rate in the rotating frame, and hence their energies are matched. This allows a transfer of the magnetization from ^{1}H to ^{13}C. In the normal situation, the magnetization of ^{13}C produced is given by the Curie Law:

$$M_0(C) = \frac{C_c B_0}{T_L} \tag{48}$$

where $C_c = \frac{1}{4}\gamma_H^2 \hbar^2 \frac{N_H}{k}$ and T_L is the lattice temperature. After the CP it is enhanced such that:

$$M_0(C) = \frac{C_c B_0}{T_L}\left(\frac{\gamma_H}{\gamma_C}\right) \tag{49}$$

The magnetization gains a factor of $\frac{\gamma_H}{\gamma_C}$, which is around 4.

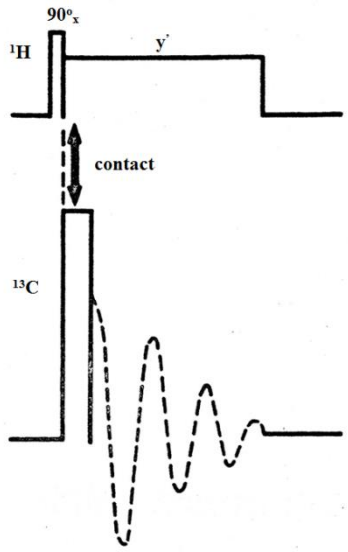

Figure 29. The pulse sequence for the CP experiment.[53]

The benefit that CP brings to dilute spin experiments is not only the signal enhancement, but also shortening of the recycle delay between scans. This is because the recycle time in the CP experiment is determined by the T_1 of protons, which often are much shorter than that for dilute spins.

2.3 Basic Concepts of Paramagnetic NMR Spectroscopy

2.3.1 Hyperfine Shifts

The total chemical shifts of nuclei in paramagnetic compounds are composed of two parts. The first part is the diamagnetic shift, also known as the orbital shift arising from all paired electrons within the molecule of interest. The second part is called the hyperfine shift that is due

to the interactions with the unpaired electrons. So the observed shift is:

$$\delta^{obs} = \delta^{orb} + \delta^{hf} \tag{50}$$

where δ^{orb} is the orbital shift, and δ^{hf} is the hyperfine shift. For δ^{hf}, two contributions are considered in our study, the Fermi contact shift (δ^{con}) and the electron-nuclear dipolar coupling shift (δ^{dip}):

$$\delta_{ii}^{hf} = \delta^{con} + \delta_{ii}^{dip} \tag{51}$$

δ_{ii} means the *i*th tensor component of the in the PAS.

The Hamiltonian of the hyperfine interaction can be written as:[44]

$$\widehat{\mathcal{H}}_{hypefine} = \hat{I} \cdot \widehat{A} \cdot \hat{S} \tag{52}$$

where $\hat{I}$ and $\hat{S}$ are the nuclear and electron spin angular momentum vectors, respectively. $\widehat{A}$ consists of an isotropic part and an anisotropic part:

$$\widehat{A} = A_{iso} \cdot \hat{1} + \widehat{T} \tag{53}$$

A_{iso} is called the isotropic hyperfine coupling constant, and $\widehat{T}$ is the anisotropic dipolar tensor, which can be further expressed as:[44]

$$A_{iso} = \frac{4\pi}{3S} \hbar \gamma g \mu_B \rho_{\alpha\beta} \tag{54}$$

$$T_{ij} = -\frac{1}{2S} \hbar \gamma g \mu_B \langle \frac{r^2 \delta_{ij} - 3 r_i r_j}{r^5} \rangle \tag{55}$$

where γ is the nuclear gyromagnetic ratio, g is the free electron g value, μ_B is the Bohr magneton, r is the distance between the nucleus and the electron, S is the total electron spin quantum number and $\rho_{\alpha\beta}$ is the electron spin density at the nucleus under study.

The Fermi contact coupling arises from the delocalization of the electron spin density. It is a "through bond" effect from the atom containing unpaired electrons, such as metal ions to the

ligand molecular orbitals. It is related to the isotropic hyperfine coupling constant (electron spin density $\rho_{\alpha\beta}$). The Fermi contact coupling is sensitive to even small electron spin density. It is analogous to the J-coupling commonly encountered in NMR for diamagnetic molecules. Without covalent bonding, the Fermi contact shift would not exist. The Fermi contact shift can be expressed as:[44]

$$\delta^{\mathrm{con}} = \mathrm{p}\frac{(\mathrm{S}+1)\rho_{\alpha\beta}}{\mathrm{T}} \tag{56}$$

where $\mathrm{p} = \frac{\mu_o(\mu_B g)^2}{9k} = 2.35 \times 10^7 \mathrm{ppm} \cdot \mathrm{K} \cdot \mathrm{au}^{-1}$, and T is the absolute temperature.

The second contribution to the hyperfine shift is from the dipolar coupling between unpaired electron spin and nuclear spin. It is analogous to the nuclear dipolar couplings, which is a "through space" interaction. This electron-nucleus dipole coupling can be expressed as an anisotropic tensor $\rho_{\alpha\beta}^{\mathrm{ii}}$ in the atomic units. The dipolar shift is then written as:

$$\delta_{\mathrm{ii}}^{\mathrm{dip}} = \mathrm{p}(\frac{8\pi}{3})\frac{(\mathrm{S}+1)\rho_{\alpha\beta}^{\mathrm{ii}}}{\mathrm{T}} \tag{57}$$

The total hyperfine shift would be the sum of Eqs.56 and 57, and is related to the hyperfine coupling tensor A_{ii} in the following way:

$$\delta_{\mathrm{ii}}^{\mathrm{hf}} = \left(\frac{\mathrm{A_{ii}}}{\hbar}\right)\frac{g\mu_B S(S+1)}{3\gamma_N kT} = \mathrm{p}\frac{(S+1)}{T}(\rho_{\alpha\beta} + \frac{8\pi}{3}\rho_{\alpha\beta}^{\mathrm{ii}}) \tag{58}$$

This total hyperfine shift is also known as the paramagnetic shift or Knight shift. Note that the effect from the g tensor anisotropy is ignored in our study.

In solution-state NMR studies, isotropic hyperfine shifts can be very large, placing the NMR signals for paramagnetic compound significantly outside the normal chemical shit range for diamagnetic compounds. In solid-state NMR, the anisotropic hyperfine tensor needs to be considered. It contributes to the line shape like a CSA powder pattern. For spin - 1/2 nuclei, the

anisotropic hyperfine tensor can be readily analyzed from the line shape. For nuclei with $I > 1/2$, the line shapes are more complicated because of the presence of the quadrupolar interactions.

2.3.2 Relaxation Effects

Besides the large hyperfine shifts, unpaired electrons in paramagnetic compounds also significantly affect the nuclear relaxation times. Typically NMR signals exhibit a Lorentzian line shape. The full width at the half maximum (FWHM) of the peak is related to the transverse relaxation time, T_2,

$$\mathrm{FWHM} = \frac{1}{\pi T_2} \tag{59}$$

In paramagnetic compounds, the existence of unpaired electrons will greatly shorten both T_1 and T_2. As a result, NMR signals from paramagnetic molecules usually experience severe line broadenings. There are three contributions to the short relaxation time: electron-nuclear dipolar effect, contact coupling effect, and Curie spin effect. The first two effects were first proposed by Solomon[18] and Bloembergen.[17] The combined equations for both effects are shown below as Eqs.60 and 61. Here, assuming that electron is a point dipole for the dipolar effect, r is the distance between electron and nucleus. The equations for the relaxation times are:[59]

$$T_1^{-1} = \frac{2}{15}\left[\frac{S(S+1)\gamma^2 g^2 \mu_B^2}{r^6}\right]\left[\frac{\tau_c}{1+(\nu_I-\nu_S)^2\tau_c^2} + \frac{3\tau_c}{1+\nu_I^2\tau_c^2} + \frac{6\tau_c}{1+(\nu_I+\nu_S)^2\tau_c^2}\right] + \frac{2}{3}\left[\frac{S(S+1)A_{con}^2}{\hbar^2}\right]\left[\frac{\tau_S}{1+(\nu_I-\nu_S)^2\tau_S^2}\right] \tag{60}$$

$$T_2^{-1} = \frac{1}{15}\left[\frac{S(S+1)\gamma^2 g^2 \mu_B^2}{r^6}\right]\left[4\tau_c + \frac{\tau_c}{1+(\nu_I-\nu_S)^2\tau_c^2} + \frac{3\tau_c}{1+\nu_I^2\tau_c^2} + \frac{6\tau_c}{1+\nu_S^2\tau_c^2} + \frac{6\tau_c}{1+(\nu_I+\nu_S)^2\tau_c^2}\right] + \left[\frac{S(S+1)A_{con}^2}{3\hbar^2}\right]\left[\tau_S + \frac{\tau_S}{1+(\nu_I-\nu_S)^2\tau_S^2}\right] \quad (61)$$

where ν_I and ν_S are the resonance frequencies for nuclei and electrons, τ_c and τ_S are the correlation times for dipolar effect and contact effect respectively. Here τ_c and τ_S are dependent on the electron relaxation times, T_{1e} and T_{2e}, as well as rotational correlation time and chemical exchange rate. Under some extreme cases one can show that:[59]

$$FWHM = \pi^{-1}(K_1 + K_2)T_{1e} \quad (62)$$

where K_1 and K_2 are collected constants for dipolar and contact effect terms. Although generally this approach is not reliable, it is straightforward that nuclear relaxation times depend on both T_{1e} and T_{2e} because they both contribute to the correlation time. To obtain narrow NMR peaks, short electron relaxation times are preferred. Practically the averaged life time of electron spin τ_e is used to describe the electron relaxation time, which is generally equivalent to T_{1e}. According to Abragam,[60] the following constraint is required to observe NMR signals:

$$2\pi A_{iso}\tau_e \ll 1 \quad (63)$$

This requires short electron relaxation times and relatively small A_{iso}. For molecules with long τ_e, the signals are usually very broad that only atoms with very small hyperfine coupling constants can be observed in NMR spectra. Table 3 gives a list of τ_e values for some common paramagnetic systems. Complexes with short τ_e, such as V^{3+}, Mn^{3+} and Fe^{3+} compounds usually produce narrow NMR signals, and those with relatively long τ_e like Cu^{2+} and VO^{2+} will give

broad peaks.

For a concentrated sample of a paramagnetic compound in solution, the applied magnetic field could cause the polarization of the large quantity of electron spins, generating a net magnetization noted as $\langle S_z \rangle$. This is named the Curie spin effect. The most important thing could be its effect on T_2 which is:[61, 62]

$$T_2^{-1} = \left[\frac{\gamma_I^2 g^2 \mu^2 \mu_0^2}{80\pi^2}\right] \langle S_z \rangle^2 \left[4\tau_r + \frac{3\tau_r}{1+\nu_I^2 \tau_r^2}\right] \quad (64)$$

Here τ_r is the rotational correlation time of the nuclear spin, and μ is the magnetic moment of the molecule. This relation indicates that Curie spin effect could dominate T_2 under high field for complexes with high-spin metal centers. For large molecules such as proteins, the rotational correlation time is long which also contributes to the T_2 relaxation rate. Therefore under such conditions, line broadenings due to the Curie spin effect could be very significant.

Table 3. Typical τ_e values for common paramagnetic systems.[63]

Paramagnetic System	S	τ_e(s)
Organic radicals	1/2	10^{-6}-10^{-8}
VO^{2+} (d^1)	1/2	10^{-8}
V^{3+} (d^2)	1	10^{-11}
Cu^{2+} (d^9)	1/2	10^{-9}
Cr^{3+} (d^3)	3/2	5×10^{-9}-5×10^{-10}
Cr^{2+} (d^4)	2	10^{-11}-10^{-12}
Mn^{3+} (d^4)	2	10^{-10}-10^{-11}
Mn^{2+} (d^5)	5/2	10^{-8}
Fe^{3+} (d^5, high spin)	5/2	10^{-9}-10^{-11}
Fe^{3+} (d^5, low spin)	1/2	10^{-11}-10^{-13}
Fe^{2+} (d^6, high spin)	2	10^{-12}-10^{-13}

2.4 Computational Details

It is often desirable that quantum chemical calculations are performed before NMR experiments. Since NMR signals from paramagnetic compounds have a large range of chemical shifts, the computational results can aid the search for NMR signals. One of the objectives of this thesis is to establish the reliability of quantum chemical computations.

2.4.1 Fundamental Paramagnetic NMR Parameters

As explained in the previous section, the main difficulties in detecting NMR signals for paramagnetic compounds are their large hyperfine shifts and severe line broadenings. Both factors are related to the hyperfine tensor. Most quantum chemical calculation packages allow evaluation of A-tensors.

As mentioned before, there is also a diamagnetic contribution called the orbital shift. This σ_{orb} part can be calculated by the GIAO magnetic shielding option that is again available in software products such as G09 and ADF. The computed shielding value can be converted to the chemical shift using the following equation:

$$\delta_{\mathrm{orb}} = \sigma_{\mathrm{ref}} - \sigma_{\mathrm{orb}} \tag{65}$$

where σ_{ref} is the absolute shielding constant for a reference molecule. Table 4 shows the σ_{ref} values for nuclei studied in this thesis.

Table 4. Absolute shielding constants used in this thesis.

Nucleus	*I*	σ_{ref} (ppm)	References
^{1}H	1/2	32.87	64,65
^{13}C	1/2	186.37	66
^{15}N	1/2	-135.8	67
^{17}O	5/2	287.50	68

In solution-state NMR spectra, hyperfine shifts dominate the signal positions. Using A_{iso} from the calculation and the expression in Eq.58, the hyperfine shift can be calculated. Note that in Eq.58, A_{iso} is in unit of Joule, but A_{iso} from calculation outputs is usually in MHz. To obtain the hyperfine shift in ppm, the following expression can be used:

$$\delta_{hf} = (2\pi 10^{6} A_{iso}) \frac{g\mu_B S(S+1)}{3\gamma kT \cdot 10^{-6}} \tag{66}$$

where A_{iso} is in MHz, and other constants are in the SI units. The total chemical shift is then calculated by adding the orbital and paramagnetic parts:

$$\delta = \delta_{hf} + \delta_{orb} \tag{67}$$

In this way, the calculated chemical shift can be directly compared with experimental results. For the anisotropic tensor $\hat{T}$, it is arranged in the way as the CSA tensor, $T_{11} < T_{22} < T_{33}$. While T_{ii} does not contribute to the isotropic hyperfine shift, the difference between T_{33} and T_{11} is responsible for line broadening. According to Eq.66, if the chemical shift of a signal is monitored at different temperatures, a plotting of δ vs. 1/T would yield the value of A_{iso}. In this way, hyperfine coupling constants could be determined from variable temperature experiments. This

strong temperature dependence is also a useful method to inspect whether a NMR signal is from a paramagnetic compound or not. If one studies paramagnetic compounds in the solid state, $\hat{\mathbf{T}}$ tensor will influence the line shape together with other nuclear spin interactions such as chemical shift, quadrupolar interaction, etc.

2.4.2 Quantum Chemical Calculation Software Products

All quantum chemical calculations reported in this thesis were performed using Gaussian 09[69] and ADF 2016.[70-72] The licensed software products are provided by the Center for Advanced Computing (Queen's University, Kingston, Ontario, Canada). Calculation jobs are directly submitted to the Frontenac cluster. General procedures of calculations are described below. For solution-state NMR studies, the molecular structures of the interested compounds were obtained from crystal structures found in the literatures. After finalizing the molecular structure, a geometry optimization was carried out. The optimized molecular structure was then used for quantitative calculations. Since results for atoms on equivalent positions may differ slightly from each other, an averaging from all equivalent atoms was performed. It is important to note that, our calculations are performed for molecules in the gas phase. However, because hyperfine shifts are usually very large, any solvent effect would be negligible.

For solid-state NMR, the calculations were performed using BAND,[73-77] which is included in ADF2016. BAND is specially designed for handling calculations for periodic systems. For a compound of interested, a crystal information file (CIF) was often found from the Crystallography Open Database (COD). The CIF file can be opened with Gaussview5/ADFGUI

to obtain the Cartesian coordinates. Optimization was then performed using BAND, and the optimized coordinates were then used for A-tensor calculations.

2.4.2.1 Basis Sets

For every calculation, one has to specify a basis set for each type of atom. In quantum chemical calculations, basis sets are used to fit the molecular orbitals (MOs). Practically, basis sets consist of functions of atomic orbitals (AOs). A linear combination of AOs is usually used to describe MOs.

There are two commonly used types of basic functions. One is the Slater-type orbital (STO) and the other one is the Gaussian-type orbital (GTO). A STO is defined as:

$$\phi_{abc}^{STO}(x,y,z) = Nx^a y^b z^c e^{-\zeta r} \tag{68}$$

In Eq.68, N is normalization constant. Constants a, b and c represents the angular momentum:

$$L = a+b+c \tag{69}$$

ζ defines the width of the orbital. This type of function is more accurate, but is harder to do integrals. A GTO is defined as:

$$\phi_{abc}^{GTO}(x,y,z) = Nx^a y^b z^c e^{-\zeta r^2} \tag{70}$$

Definitions of the symbols are the same with Eq.68. To solve the accuracy problem, a STO function is usually expressed as a linear combination of GTO's (CGTO's). An example is the default basis set in the Gaussian software, STO-3G.[78] The CGTO's are written as:

$$\phi_{abc}^{CGTO}(x,y,z) = N\sum_{i=1}^{n} c_i\, x^a y^b z^c e^{-\zeta_i r^2} \tag{71}$$

The minimal basis set is, clearly, one basis function for each AO in the atom. The double-zeta

basis set means two basis functions for each AO, and triple-zeta and quadruple zeta basis sets are similarly defined. For example, a C atoms need 5 basis functions for a minimal basis set (1s, 2s, $2p_x$, $2p_y$ and $2p_z$), and 10 basis functions for a double-zeta basis set. A split-valence basis set means that one function is used for the core orbitals, and more functions are applied for the valence orbitals.

As is known, pure AO's are "static" models. The actual AO's may shift a little bit under the influence of neighbouring atoms. This is called polarization. A polarized s orbital can mix with p orbitals, and p orbitals can mix with d orbitals, etc. With this effect, polarization functions need to be added to the basis sets. A double-zeta (DZ) basis set with polarization functions are named as double-zeta plus polarization (DZP) basis set. Fig.30 shows two simple examples of basis sets.

```
C   0
S   3  1.00
      71.6168370          0.154328970
      13.0450960          0.535328140
       3.53051220         0.444634540
S   3  1.00
       2.94124940        -0.999672300E-01
       0.683483100        0.399512830
       0.222289900        0.700115470
P   3  1.00
       2.94124940         0.155916270
       0.683483100        0.607683720
       0.222289900        0.391957390
```

```
C   0
S   6  1.00
      4232.61000          0.202900000E-02
       634.882000         0.155350000E-01
       146.097000         0.754110000E-01
       42.4974000         0.257121000
       14.1892000         0.596555000
       1.96660000         0.242517000
S   1  1.00
       5.14770000         1.00000000
S   1  1.00
       0.496200000        1.00000000
S   1  1.00
       0.153300000        1.00000000
P   4  1.00
       18.1557000         0.185340000E-01
       3.98640000         0.115442000
       1.14290000         0.386206000
       0.35940000         0.640089000
P   1  1.00
       0.11460000         1.000000000
D   1  1.00
       0.75000000         1.000000000
```

Figure 30. STO-3G basis set (left) and a DZP basis set (right) for carbon atoms formatted in Gaussian software style. The first column represents ζ, and the second column are c_i's.

When dealing with anions and electronegative atoms, it is sometimes necessary to add diffuse functions. Diffuse functions have small ζ values, see Eqs.68 and 71, which means the electron is far from the nucleus. Selection of basis sets can greatly affect the results of calculations. Particularly in Guassian09, the internally stored basis sets are sometimes not complete enough for the metal atom as the paramagnetic center. However, most of the atoms we worked with have proper basis sets inside the programs. Table 5 is a list of commonly used basis sets in G09 and ADF2016. Tests of the capability of basis sets were also done in our study as described in the next chapter.

Table 5. Frequently used internal basis sets in Gaussian09 and ADF2016.

Basis set	Software	Description	Application
6-31G[79-88]	Gaussian09	Double-zeta with CGTO made of 6 GTO for core orbitals and one CGTO of 3 GTO, one GTO for valence orbitals	H-Kr
6-311G[89-97]	Gaussian09	Split-valence triple-zeta basis adding one GTO to	H-Kr
EPR-II[98,99]	Gaussian09	Double zeta basis set with a single set of polarization functions and an enhanced s part optimized for EPR calculations	H, B-F
DZ	ADF2016	Double-zeta basis set without polarization functions	All
TZP	ADF2016	Triple-zeta with polarization added from H to Ar	All
TZ2P	ADF2016	Triple-zeta with two polarization functions	H-Kr
QZ4P	ADF2016	Quadruple-zeta with four polarization functions optimized relativstically	All
jcpl	ADF2016	Double-zeta basis set designed for ESR calculations	Selected elements

Note: In Gaussian, polarization is requested using * or (p) after basis set, and diffusion is added by + or (d). For example, 6-31G(d) is 6-31G with added d polarization functions on non-hydrogen atoms; 6-311++G is 6-311G with added diffusion functions for hydrogen and non-hydrogen atoms.

2.4.2.2 Density Functional Theory

In our study, the underlying theory of all calculations is the Kohn-Sham approach to the Density Functional Theory (DFT).[100, 101] So far in chemistry, DFT provides the most successful approach to calculations of molecular properties. DFT predicts the ground state properties of a system based on the electron density. Its ultimate goal is to find the best approach to the unknown exchange-correlation energy in order to minimize the energy of the system. This is the reason why it is also named as exchange-correlation (XC) functional.

For a chemical system, the ground state energy can be written as:[100]

$$E_O = \min_{\rho \to N}(F[\rho] + \int \rho(\vec{r}) V_{NE} d\vec{r}) \quad (72)$$

where ρ stands for the electron density, V_{NE} is the potential energy of nuclear-electron (NE) interaction. $F[\rho]$ is the universal functional that contains the kinetic energy, the classical Coulomb interaction and the non-classical energy part, which is:

$$F[\rho] = T[\rho] + J[\rho] + E_{ncl}[\rho] \quad (73)$$

The Coulomb interaction part $J[\rho]$ is known. Kohn and Sham proposed that the kinetic energy can be computed using the assumptions of Hartree-Fock approximation,[102, 103] from which the contribution due to the kinetic energy is:

$$T_S = -\frac{1}{2}\sum_i^N \langle \psi_i | \nabla^2 | \psi_i \rangle \quad (74)$$

where ψ_i's are the orbitals of a non-interacting system. With this approach, $F[\rho]$ is re-written as:

$$F[\rho] = T_S[\rho] + J[\rho] + E_{XC}[\rho] \quad (75)$$

E_{XC} is the exchange-correlation energy as mentioned. It contains everything that is unknown. DFT gives the approximation of E_{XC}, which are the well-known Kohn-Sham equations.[101] The

form of the ground-state orbital wave function was proposed to minimize the full energy for the system.

$$V_S(\vec{r}_1) = \int \frac{\rho(\vec{r}_2)}{r_{12}} d\vec{r}_2 + V_{XC}(\vec{r}_1) - \sum_A^M \frac{Z_A}{r_{1A}} \tag{76}$$

$$\left(-\frac{1}{2}\nabla^2 + V_S(\vec{r}_1)\right)\psi_i = \epsilon_i \psi_i \tag{77}$$

Based on the Kohn-Sham equations, there are two most common approximations of XC functional. The first one is called local density approximation (LDA). This approximation is based on the assumption of uniform electron gas in the system. In this case, E_{XC} can be written as:

$$E_{XC}^{LDA}[\rho] = \int \rho(\vec{r}) \epsilon_{XC}\big(\rho(\vec{r})\big) d\vec{r} \tag{78}$$

ϵ_{XC} is the exchange-correlation energy per particle for uniform electron gas with density ρ. ϵ_{XC} is further separated into two parts, the exchange part and the correlation part:

$$\epsilon_{XC}\big(\rho(\vec{r})\big) = \epsilon_X\big(\rho(\vec{r})\big) + \epsilon_C\big(\rho(\vec{r})\big) \tag{79}$$

The expression for the exchange part for the energy of an electron was derived by Bloch and Dirac:[104,105]

$$\epsilon_X = -\frac{3}{4}\left(\frac{3\rho(\vec{r})}{\pi}\right)^{1/3} \tag{80}$$

There is no exact expression for ϵ_C. The approximation was proposed by Ceperly-Alder.[106]

LDA has moderate accuracy. Its assumption with homogeneous electron gas is clearly not sufficient. To improve this, the generalized gradient approximation (GGA)[107-109] was proposed. The approximation of E_{XC} is based on the charge density as well as its gradient. The gradient part could explain the inhomogeneity of the electron gas.

$$E_{XC}^{GGA}[\rho] = \int f(\rho, \nabla\rho) d\vec{r} \tag{81}$$

GGA provides a more accuracy approach to most of the systems. It is further improved by Becke,[110] who introduced the hybrid functional:

$$E_{XC}^{hyb} = \alpha E_X^{KS} + (1-\alpha) E_{XC}^{GGA} \quad (82)$$

where E_X^{KS} is the exchange energy calculated from the Kohn-Sham equations, and α is fitting parameter. The improved accuracy of GGA and hybrid functional is important to quantum chemical studies, especially for small chemical systems.

B3LYP of hybrid functional[111] was used throughout all our calculations for isolated molecules in both Gaussian09 and ADF2016. For solid-state NMR studies, since BAND does not allow the use of a hybrid functional, GGA BP86 by Becke[110] and Perdew[112] was used in our calculations.

2.4.2.3 Algorithms of Hyperfine A-tensor Calculation for Periodic Systems

In ADF2016, the hyperfine A-tensors[113] and magnetic NMR shielding[114-119] are calculated using the DFT method including relativistic correction of zeroth order regular approximation (ZORA)[120] with all electron basis sets. According to the previous research and our results, the calculation outputs have high consistency with the experimental data. The fact shows the matureness of the underlying algorithms. BAND calculations are for periodic systems of solids. Interestingly, no literature was found to report A-tensor calculations using BAND. Our objective in this thesis was to test the accuracy of the BAND calculation on A-tensors. While ADF can handle both diamagnetic and paramagnetic NMR shielding calculations,[121-123] magnetic shielding for the paramagnetic system cannot be computed in BAND.

The DFT based method for the calculation of hyperfine A-tensor was developed by Kadantsev and Ziegler.[124] The method also includes the relativistic ZORA effect without the frozen core approximation. The hyperfine Hamiltonian is written as usual:

$$\hat{\mathcal{H}}_{\mathrm{hf}} = \sum_{\mathrm{N}} \hat{I}_{\mathrm{N}} \cdot \hat{\mathrm{A}}_{\mathrm{N}} \cdot \hat{\mathrm{S}} \tag{83}$$

where $\hat{\mathrm{S}}$ is the total electron spin operator, and $\hat{I}_{\mathrm{N}}$ is the nuclear spin operator of atom N. For the ZORA effect, the kinetic energy $-1/2\hat{\mathrm{p}}^2$ operator is modified as:

$$\hat{\mathrm{T}}^{\mathrm{ZORA}} = \hat{\boldsymbol{\sigma}} \cdot \hat{\mathrm{p}} \frac{\mathrm{K}}{2} \hat{\boldsymbol{\sigma}} \cdot \hat{\mathrm{p}} \tag{84}$$

where $\hat{\mathrm{p}}$ is the momentum operator which is:

$$\hat{\mathrm{p}} = -\mathrm{i}\nabla \tag{85}$$

$\hat{\boldsymbol{\sigma}}$ is the vector of Pauli matrices:

$$\hat{\boldsymbol{\sigma}} = (\hat{\sigma}_{\mathrm{x}}, \hat{\sigma}_{\mathrm{y}}, \hat{\sigma}_{\mathrm{z}}) \tag{86}$$

and K has the expression of:

$$\mathrm{K} = \frac{1}{1 - \mathrm{V_S}(\vec{\mathrm{r}})/2\mathrm{c}^2} \tag{87}$$

where $\mathrm{V_S}(\vec{\mathrm{r}})$ is the KS potential (Eq.76), and c is the speed of light. For Pauli matrices, it was proved that:

$$(\hat{\boldsymbol{\sigma}} \cdot \vec{\mathrm{a}})(\hat{\boldsymbol{\sigma}} \cdot \vec{\mathrm{b}}) = \vec{\mathrm{a}} \cdot \vec{\mathrm{b}} + \mathrm{i}\hat{\boldsymbol{\sigma}} \cdot (\vec{\mathrm{a}} \times \vec{\mathrm{b}}) \tag{88}$$

Apply this to Eq.84, the kinetic energy without the applied magnetic field can be expressed as:

$$\hat{\mathrm{T}}_{\mathrm{SR}}^{\mathrm{ZORA}} + \hat{\mathrm{T}}_{\mathrm{SO}}^{\mathrm{ZORA}} = \hat{\mathrm{p}} \frac{\mathrm{K}}{2} \hat{\mathrm{p}} + \frac{1}{2} \hat{\boldsymbol{\sigma}} \times (\nabla \mathrm{K} \times \hat{\mathrm{p}}) \tag{89}$$

The first term in Eq.89 is the scalar relativistic term, and the second term is called spin-orbit term. After the external magnetic field is applied, the momentum operator should be modified as:

$$\hat{\mathrm{P}} = \hat{\mathrm{p}} + \frac{\hat{\mathrm{A}}}{\mathrm{c}} \tag{90}$$

where $\vec{\mathrm{A}}$ is the vector potential:

$$\vec{\mathrm{B}} = \nabla \times \vec{\mathrm{A}} \tag{91}$$

Therefore, Eq.89 becomes:

$$\hat{\mathrm{T}}^{\mathrm{ZORA}} = \hat{\mathrm{P}}\frac{\mathrm{K}}{2}\hat{\mathrm{P}} + \frac{\mathrm{i}}{2}\hat{\boldsymbol{\sigma}} \cdot \left\{\left(\hat{\mathrm{p}} + \frac{\hat{\mathrm{A}}}{\mathrm{c}}\right)\mathrm{K} \times \left(\hat{\mathrm{p}} + \frac{\hat{\mathrm{A}}}{\mathrm{c}}\right)\right\} \tag{92}$$

With some linear algebra involved, the kinetic energy finally is:

$$\hat{\mathrm{T}}^{\mathrm{ZORA}} = \hat{\mathrm{p}}\frac{\mathrm{K}}{2}\hat{\mathrm{p}} + \frac{1}{2}\hat{\boldsymbol{\sigma}} \cdot (\nabla \mathrm{K} \times \hat{\mathrm{p}}) + \frac{\mathrm{K}}{2\mathrm{c}}\vec{\mathrm{A}}\hat{\mathrm{p}} + \hat{\mathrm{p}}\vec{\mathrm{A}}\frac{\mathrm{K}}{2\mathrm{c}} + \frac{\mathrm{K}}{2\mathrm{c}^2}\vec{\mathrm{A}}^2 + \frac{\mathrm{K}}{2\mathrm{c}}\hat{\boldsymbol{\sigma}} \cdot \vec{\mathrm{B}}_0 + \frac{1}{2\mathrm{c}}\hat{\boldsymbol{\sigma}} \cdot \left(\nabla \mathrm{K} \times \vec{\mathrm{A}}\right) \tag{93}$$

Relatively, the first two terms are the scalar relativistic and spin-orbit terms. The third and the fourth terms are ignored in the following algorithm. The rest of the terms are recognized as microscopic hyperfine Hamiltonian:

$$\hat{\mathcal{H}}_{\mathrm{mic}}^{\mathrm{hf}} = \frac{\mathrm{g_e}}{2}\frac{1}{2\mathrm{c}}\left\{\mathrm{K}\hat{\boldsymbol{\sigma}} \cdot \vec{\mathrm{B}}_0 + \hat{\boldsymbol{\sigma}} \cdot \left(\nabla \mathrm{K} \times \vec{\mathrm{A}}\right)\right\} \tag{94}$$

Then it is further expressed as:

$$\hat{\mathcal{H}}_{\mathrm{mic}}^{\mathrm{hf}} = \sum_C \frac{\mathrm{g_e g_C}}{8\mathrm{M}c^2}\hat{\boldsymbol{\sigma}}\left\{-\hat{I}_{\mathrm{C}}(\nabla \cdot \mathrm{K}\nabla(\frac{1}{\Delta \mathrm{r_C}}) + \left(\hat{\mathrm{I}}_{\mathrm{C}} \cdot \nabla\right)\mathrm{K}\nabla\left(\frac{1}{\Delta \mathrm{r_C}}\right)\right\} \tag{95}$$

where $\Delta\vec{\mathrm{r}}_{\mathrm{C}} = \vec{\mathrm{r}} - \vec{\mathrm{R}}_{\mathrm{C}}$ and $\Delta \mathrm{r}_{\mathrm{C}}$ is the distance from nucleus C. The nuclear magnetic moment for C is:

$$\mu_{\mathrm{C}} = \frac{\mathrm{g_C}}{2\mathrm{M_C}}\hat{I}_{\mathrm{C}} \tag{96}$$

$\mathrm{g_C}$ is the nuclear g value and $\mathrm{M_C}$ is the nuclear mass. The corresponding vector potential is:

$$\vec{\mathrm{A}} = \mu_{\mathrm{C}} \times \frac{\Delta\vec{r}_C}{\Delta r_C^3} = -\mu_{\mathrm{C}} \times \nabla(\frac{1}{\Delta r_C}) \tag{97}$$

Therefore the magnetic field at nucleus C is:

$$\vec{B} = \nabla \times \vec{A} = -\nabla \times \left[\mu_C \times \nabla(\frac{1}{\Delta r_C})\right] \tag{98}$$

By using Eqs.97 and 98, the tensor components can be derived. The procedure is described in detail by Lenthe:[120]

$$(A_C)_{kl} = \frac{g_e g_C}{4Mc^2} \int m(\vec{r}) \left\{ \delta_{kl} \nabla \cdot \left(K \frac{\Delta \vec{r}_C}{\Delta r_C^3} \right) - \nabla_k \left(K \frac{(\Delta \vec{r}_C)_l}{\Delta r_C^3} \right) \right\} d\vec{r}$$

$$= \frac{g_e g_C}{4Mc^2} \int \frac{K}{\Delta r_C^3} ((\Delta \vec{r}_C)_l \nabla_k m(\vec{r}) - \delta_{kl} \Delta \vec{r}_C \cdot \nabla m(\vec{r})) d\vec{r} \tag{99}$$

where $m(\vec{r}) = \rho_\alpha(\vec{r}) - \rho_\beta(\vec{r})$ is the spin density difference between two electron spin states. In the case that $K \to 1$, the nonrelativistic components are obtained:

$$(A_C)_{kl} = \frac{g_e g_C}{4Mc^2} \int m(\vec{r}) \left\{ \frac{3}{8\pi} \delta(\Delta \vec{r}_C) \delta_{kl} + 3 \frac{(\Delta \vec{r}_C)_k (\Delta \vec{r}_C)_l}{\Delta r_C^5} - \frac{\delta_{kl}}{\Delta r_C^3} \right\} d\vec{r} \tag{100}$$

Eqs.99 and 100 are two different approaches to calculate A-tensor components. In the user's guide of BAND, Eq.99 is described as the "from gradient" method, while Eq.100 is named as the "from density". For the gradient method, the isotropic hyperfine coupling constant is an integral term. For the density method, it is

$$(A_C)_{iso} = \frac{2\pi g_e g_C}{3Mc^2} \{\rho_\alpha(\vec{R}_C) - \rho_\beta(\vec{R}_C)\} \tag{101}$$

Since the isotropic term calculated using Eq.100 is an integral through a smoother function, in principle, A_{iso} determined from the gradient method should be more accurate than from the density approach. They are described as a "nonlocal fashion" for gradient and "local fashion" for density in the user's guide of BAND. The tests of these two methods will be reported in Chapter 4.

2.4.2.4 Features in BAND for A-tensor Calculations

In the BAND input files, the keyword of introducing A-tensor calculation is:

ATENSOR

END

The default method is the gradient approach. To calculate A-tensors using the density approach, one should include in the keyword the following lines:

DEBUG ATENSOR

ATENSOR

END

This option is not listed in the user's guide for BAND. By adding the DEBUG ATENSOR line, the program will calculate the A-tensor using both approaches. Results from the two methods also have different formats in the output files. For the gradient method, A_{iso} values are reported in MHz under every single atom's report. An example is shown in Fig.31. Tensor components A_{ii} are from the full A-tensor ($A_{iso} + T_{ii}$). For the density approach, the isotropic values are reported in the atomic units (a.u.) in a list separated from the reports for single atoms, as seen in Fig.32. To obtain A_{iso}'s in MHz, the A_{iso}'s reported in the list should be multiplied by a conversion factor, and then divided by 2*I*. The values of the conversion factors can be found in reports for individual atoms as indicated in Fig.32. Traceless tensor components T_{ii}'s are reported as a_{ii} in MHz for each single atom.

```
real nuclear spin is                    1.50000000
the nuclear spin 1/2 is assumed, scale if different from real
a.u. to MHz conversion factor is    424.72347279
ATENSOR before diagonalization (a.u):
   -0.7559    0.4508    1.0421
    0.4508   -2.1781   -1.3504
    1.0421   -1.3504   -2.8084
Principles values
(a.u.):           -0.7559        -2.1781        -2.8084
Principles values
(MHz):          -321.0326      -925.0906     -1192.7846
1/3 Tr(A):                        -812.9693 MHz


------------------------------------------------
 isotope             =  63Cu
 nuclear spin I      =  1.5
 magnetic moment mu  =  2.2232900
         g_n = mu/I  =  1.4821933
 quadrupole moment Q = -0.22000 e 10-24 cm2
------------------------------------------------

Atom #      3 Atomic number    29
Coordinates 1st set:           -0.1505   -0.1614   -0.1403
Coordinates 2nd set:           -0.1505   -0.1614   -0.1403

==== calculated tensor (a.u.) Cu
           X             Y             Z
    X   -0.548666E-08  0.327254E-08  0.756444E-08
    Y    0.327254E-08 -0.158104E-07 -0.980232E-08
    Z    0.756444E-08 -0.980232E-08 -0.203855E-07

===== principal axes A-tensor Cu
          11            22            33
    X    0.303164      0.309595      0.901245
    Y   -0.569660      0.817042     -0.089045
    Z   -0.763923     -0.486408      0.424062
principal values calculated tensor Cu (not multiplied by g_n/S)
        -0.306971E-07 -0.873480E-08 -0.225071E-08  a.u.
principal values 63Cu  A-tensor (includes factor g_n/S)
         a11           a22           a33
        -0.598738E+03 -0.170370E+03 -0.438996E+02  MHz <-- Aii's
        -0.199718E+03 -0.568293E+02 -0.146433E+02  10-4 cm-1
Isotropic value  63Cu  A-tensor:      -271.002     MHz <-- Aiso
```

Figure 31. An example of the BAND A-tensor calculation output from the gradient approach.

(a)

```
ATOM#       1 r =                0.00000 Aiso =       1.89917
ATOM#       2 r =                0.00000 Aiso =       1.90384
ATOM#       3 r =                0.00000 Aiso =       1.90015
ATOM#       4 r =                0.00000 Aiso =       1.90384
ATOM#       5 r =                0.00000 Aiso =       0.38325
ATOM#       6 r =                0.00000 Aiso =       0.38325
ATOM#       7 r =                0.00000 Aiso =       0.38303
ATOM#       8 r =                0.00000 Aiso =       0.38301
ATOM#       9 r =                0.00000 Aiso =       0.38322
ATOM#      10 r =                0.00000 Aiso =       0.38321
```

(b)

```
 real nuclear spin is                    1.50000000 <-- I
 the nuclear spin 1/2 is assumed, scale if different from real
 a.u. to MHz conversion factor is    424.72347279
 ATENSOR before diagonalization (a.u):
     0.5173    0.7234    0.4776
     0.7234   -0.2618   -1.1900
     0.4776   -1.1900   -0.2555
 Principles values (a.u.):
0.5173        -0.2618        -0.2555
 Principles values (MHz):
219.6906      -111.1812      -108.5094
 1/3 Tr(A):                            0.0000 MHz


 ------------------------------------------------
  isotope             =  63Cu
  nuclear spin I      =  1.5
  magnetic moment mu  =  2.2232900
         g_n = mu/I   =  1.4821933
  quadrupole moment Q = -0.22000 e 10-24 cm2
 ------------------------------------------------

 Atom #      1 Atomic number    29
 Coordinates 1st set:           11.2455    8.8753   -0.1403
 Coordinates 2nd set:           11.2455    8.8753   -0.1403

 ==== calculated tensor (a.u.) Cu
            X              Y              Z
     X    0.375466E-08  0.525137E-08  0.346674E-08
     Y    0.525137E-08 -0.190016E-08 -0.863777E-08
     Z    0.346674E-08 -0.863777E-08 -0.185450E-08

 ===== principal axes A-tensor Cu
           11             22             33
     X    0.350079      0.748516      0.563177
     Y   -0.678876     -0.211518      0.703127
     Z   -0.645424      0.628477     -0.434101
 principal values calculated tensor Cu (not multiplied by g_n/S)
        -0.128203E-07  0.518150E-08  0.763882E-08  a.u.
 principal values 63Cu  A-tensor (includes factor g_n/S)
         a11            a22            a33
        -0.250057E+03  0.101064E+03  0.148993E+03  MHz <-- Tii's
        -0.834099E+02  0.337112E+02  0.496987E+02  10-4 cm-1
 Isotropic value  63Cu  A-tensor:      0.331587E-12 MHz
```

Factor to convert A_{iso} from a.u. to MHz

Figure 32. An example of the BAND A-tensor output from the density approach. (a) A_{iso} list in a.u. (b) Output section for the traceless part.

Chapter 3 NMR Studies of Paramagnetic Vanadium Compounds in Solution

3.1 Overview

In this chapter, we focus on NMR studies of paramagnetic compounds containing V(III) and V(IV) ions. The electron configuration of a neutral V atom is $[Ar]3d^34s^2$. V exhibits common oxidation states of +5, +4, +3 and +2 as summarized in Table 6. Most of the results reported in this chapter are from vanadium(III) (d^2, S = 1) compounds. Some data are reported for one vanadium(IV) (d^1, S = 1/2) compound.

Table 6. Descriptions of common oxidation states of V.

Oxidation State	Ion	Colour
+5	VO_3^- or VO_2^+	Yellow
+4	VO^{2+}	Blue
+3	V^{3+}	Green
+2	V^{2+}	Violet

Fig.33 shows the structures of the compounds studied in this chapter. Vanadium(III) acetylacetonate, $V(acac)_3$, is an air sensitive dark brown powder at the room temperature. V^{3+} is the paramagnetic metal center, with 6 oxygen atoms bonded to it forming an octahedral structure. It has good solubility in polar organic solvents, and its solution turned out to be stable. $VCl_3(THF)_3$ and $VCl_3(MeCN)_3$ both have octahedral structures. Their powders and solutions are

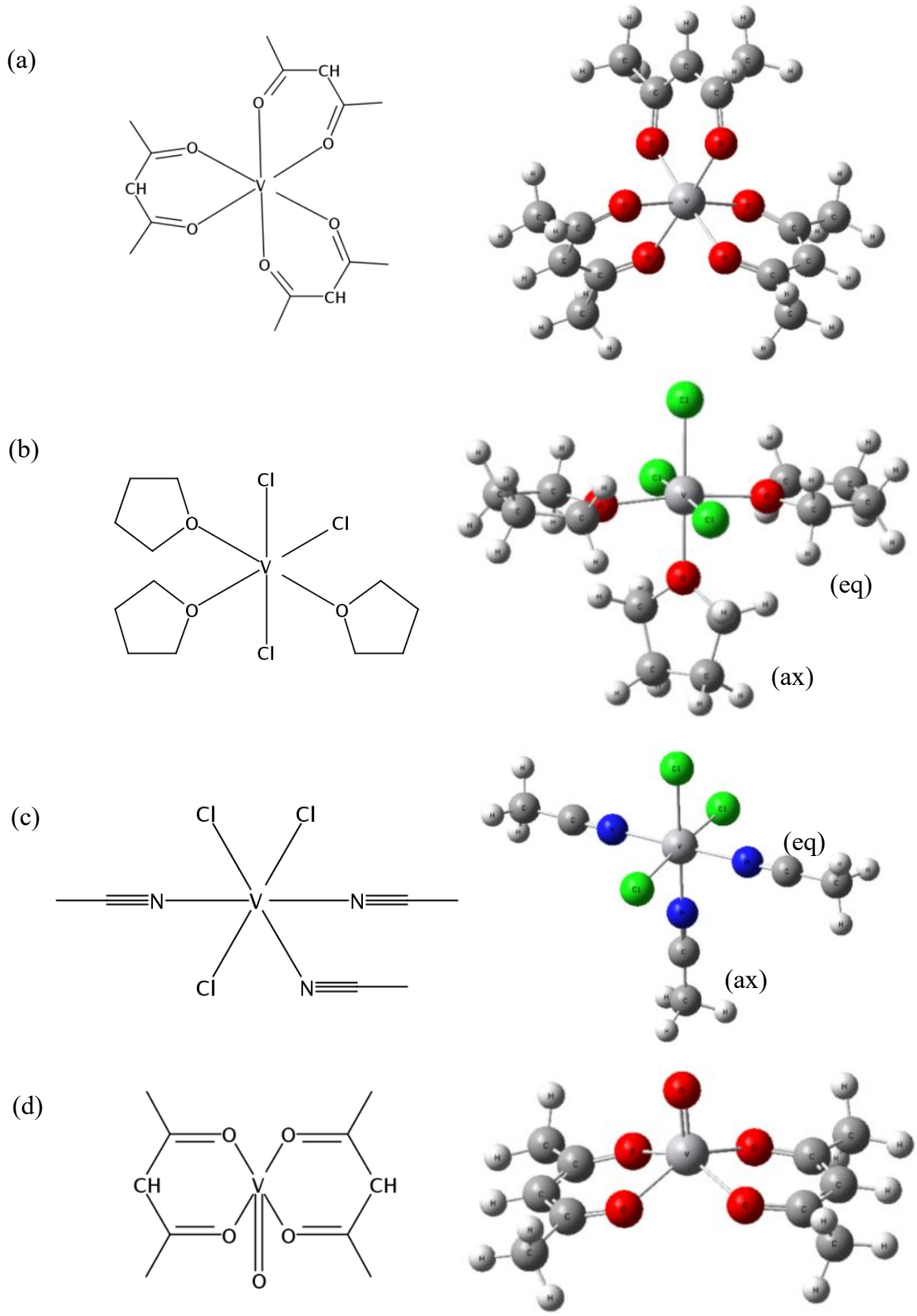

Figure 33. Plane (left) and stereo (right) structure views of (a) V(III)(acac)$_3$ (b) V(III)Cl$_3$(THF)$_3$ (THFs have axial and equatorial types) (c) V(III)Cl$_3$(MeCN)$_3$(MeCNs have axial and equatorial types) (d) V(IV)O(acac)$_2$.

both very unstable, which can be oxidized quickly upon exposure to air. $VO(acac)_2$, vanadyl acetylacetonate, contains a vanadyl ion VO^{2+}(V(IV), d^1). Due to the long electron relaxation time of V^{4+}, it is the only VO^{2+} compound that has been studied. $VO(acac)_2$ is fine blue-green powder. Unlike vanadium(III) compounds, it is very stable in solution and the solid state. The oxygen atoms bonded to the V center form a pyramid structure.

By studying some small V compounds, we intended to establish a correlation between experimental and computed A_{iso} values. The next step is to extend this approach to a large protein system, transferrin. Transferrins are a family of glycoproteins. They are known for their iron-binding properties. In this way they control the level of free iron in the biological fluids.[125] The iron binding ability also provides antimicrobial functions.[126,127] Four types of transferrins have been discovered:[128] 1) serum transferrin in plasma which transfers iron in blood; 2) lactoferrin found in milk; 3) melanotransferrins from melanoma cells, and 4) ovotransferrin discovered from avian egg white. In this study, ovotransferrin was used. Ovotransferrin is also known as conalbumin.[129] It is a single glycopeptide protein with a molecular weight of 77.9 kDa.[130] The N lobe and C lobe both have an iron-binding site. The crystal structure of the binding sites are very similar to those in human serum transferrin. Atoms binding to the iron ion are hexacoordinated. Four of them are from the side chains of amino acids, two tyrosines, one aspartate and one histidine. The rest two are from the correspondence bonded carbonate anion. Structures of the two binding sites, as shown in Fig.34, are very similar. The ovotransferrin, without binding to Fe^{3+} cations, is called apotransferrin. Besides Fe^{3+}, apotransferrin can also bind other metal ions such as Cu^{2+},[131] Ga^{3+},[132] and Cr^{3+}.[133] In our study, we used V^{3+} to replace

Fe^{3+} because a recent study has shown that it is possible to study paramagnetic V(III) coordinate compounds using solid-state NMR.[44]

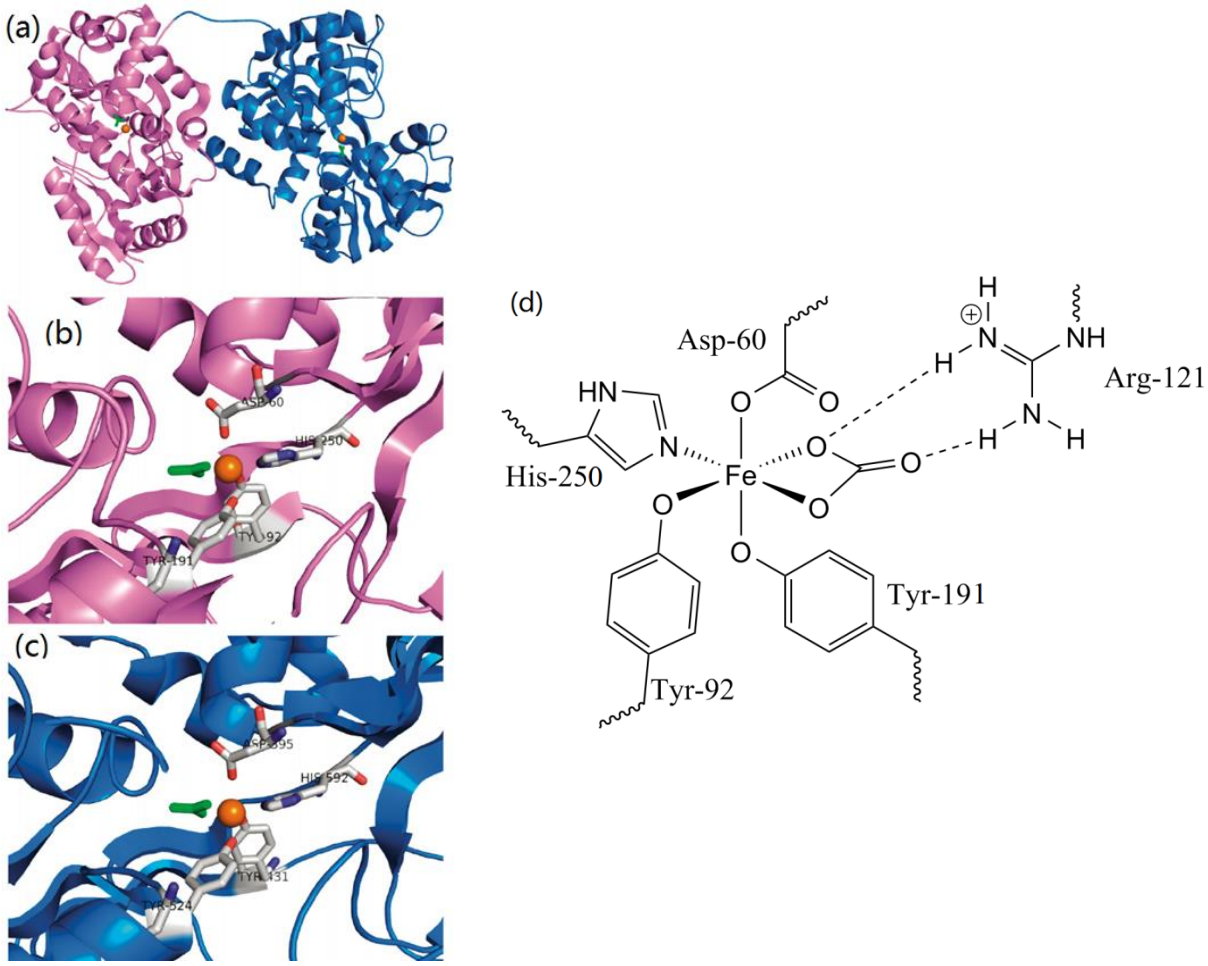

Figure 34. (a) Crystal structure of ovotransferrin. (b) Binding site in the N lobe. (c) Binding site in the C lobe. (d) Structure in detail of the N lobe binding site with Fe^{3+} and CO_3^{2-}.[134]

3.2 Experimental and Computational Details

Unless otherwise indicated, NMR spectra reported and discussed in this thesis were recorded on Bruker 400 and 500 spectrometers. Software products for spectra analysis are Bruker Topspin and MestReNova.[135]

3.2.1 Preparation of Small Vanadium Compounds

$V(acac)_3$ powder was purchased from Sigma-Aldrich. The bottle was stored in a sealed bag filled with nitrogen gas. For ^{1}H and ^{13}C NMR experiments, $V(acac)_3$ (125 mg) was fully dissolved in 0.7 mL DMSO-d_6. For ^{17}O NMR experiments, the sample was prepared by adding $V(acac)_3$ (120 mg) in 0.5 mL $CDCl_3$ to avoid any solvent signal. The solid was not completely dissolved. The saturated solution on the top portion was transferred into a NMR tube.

$VCl_3(THF)_3$ and $VCl_3(MeCN)_3$ samples were both synthesized using VCl_3 (vanadium trichloride), which is a fine black powder purchased from Sigma-Aldrich. $VCl_3(THF)_3$ is a pink crystal synthesized from VCl_3 and tetrahydrofuran (THF) using a procedure modified from the literature.[136] VCl_3 (120 mg) was loaded into a 5 mL pressure tube, and then 2 mL of anhydrous THF was added along with a magnetic stir bar. The pressure tube was sealed and heated in oil bath around 75℃ for about 10 hours. The solution obtained was very concentrated with a brown-red colour. Upon exposure to air, the red colour would disappear giving a brown solution. The further oxidized solution turned green eventually. Similarly, $VCl_3(MeCN)_3$ was synthesized from VCl_3 and acetonitrile. The preparation procedure was also modified from the literature.[137] VCl_3 (200 mg) was transferred into a 5 mL pressure tube, and then 1.5 mL anhydrous acetonitrile was added along with a magnetic stir bar. The mixture was heated in the oil bath at 95℃ for about 10 hours until the solid disappeared and the solution turned into green. The solution was then cooled off quickly in the freezer (−20℃). Small crystals formed on the bottom of the tube were filtered out with a gentle flow of nitrogen gas on the top. For multiple uses, the fresh green crystals were sealed in a vial and then stored in the desiccator. Due to the binding ability of V^{3+},

solvents containing oxygen atoms should be avoided. In order to perform solution-state NMR experiments, some oxygen-free organic solvents were used to test the solubility of $VCl_3(MeCN)_3$. In the end, the crystals were found to dissolve a little bit in methylene chloride (CH_2Cl_2). The low solubility was good enough for ^1H NMR experiments. However, the solution could not stay long enough in the NMR tube to obtain ^{13}C NMR signals. To extend its lifetime, the NMR tube with the dilute solution was heated in the oil bath around 45℃, which boils the CH_2Cl_2. After a few minutes, part of the air in the NMR tube was pressed out, causing a pressure change in the tube leading the solution to stop boiling. The NMR tube was then sealed with Parafilm and cooled to room temperature. Such solutions could remain unchanged for a few hours to allow for the detection of the ^{13}C NMR signals. For variable temperature experiments, only low temperature experiments were performed for $VCl_3(MeCN)_3$ due to the low boiling point of CH_2Cl_2. Moreover, since ^{13}C is dilute spin, it took several hours in order to observe the signals. Under this situation, only three ^{13}C experiments were carried out.

$VO(acac)_2$ (vanadyl acetylacetonate) was purchased from Sigma-Aldrich. It is fine blue-green powder. Unlike vanadium(III) compounds, it is very stable in both solution and solid state. A sample of $VO(acac)_2$ in chloroform was used to observe the ^1H peak from the methyl groups. For other ^1H signals and ^{13}C signals, higher concentrations are needed to observe the broad peaks. Therefore, $VO(acac)_2$ in DMF was used to perform the experiments.

3.2.2 Preparation and Characterization of Transferrin Samples

Ovotransferrin (OTF) extracted from chicken egg white was purchased from Sigma-Aldrich. In a previous work, ^{17}O NMR was performed for OTF-Al^{3+}-$[C_2{}^{17}O_4]^{2-}$.[138] The published work was first reproduced here as a test run. Tris-HCl buffer was adjusted to pH ~ 7.5 and diluted to 0.1 M. About 90 mg OTF was dissolved in 1 mL buffer solution. Aluminum nitrate $[Al(NO_3)_3]$ in stock bottle, which absorbs moisture from air, was dried with nitrogen gas. Dried $Al(NO_3)_3 \bullet xH_2O$ and $K_2[C_2{}^{17}O_4]$ were added to the protein solution to reach a molar ratio slightly over Al^{3+}: $[C_2{}^{17}O_4]^{2-}$: OTF = 2:2:1. Free $[C_2{}^{17}O_4]^{2-}$ ligands were removed by ultrafiltration using a Fisher Scientific accuSpin Micro 17 Microcentrifuge. The protein concentrate was washed with buffer solution for 6 times, at a speed of 13,300 rpm for 30 min to remove all the free ligands. The final concentrate was collected in the NMR tube for solution-state NMR experiments.

The concentration of the apotransferrin solution was determined using UV-vis spectroscopy. The molar absorptivity or molar extinction coefficient ε of OTF at 280 nm is 91200 $M^{-1}cm^{-1}$. Therefore,

$$A_{280}(\mathrm{OTF}) = \varepsilon lc = 92100 \mathrm{M^{-1}cm^{-1}}lc \tag{102}$$

where A_{280} is the absorbance at 280 nm, l is the path length of the light through the sample in cm, and c is the molar concentration of the solution in M. The UV-vis spectra were recorded on a J-815 CD spectrometer in a 1 cm cuvette. A typical UV-Vis spectrum of apotransferrin solution is shown in Fig.35.

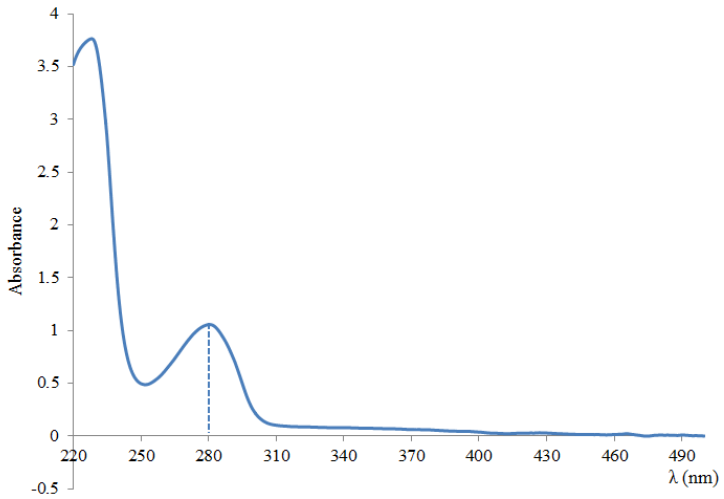

Figure 35. UV-vis spectrum of apotransferrin in Tris-HCl buffer solution (pH~7.5).

To know the concentration of Al^{3+} more accurately, UV difference spectra were obtained in a titration experiment as illustrated in Fig.36. From the apparent slope change in the plot of the absorbance at different molar ratio, the point around Al^{3+}: OTF = 2:1 can be easily determined.

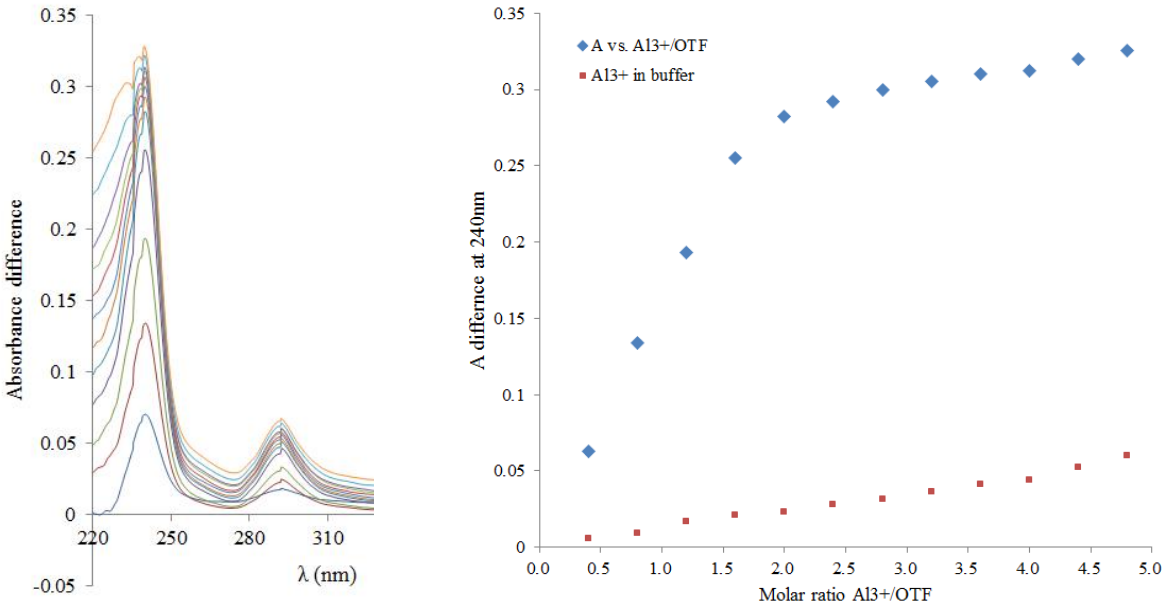

Figure 36. Difference UV spectra upon stepwise addition of Al^{3+} to OTF-HCO_3^- solution (left) and absorbance differences at 240 nm versus molar ratio plot (right). The absorbance of pure Al^{3+} at the same wavelength is also plotted as a slope reference (right). The OTF concentration was around 1μM.

The preparation of OTF-V^{3+}-$[C_2{}^{17}O_4]^{2-}$ was carried out in a similar way. Bertini[139] stated that despite the oxidation reactive properties, V^{3+} can bind to OTF to form a stable product. Based on this finding, efforts were made to study ^{17}O QCT NMR of OTf-V^{3+}-$[C_2{}^{17}O_4]^{2-}$. 120 mg of apotransferrin was weighed in a vial. Tris-HCl buffer was adjusted to pH ~ 8,[139] and then was diluted to 0.1 M. 1 mL of the buffer was added to the vial to dissolve the protein. The UV-vis spectrum was recorded to calculate the OTF concentration. 1.7 mg of $K_2C_2O_4$ (which was enough to saturate the anion binding sites) was added to the apotransferrin solution in the cuvette. VCl_3 aqueous solution was prepared and adjusted to a concentration such that number of moles of VCl_3 in 30 μL of the solution was the same with OTF in the cuvette. The VCl_3 solution was then titrated to the apostransferrin in cuvette. A spectrum was recorded after each 10 μL VCl_3 solution added. The difference spectra were then recorded as shown in Fig.37. Concentrated VCl_3 solution and $K_2C_2[^{17}O_4]$ was then added to the apotransferrin solution in stock to reach the molar ratio a little greater than V^{3+}: $[C_2{}^{17}O_4]^{2-}$: OTF = 2:2:1 to form a light green solution. The free $[C_2{}^{17}O_4]^{2-}$ in OTf-V^{3+}-$[C_2{}^{17}O_4]^{2-}$ solution were removed by ultrafiltration. The final concentrate was obtained and transferred into the NMR tube.

A previous study showed that when the RF field is much smaller than the quadrupolar interaction of the half-integer spin nuclei,[138] one can prove that the effective 90° pulse width for CT is (I + 1/2) times shorter than the normal 90° pulse. Therefore, the pulse length should be shortened to 1/3 for ^{17}O experiments. Before QCT ^{17}O experiments, the 90° pulse was measured using a H_2O sample at a given power level. By determine the time point when the intensity of FID signal became zero, the P1 of 90° pulse can be estimated. For example, in Fig.38 the net

signal intensity is zero at P1 = 58 μs. Therefore the signal with maximum intensity should appear around 29 μs. 29 μs is the 90° pulse width. 1/3 of it should be used when acquiring ^{17}O QCT signals.

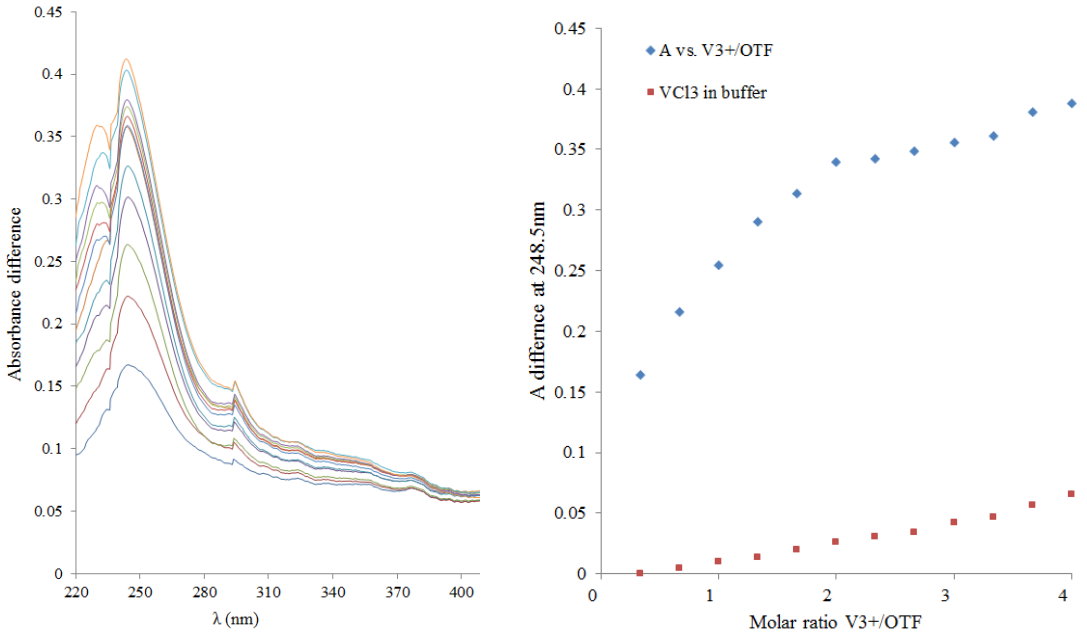

Figure 37. Difference UV spectra upon stepwise addition of V^{3+} to OTF-$C_2O_4^{2-}$ solution (left) and absorbance difference at 248.5 nm versus molar ratio plot (right). The OTF concentration was around 10 μM.

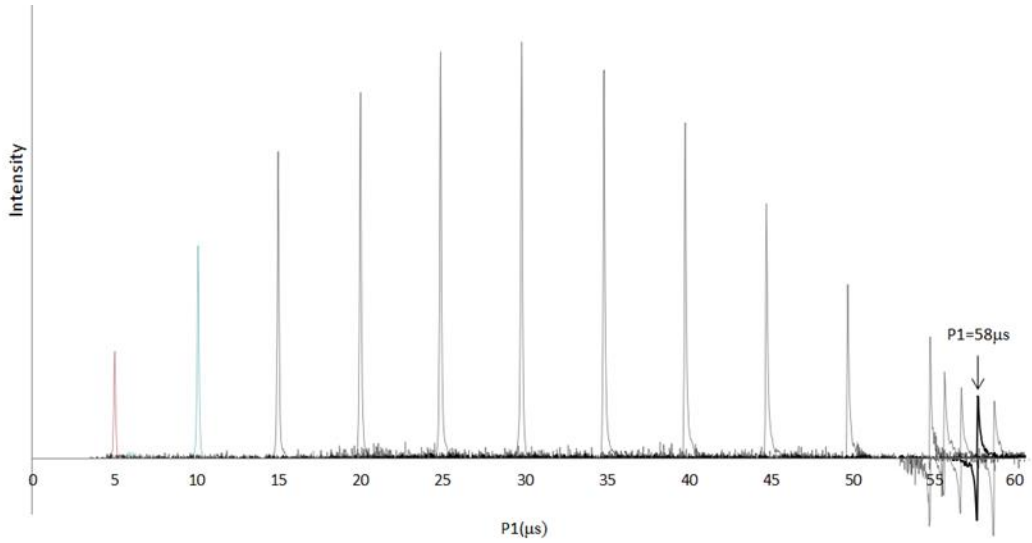

Figure 38. Plot of signal intensities versus different P1 with PL = 2 dB.

Under the QCT signal condition, ^{17}O spectra were recorded on Bruker 600 spectrometer. The spectra were acquired under the conditions of TD = 4096, D1 = 0.005 s, P1 = 5 s and PL1 = 0 dB with a million scans. The signal from free $[C_2{}^{17}O_4]^{2-}$ ligands should appear around 270 ppm.

3.2.3 Computational Details

For small vanadium compounds, the molecular structures were built in Gaussview 5 using crystal structure data reported in the literature.[140,141] The number of unpaired electrons needs to be specified for each system. In Guassian09, the spin multiplicity 2S+1 was needed as an input. In ADF2016, the number of unpaired electrons was described in the input file as number of electron spin-α state exceed spin-β state. For both software products, the B3LYP exchange functional of the DFT method was used. In ADF2016, relativistic ZORA effect was added in all calculations for precision consideration. Moreover, different basis sets were tested for $V(acac)_3$.

3.3 Results and Discussion

3.3.1 Small Vanadium Compounds

In our study, we attempted to record all ^1H, ^{13}C and ^{17}O NMR spectra for each system whenever possible. For each V compounds we studied, all ^1H NMR signals could be assigned, because ^1H's are relatively far from the paramagnetic center, thus with small hyperfine coupling

constants. ^{13}C NMR is more challenging due to its low natural abundance (1%). The ^{13}C NMR experiments can take hundreds of times longer than ^{1}H. For those ^{13}C close to the metal center, the large A_{iso}'s increase the difficulty to observe their NMR signals. For example, in $VO(acac)_2$, we only observed the ^{13}C signal for the methyl groups. ^{17}O has an even lower natural abundance, 0.037%, and the oxygen atom is usually directly attached to the paramagnetic metal center. These make ^{17}O NMR experiments generally most difficult. In our study, we were able to detect only the natural abundance ^{17}O NMR signal from $V(acac)_3$.

Solution-state ^{1}H, ^{13}C and ^{17}O NMR spectra of $V(acac)_3$ are shown in Figs.39-41. In diamagnetic compounds, most ^{1}H signals appear between 0 and 10 ppm, and ^{13}C signals are mostly under 200 ppm. As seen from Fig.39, the effects of unpaired electrons can be quite drastic. The ^{1}H signals from $V(acac)_3$ appear around 40 and 46 ppm, which are impressively greater than signals from diamagnetic compounds. In the ^{13}C spectrum of $V(acac)_3$, the carbonyl carbons experience the strongest hyperfine interaction and thus display the greatest hyperfine shifts, 1090 ppm. The methyl groups acquire negative electron spin density, so their ^{13}C signal has a negative chemical shift around -220 ppm. With the good solubility in chloroform, we were able to observe the ^{17}O signal within 3 hours for $V(acac)_3$. The positions of all signals are consistent with the literature values.[44,142,143]

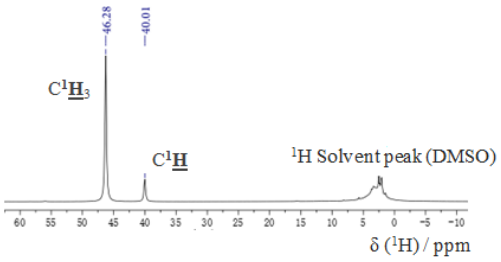

Figure 39. ^{1}H NMR spectra of $V(acac)_3$ in DMSO-d_6.

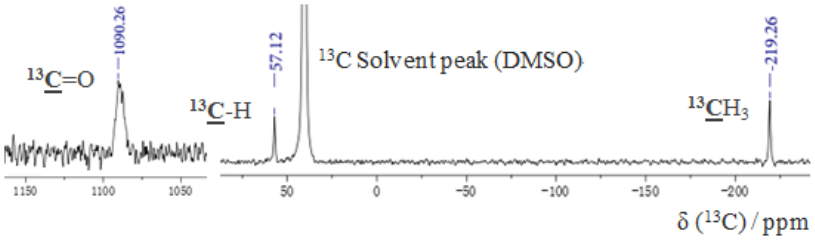

Figure 40. ^{13}C NMR spectra of V(acac)$_3$ in DMSO-d$_6$.

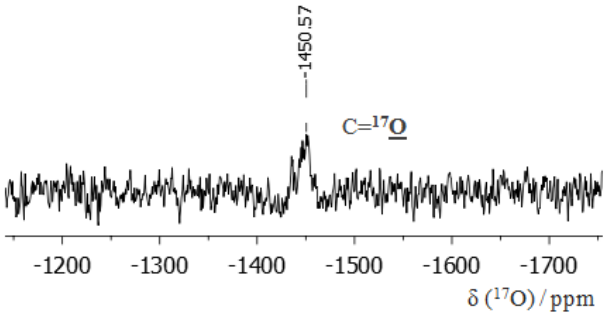

Figure 41. ^{17}O NMR spectrum of V(acac)$_3$ in CDCl$_3$.

Two ^{1}H NMR signals were observed for VCl$_3$(THF)$_3$. As shown in Fig.42, the signal from the ^{1}H that is closer to the metal center has larger chemical shift around 26 ppm. Moreover, it obviously has greater line broadening than the other ^{1}H peak due to the larger anisotropic A-tensor. Similar results were found in the ^{13}C spectrum.

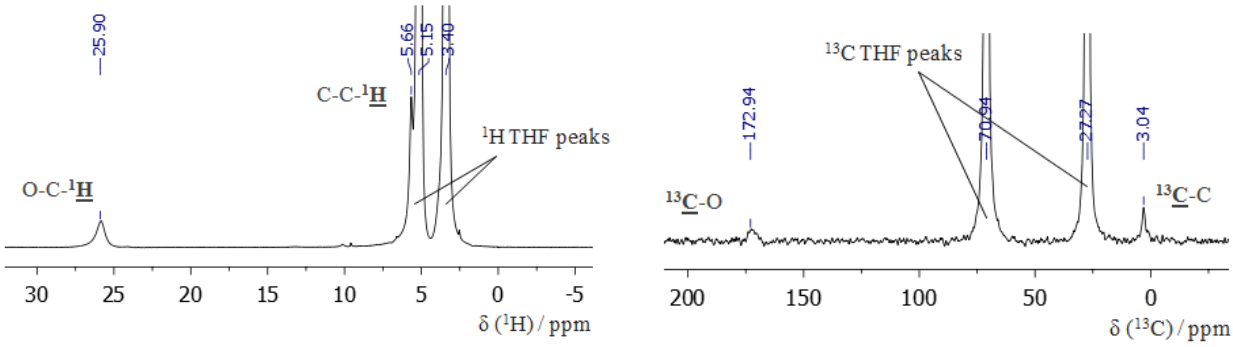

Figure 42. ^{1}H (left) and ^{13}C (right) NMR spectra of VCl$_3$(THF)$_3$ in THF.

Although ^{17}O peak from $V(acac)_3$ was obtained at the natural abundance, the attempt to acquire ^{17}O signal from $VCl_3(THF)_3$ under the same conditions was unsuccessful. It is possible that A_{iso} of the oxygen atoms in $VCl_3(THF)_3$ is greater than that in $V(acac)_3$. Moreover, $VCl_3(THF)_3$ solution is not as stable as $V(acac)_3$. Therefore, with the decreased sensitivity, the lifetime of $VCl_3(THF)_3$ solution may not allow us to observe the ^{17}O signal.

The fact that ^{1}H and ^{13}C NMR signals of $VCl_3(THF)_3$ were observed in THF indicates that ligand exchange must be slow. However, for the analogously synthesized $VCl_3(MeCN)_3$ solution, a very broad ^{1}H peak was observed around the CH_3CN solvent signal position, suggesting that fast ligand exchange occurs. Therefore, we crystalized $VCl_3(MeCN)_3$ and re-dissolved in CH_2Cl_2. In the ^{1}H spectra, an additional peak was observed when the temperature was below -20 ℃. Some early works[144-146] confirmed that there are two structures of $VCl_3(MeCN)_3$, fac and mer as shown in Fig.43. O'Brien[146] reported both of the two structures may exist in the solution at low temperatures. Thus, we assigned the additional peak observed under -20℃ to be from the fac structure as shown in Fig.44. This was further confirmed by our A_{iso} calculation, as will be discussed later. Since $VCl_3(MeCN)_3$ is very unstable in both solid and solution state, the crystals were dissolved in CH_2Cl_2 immediately after filtration. Therefore, in the ^{13}C spectra, some CH_3CN residue signals also appear as seen in Fig.45.

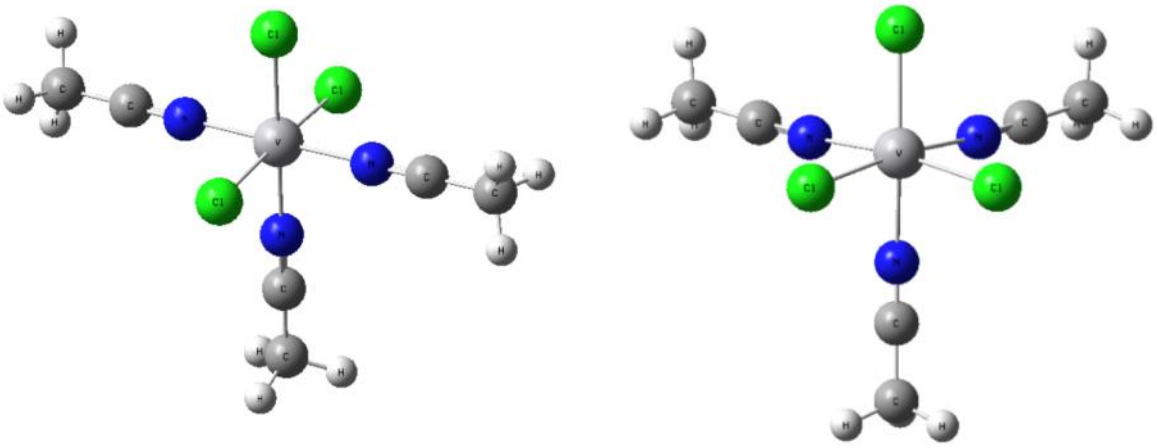

Figure 43. Mer (left) and fac (right) structures of $VCl_3(MeCN)_3$.

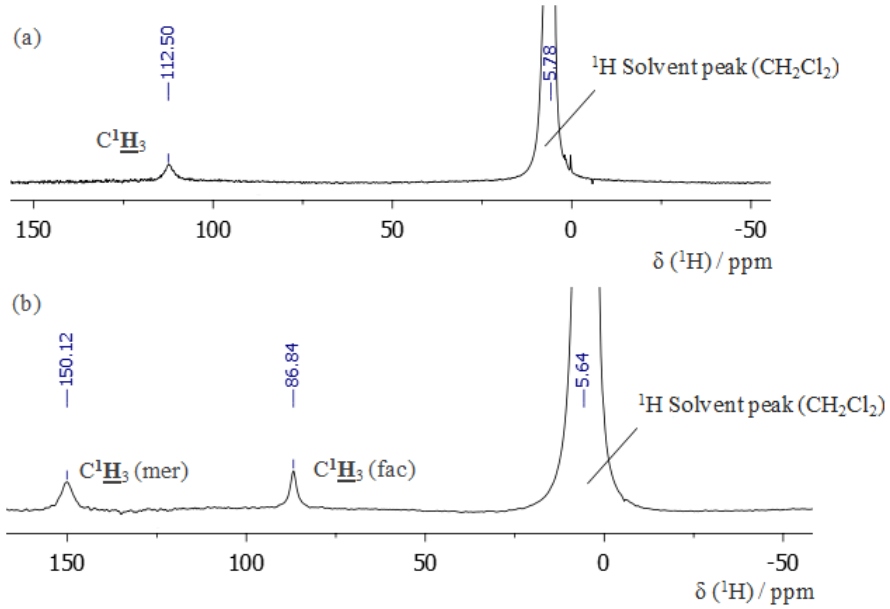

Figure 44. ^{1}H NMR spectra of $VCl_3(MeCN)_3$ in CH_2Cl_2 at (a) room temperature and (b) -35℃.

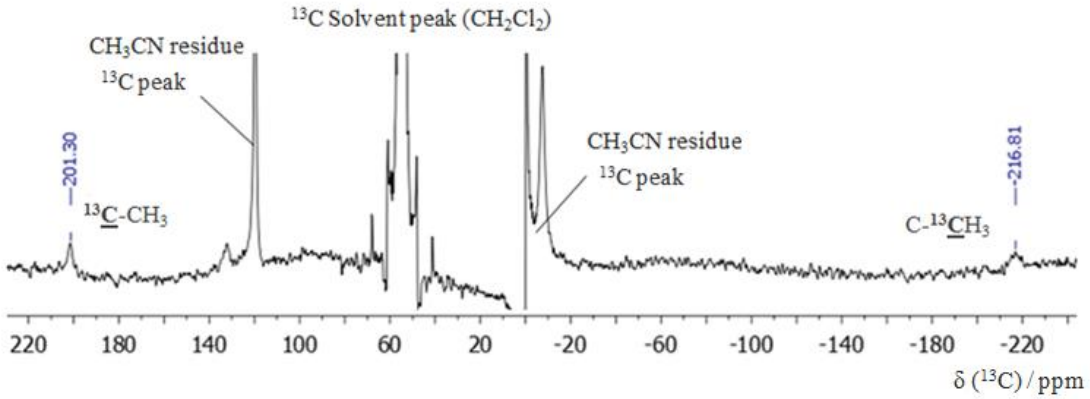

Figure 45. ^{13}C NMR spectrum of $VCl_3(MeCN)_3$ in CH_2Cl_2 at room temperature.

Due to the long electron relaxation time of VO^{2+}, it is difficult to observe NMR signals from $VO(acac)_2$. While two ^1H signals were observed in Fig.46, only the ^{13}C peak from $-CH_3$ groups was detected, as shown in Fig.47. ^1H's from the methyl groups have a very small chemical shift around 4 ppm. This peak overlaps with signals from DMF. Due to its small hyperfine coupling constant, experimental value of A_{iso} cannot be obtained from the variable temperature experiments. The C-^{1}**H** peak is much broader, having a large chemical shift of 33 ppm. Comparing with the NMR peaks from V^{3+} compounds, line broadenings for the signals from the VO^{2+} compound are significant. In the ^{13}C spectrum shown in Fig.47, one may notice that all the solvent signals have shifted by about 5 ppm. This effect may be caused by the free DMF binding to the compound in the solution.

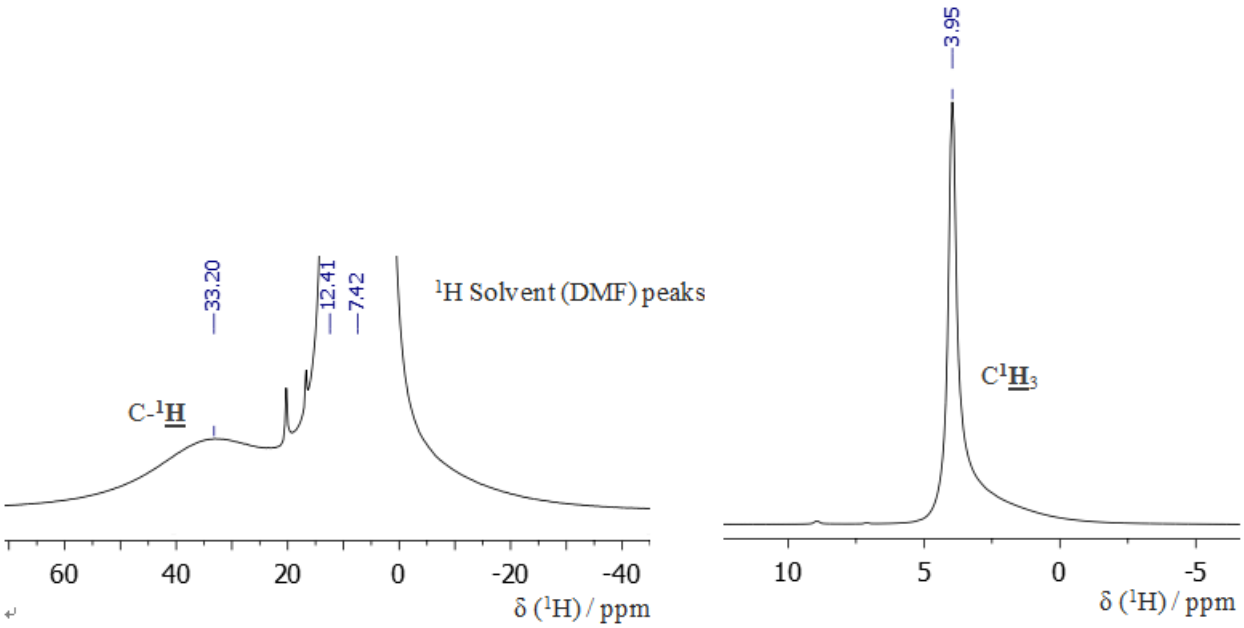

Figure 46. ^1H NMR spectra of (a) $VO(acac)_2$ in DMF (b) $VO(acac)_2$ in $CDCl_3$.

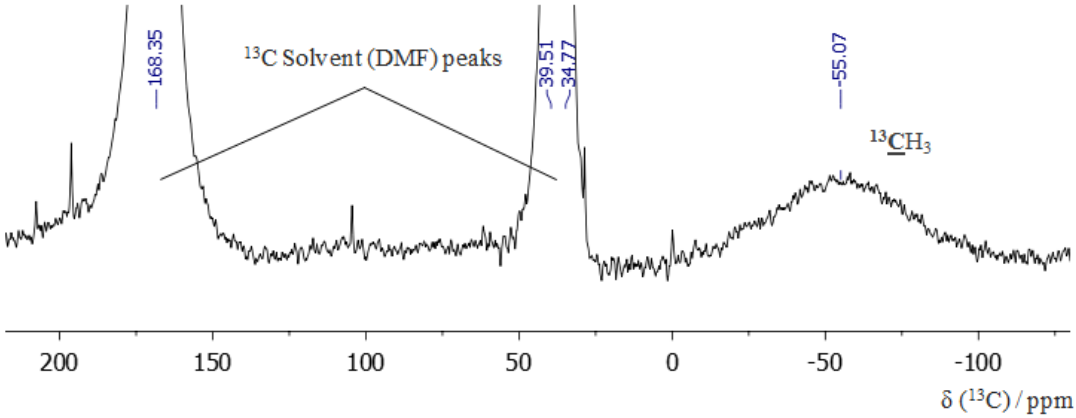

Figure 47. ^{13}C NMR spectrum of $VO(acac)_2$ in DMF.

Whenever a NMR signal was observed from a vanadium compound, variable temperature experiments were also performed to obtain more reliable values of A_{iso}. In §2.4.1, the method to measure A_{iso} experimentally was explained. For paramagnetic compounds, the solvent signals are also affected by the temperature, although not significantly. Therefore, the chemical shifts reported in the δ vs. 1/T plots were the δ differences between the compound signals and referenced solvent signals. Linear plots of ^{17}O, ^{1}H and ^{13}C signals of $V(acac)_3$ were shown as examples in Figs.48 and 49. Other plots can be found in Appendix II.

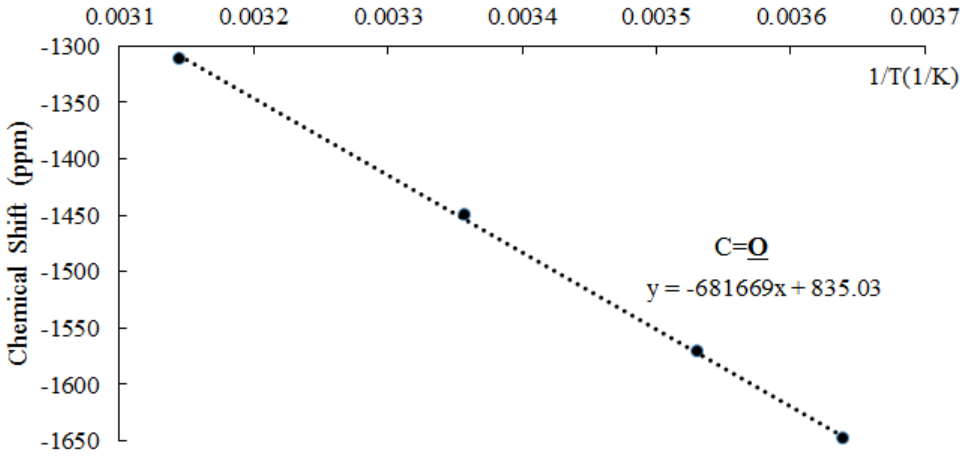

Figure 48. δ vs. 1/T plot of ^{17}O NMR signal for $V(acac)_3$.

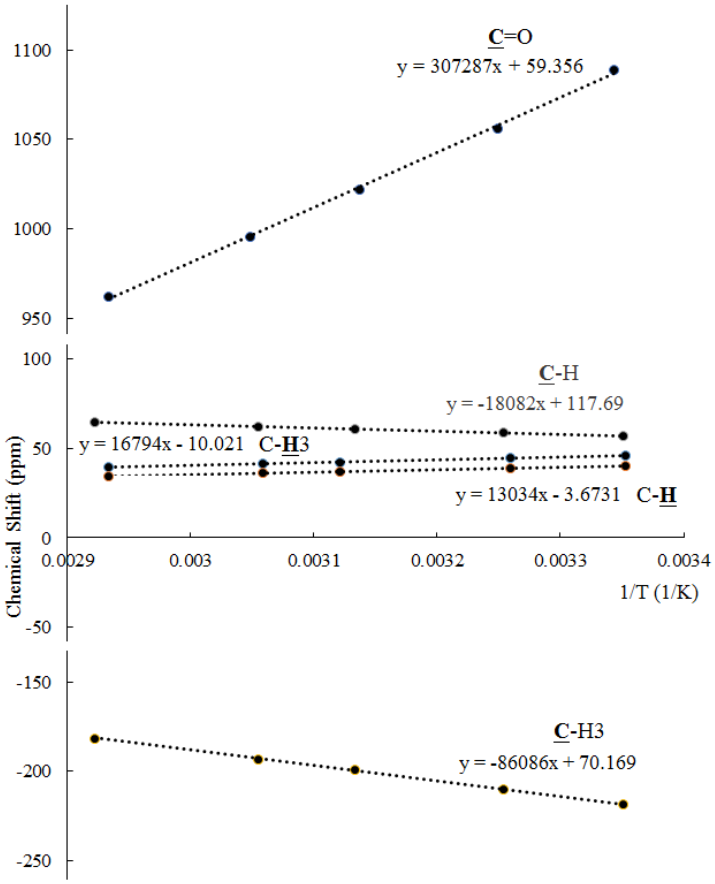

Figure 49. δ vs. 1/T plots for ^{1}H and ^{13}C NMR signals from $V(acac)_3$.

As mentioned earlier, $V(acac)_3$ has a complete set of NMR parameters from both the literature and our work. Therefore, this system was used to test the capability of the computational methods. The hyperfine coupling constants and chemical shifts results are listed in Table 7. For Gaussian09 calculations, the embedded basis sets in Gaussian09 are not complete enough for vanadium in order to give good results. The customized basis set Wachsters+f[147] was decided to be the best fit for V. Results from others were off the experimental values to some extent, such as the Weigend Coulomb Fitting in the table. Except for the Weigend basis set[148] which gives clear significantly offsets, most of the basis sets in the table produced reasonable

results. For the consideration of correctness, completeness as well as time consuming problem, the combination of Watchters+f[147] and EPR-II[99] for Gaussian09 was chosen to apply to calculate all the other compounds while the QZ4P and jcpl group was used in ADF2016. Anisotropic A-tensor calculations for each compound are provided in Appendix I.

Table 7. Testing various computational methods with experimental data obtained for $V(acac)_3$.

G09[a] Watchters+f EPR-II	G09 Watchters+f 6-311++g	G09 Weigend EPR-II	ADF DZ	ADF TZP	ADF TZ2P	ADF QZ4P	ADF jcpl[b]	Exp.	Liter.
A_{iso}(MHz)[c]									
1.85	1.66	-0.65	1.69	2.20	2.07	2.31	2.27	4.39	
3.40	3.37	0.81	3.43	3.75	3.62	3.42	3.46	3.67	
-0.03	-0.13	2.18	0.07	-0.25	-0.22	-0.15	-0.13	-0.22	
-1.08	-1.11	-2.59	-1.10	-1.15	-1.10	-1.07	-1.06	-1.03	
0.70	0.73	0.18	0.90	0.69	0.67	0.64	0.66	0.62	
0.85	0.88	-0.23	1.06	0.96	0.96	0.90	0.91	0.80	
δ(ppm)[c]									
-600	-472	701	-520	-770	-704	-821	-801	-1451	-1250[44]
1139	1138	414	1141	1254	1219	1170	1174	1090	1100[142]
85	63	709	104	36	45	71	73	57	40[142]
-275	-286	-700	-299	-286	-275	-257	-263	-219	-180[142]
56	54	16	77	56	54	52	53	40	40[143]
63	68	-9	77	70	70	67	67	46	45[143]

[a]Watchters+f[147] basis set was used for V. EPR-II[99] basis set was used for all the other atoms. Similar rules apply to the rest of G09 calculations. [b]QZ4P basis set was used for V. jcpl was used for all the other atoms (not available for V). [c]Calculation results are averaged from all equivalent positions.

For a straightforward view of the calculation quality, Correlation graphs of computational results using chosen basis sets combinations from G09 and ADF2016 versus experimental δ results for $V(acac)_3$ are plotted in Fig.50. For this small system the two software products produce results of similar quality.

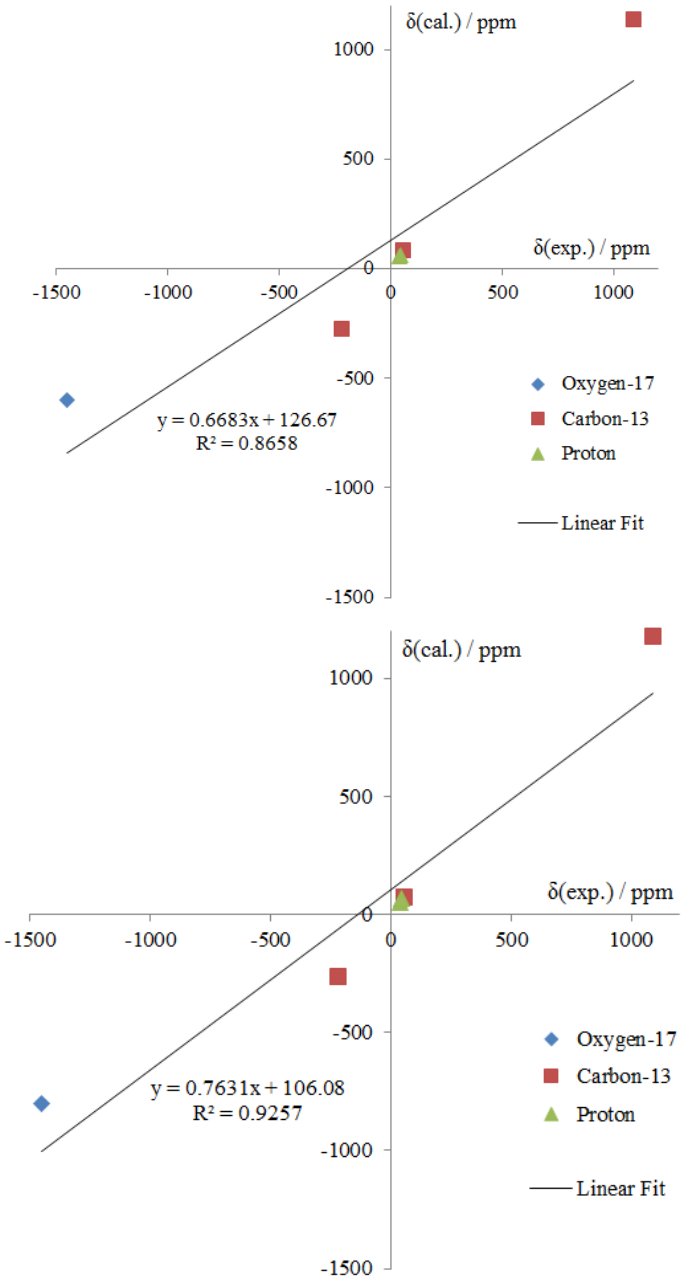

Figure 50. Correlation graphs of computational results from G09 with EPR-II (upper) and ADF2016 with jcpl (lower) versus experimental δ results for $V(acac)_3$.

In Table 8, the calculation, experimental and literature results of hyperfine coupling constants (in MHz) and chemical shifts (in ppm) of all small V systems are summarized together. The basis sets used are Watchters+f and EPR-II for Gaussian09 and QZ4P and jcpl for ADF2016. Correlation graphs are plotted as in Fig.51. The consistency of the values shows validity of our calculation and experimental methods.

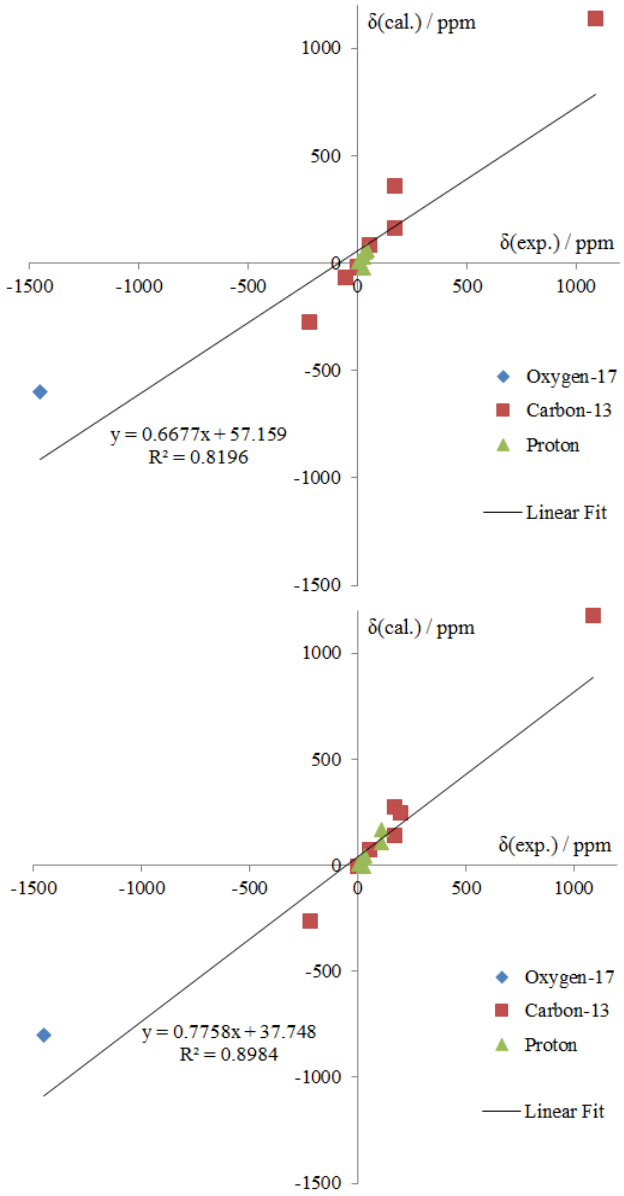

Figure 51. Correlation graphs of computational results from G09 (upper) and ADF (lower) versus experimental δ results for the four compounds shown in Table 8.

Table 8. Summary of experimental and computational solution-state NMR results of V compound systems.

Compound	Atoms	A_{iso}(G09)	A_{iso}(ADF)	A_{iso}(Exp.)	δ(G09)	δ(ADF)	δ(Exp.)
$V(acac)_3$	V-^{17}**O**	1.85	2.27	4.39	-600	-801	-1451
	^{13}**C**=O	3.40	3.46	3.67	1139	1174	1090
	C-^{13}**C**-C	-0.03	-0.13	-0.22	85	73	57
	^{13}**C**-H_3	-1.08	-1.06	-1.03	-275	-263	-219
	C-^{1}**H**	0.70	0.66	0.62	56	53	40
	C-^{1}**H**$_3$	0.85	0.91	0.80	63	67	46
$VCl_3(THF)_3$	V-^{17}**O**	3.29	2.95		-1642	-1499	
	^{13}**C**-O(eq)	0.29	0.21	0.25	160	142	173
	^{13}**C**-O(ax)	0.98	0.69	0.25	356	276	173
	^{13}**C**-C(eq)	-0.18	-0.13	-0.21	-23	-3	3
	^{13}**C**-C(ax)	-0.16	-0.14	-0.21	-17	-5	3
	O-C-^{1}**H**(eq)	0.34	0.38	0.46	29	31	27
	O-C-^{1}**H**(ax)	-0.40	-0.14	0.46	-23	-4	27
	C-C-^{1}**H**(eq)	0.04	0.03	0.12	5	5	6
	C-C-^{1}**H**(ax)	0.05	0.01	0.12	7	4	6
$VCl_3(MeCN)_3$	^{13}**C**≡N(eq)		0.43	0.02		248	201
	^{13}**C**≡N(ax)		0.23	0.02		202	201
	^{13}**C**-C(eq)		-1.06	-0.93		-294	-217
	^{13}**C**-C(ax)		-0.65	-0.93		-178	-217
	C-^{1}**H**(eq)		2.31	2.17		166	113
	C-^{1}**H**(ax)		1.45	2.17		105	113
	C-^{1}**H**(fac)		1.07	1.29			
$VO(acac)_2$	V=^{17}**O**	7.64	8.64		-279	-446	
	V-^{17}**O**	-1.09	-0.35		525	392	
	^{13}**C**=O	5.96	6.15		816	854	
	C-^{13}**C**-C	1.93	1.66		304	291	
	^{13}**C**-H_3	-0.91	-0.91	-1.03	-70	-58	-55
	C-^{1}**H**	1.70	1.53	1.05	52	47	33
	C-^{1}**H**$_3$	0.02	0.02		3	3	4

3.3.2 Transferrin

The solution-state ^{17}O NMR spectra of OTf-Al^{3+}-$[C_2{}^{17}O_4]^{2-}$ recorded on a Bruker 600 spectrometer under QCT conditions are shown in Fig.52. The spectra were acquired under the conditions of TD=4096, D1=0.005s, P1=5μs and PL1=0 with a million scans. The signal of the free $[C_2{}^{17}O_4]^{2-}$ ligands appears at 270 ppm. As seen from Fig.52, after subjecting the protein solution to further ultrafiltration, the free ligand peak disappeared. The observed QCT signals are in agreement with that reported previously.[148] This proved that our protein sample prepared was correct.

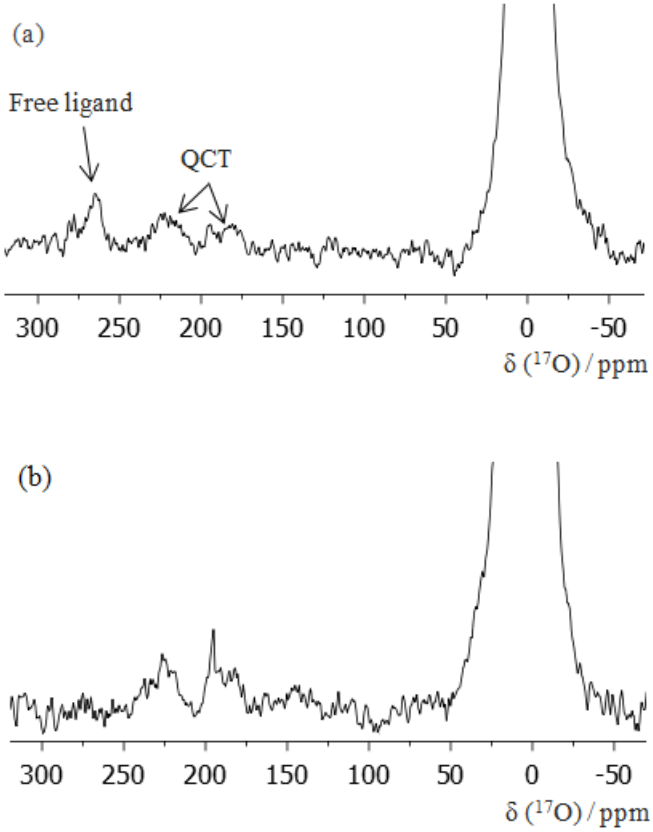

Figure 52. ^{17}O NMR spectra of OTf-Al^{3+}-$[C_2{}^{17}O_4]^{2-}$ in D_2O under QCT condition on Bruker 600 with (a) 4 times ultrafiltration and (b) 6 times ultrafiltration.

After studying the Al^{3+} diamagnetic analog of transferrin, we attempted to record the ^{17}O QCT NMR spectrum for paramagnetic OTf-V^{3+}-$[C_2{}^{17}O_4]^{2-}$. Unfortunately, all our efforts were unsuccessful. The potential reasons may be the followings. First, a protein ^{17}O NMR study in the solution state is difficult. As stated in Chapter 1, large molecules acquire short T_2 in solution which greatly broaden the peaks. Second, the V^{3+} cations with unpaired electrons will further broaden the peak with the strong hyperfine interaction. Third, the quadrupolar nucleus ^{17}O acquires a large C_Q which gives rise to broad QCT peaks in such a viscous solution. Last, but not least, the statement that V^{3+} could be stabilized by OTF binding sites may not be correct. Harris[149] had also doubted this idea with some supportive evidence. He argued that the idea of Bertini that transferrins tend to stabilize trivalent oxidation state cations was not convincible. Instead, transferrins are able to stabilize the higher oxidation state of a nucleus. Therefore, V^{3+} is oxidized into VO^{2+} or even higher oxidation state in OTF. If this statement is true, it will be very difficult to observe ^{17}O NMR signals (such as V(IV)O(acac)$_2$ as mentioned earlier). However, both ideas need more proof to be confirmed. Potential new methods are required to differentiate the binding with two oxidation states.

Fig.53 shows the solid-state ^{17}O NMR spectra of $K_3V(C_2{}^{17}O_4)_3{\bullet}3H_2O$ and OTf-V^{3+}-$[C_2{}^{17}O_4]^{2-}$ acquired on the Bruker 900 spectrometer. Compared with the ^{17}O spectrum obtained for $K_3V(C_2{}^{17}O_4)_3{\bullet}3H_2O$, the S/N in the spectrum of OTf-V^{3+}-$[C_2{}^{17}O_4]^{2-}$ is too low. It is very difficult to distinguish any peak from such a spectrum. More efforts are needed on resolving the signals.

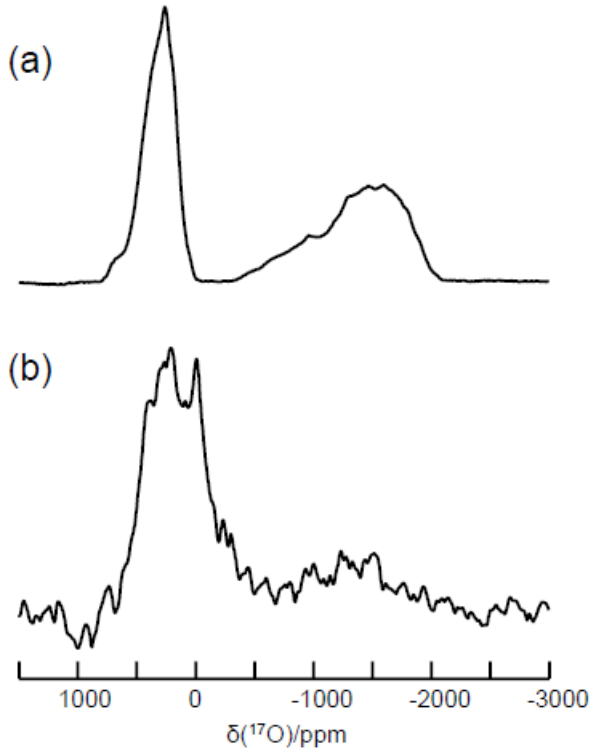

Figure 53. Solid-state ^{17}O NMR spectra of (a) $K_3V(C_2{}^{17}O_4)_3 \cdot 3H_2O$ and (b) OTf-V^{3+}-$[C_2{}^{17}O_4]^{2-}$ obtained at 21.1T. The spectra were obtained by Dr.Victor Terskikh at the National Ultrahigh Field NMR Facility for solids (Ottawa).

3.4 Conclusions

In this chapter, we have recorded ^{1}H and ^{13}C solution-state NMR signals for small V(III) compounds, as well as ^{17}O signal of $V(acac)_3$. For the V(IV) compound $VO(acac)_2$, only ^{1}H signals and the ^{13}C signal from the methyl groups, which have small A_{iso} values, were obtained. For the calculation part, we used $V(acac)_3$ as a test model to show the validity of our computational methods. The application on the other V systems is also successful. We also confirmed the existence of two types of structures for $VCl_3(MeCN)_3$ by comparing experimental

and calculated A_{iso} values.

For the large protein system, we were able to reproduce the work of solution-state ^{17}O NMR of OTf-Al^{3+}-$[C_2{}^{17}O_4]^{2-}$. However, we were not able to obtain the ^{17}O signal for OTf-V^{3+}-$[C_2{}^{17}O_4]^{2-}$ using solution-state NMR experiment. Reasons for the unsuccessful trial are not confirmed. More efforts will be made on this experiment.

Chapter 4 NMR Studies of Paramagnetic Compounds in the Solid State

4.1 Overview

In solid-state NMR, most line shapes are dominated by anisotropic interactions. These interactions, such as the anisotropic dipolar interaction, are direction dependent and thus they give rise to irregular line shapes. The anisotropic interactions also cause great line broadenings. For example, line broadening caused by the quadrupolar interaction can reach over several MHz. Solid-state NMR is generally considered to be much more difficult than solution-state NMR. However, it can be advantageous for studying proteins with large molecular weights that are beyond solution-state NMR's capability.

Solid-state NMR studies of paramagnetic compounds are very rare. Due to the limitations of experimental solid-state NMR data, in this chapter we focus on only one paramagnetic Cu(II) (S = 1) compound, Cu(DL-alanine)$_2$•H$_2$O as shown in Fig.54.

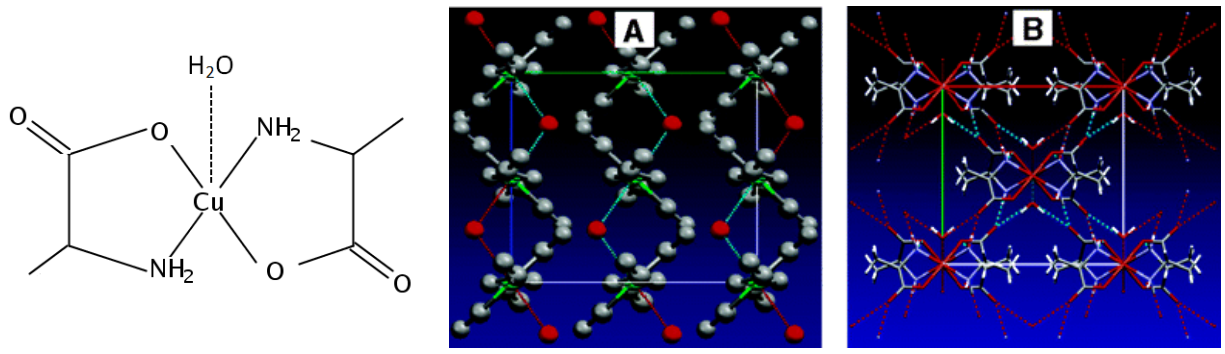

Figure 54. Molecular structure (left) and crystal structure (right) of Cu(DL-alanine)$_2$•H$_2$O viewing along (A) a axis and (B) c axis.[150]

We decided to choose this compound because it has the most complete set of NMR results available from the literature. Unlike the calculations of the small paramagnetic compounds for solution-state NMR studies, taking only one molecule into consideration in the calculation is clearly not sufficient for the solid-state NMR studies. As seen in Fig.55, calculation results from models with only 1 or even 3 Cu atoms have large offsets with the experimental values.[104] However, increasing computational model size to include 9 Cu atoms gives reasonable results. Therefore, BAND is chosen to perform the calculations since it works on periodic systems.

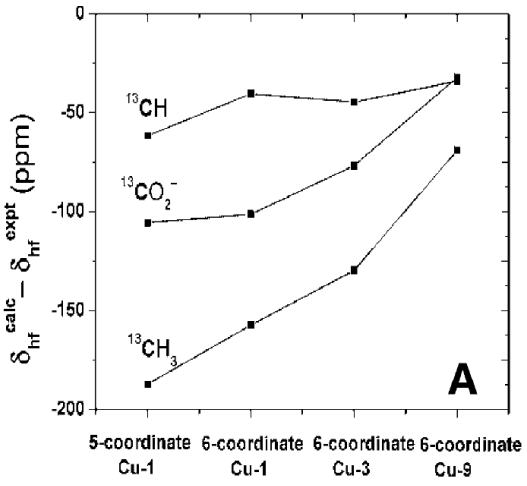

Figure 55. Error of calculated hyperfine shifts in different structure models of $Cu(DL\text{-alanine})_2 \cdot H_2O$.[150]

Based on the literature experimental results, BAND features tests were carried out. We aimed to discover BAND's capability and to figure out the best method to calculate A-tensors.

4.2 Computational Details

All calculations in this chapter were performed with the BAND package in ADF2016.

As mentioned in Chapter 2, BAND does not allow NMR shielding calculations for paramagnetic systems. A-tensor calculations were performed with combinations of different basis sets and DFT exchange functionals including ZORA relativistic effect using TZ2P basis set for all atoms. Three structures were used as test models, original structure from literature report,[150] LDA VWN optimized structure, GGA BP86 optimized structure. For each structure, calculations were carried out by the following functionals: LDA VWN, GGA BP86, GGA PBE, GGA mPBE, GGA BLYP and GGA revPBE. In §2.4.2.3, two approaches of calculating A-tensors were explained. For each combination, both approaches were included to check their accuracies. Full A-tensors were pulled out to compare with experimental results. Correlation graphs of each combination were plotted to see the consistencies straightforwardly. In this chapter, all A-tensor values are reported in MHz.

4.3 Results and Discussions

Experimental results of both isotropic and anisotropic A-tensors of some atoms of $Cu(DL\text{-alanine})_2 \bullet H_2O$ are obtained from several literature reports.[150-153] These results were obtained from either solid-state NMR or ENDOR studies. Experimental results of A-tensor components (in MHz) for $Cu(DL\text{-alanine})_2 \bullet H_2O$ are summarized in Table 9. Slopes and value of R^2 of the fittings for all the correlation graphs are listed in Table 10. Refer to Appendixes III and IV for full A-tensors.

Table 9. Experimental A-tensor results in MHz obtained from the literature for $Cu(DL\text{-alanine})_2 \bullet H_2O$.

Atoms	A_{iso}	T_{11}	T_{22}	T_{33}	References
C=**O**	-1.80	2.39	0.42	-2.81	44
H_2**O**	1.50				44
C=O	-3.76	-3.30	1.65	1.65	150, 151
C-**C**-H	-3.27	-1.60	0.80	0.80	150, 151
C-H_3	1.89	-0.27	-0.27	0.55	150, 151
N-**H**	-6.70	-7.63	-2.43	10.05	150, 152
N-**H**	-5.70	-6.76	-2.72	9.48	150, 152
C-**H**	0.32	-3.90	1.10	2.80	150, 152
C-**H**$_3$	1.18	-2.49	0.00	2.49	150, 152
H$_2$O	0.90				44

After evaluating all the data in Table 10, we decided that BLYP appears to be the best fitting functional for A-tensor calculations. The LDA VWN functional produced less accurate A-tensor data than the GGA functional. However, VWN optimized structure seems to be better than BP86 optimization. Correlation graphs of the results from the BLYP functional for isotropic and anisotropic A-tensor components using two optimized structures are plotted in Figs.56 and 57.

Table 10. A summary of slope/R^2 values from correlation graphs for isotropic (A_{iso}) and anisotropic (T_{ii}) A-tensor components.

	Model	Method	VWN	BP86x	PBEx	mPBE	BLYP	revPBE
A_{iso} Slope/R^2	Orig.	Gradient	1.32/0.55	1.46/0.57	1.44/0.57	1.45/0.57	1.46/0.57	1.47/0.57
		Density	0.83/0.83	0.96/0.92	0.93/0.92	0.94/0.93	0.96/0.92	0.96/0.93
	VWN Opt.	Gradient	1.40/0.59	1.51/0.60	1.48/0.59	1.49/0.59	1.52/0.60	1.52/0.60
		Density	0.85/0.82	0.94/0.91	0.91/0.91	0.92/0.92	0.95/0.92	0.94/0.92
	BP86 Opt.	Gradient	1.36/0.58	1.46/0.59	1.44/0.58	1.44/0.58	1.47/0.59	1.47/0.58
		Density	0.83/0.82	0.92/0.90	0.89/0.90	0.90/0.91	0.93/0.91	0.92/0.91
T_{ii} Slope/R^2	Model	Method	VWN	BP86x	PBEx	mPBE	BLYP	revPBE
	Orig.	Gradient	1.30/0.90	1.24/0.80	1.30/0.91	1.30/0.91	1.30/0.91	1.30/0.91
		Density	1.09/0.85	1.05/0.85	1.04/0.85	1.04/0.85	1.06/0.86	1.04/0.85
	VWN Opt.	Gradient	1.18/0.92	1.19/0.92	1.18/0.92	1.18/0.92	1.18/0.92	1.18/0.92
		Density	0.94/0.88	0.91/0.88	0.90/0.88	0.90/0.88	0.91/0.89	0.90/0.89
	BP86 Opt.	Gradient	1.17/0.92	1.17/0.92	1.16/0.92	1.17/0.92	1.17/0.92	1.17/0.92
		Density	0.93/0.88	0.90/0.88	0.89/0.88	0.89/0.88	0.90/0.88	0.89/0.88

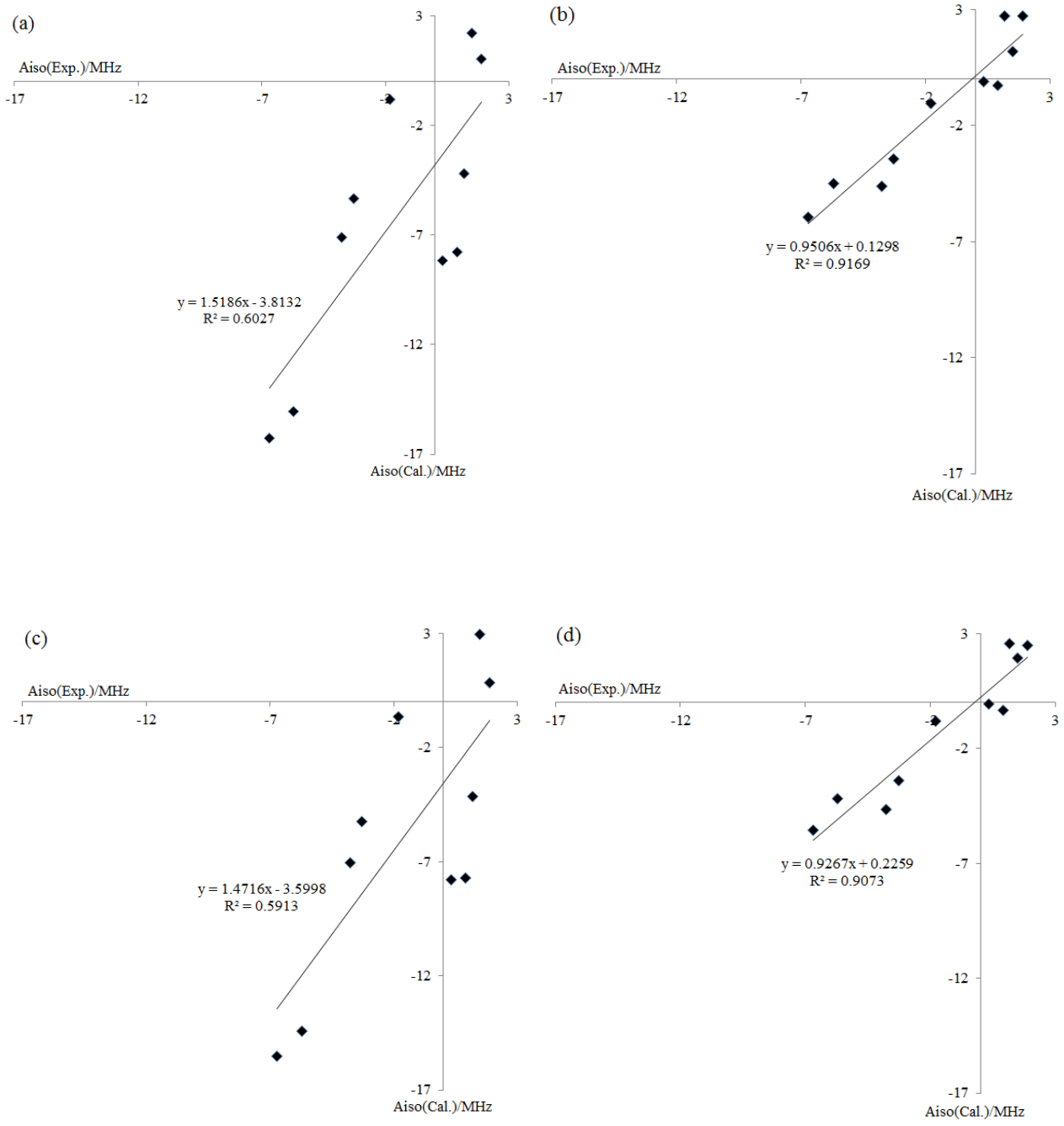

Figure 56. Correlation between experimental vs. computational A_{iso} values for (a) VWN via gradient (b) VWN via density (c) BP86 via gradient (d) BP86 via density.

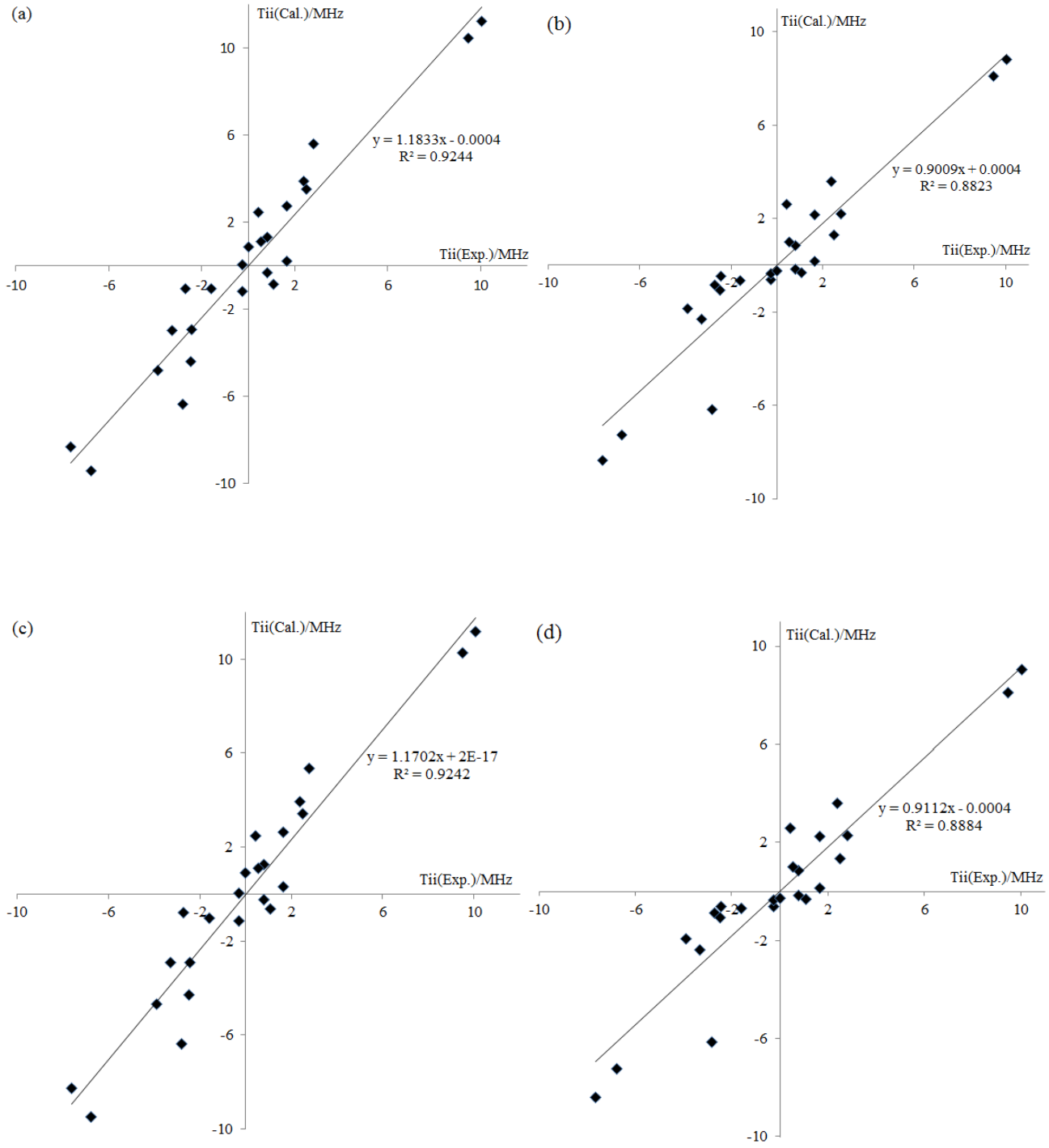

Figure 57. Correlation between experimental vs. computational T_{ii} values for (a) VWN via gradient (b) VWN via density (c) BP86 via gradient (d) BP86 via density.

From Table 10 and Figs. 56 and 57, it can be seen that the gradient and density approaches produce quite different A_{iso} values. The A_{iso} results from the gradient approach are way off the experimental values. Results from the density approach are acceptable for prediction purpose. The difference between these two methods was mentioned in §2.4.2.3. The gradient method calculates A_{iso} with an integral term, and the density approach involves no integrations. In principle, the gradient method should be more accurate since it integrates over a smoother function. However, the results show the opposite fact. The reasons behind this phenomenon are not yet confirmed. Some conjectures are made to explain this fact here. First, in Kadantsev and Ziegler's work,[124] after explaining algorithms of the two approaches they stressed that to apply gradient approach "one has to construct gradient of Bloch basis set functions". In another study[153] they explained in details the implementation of energy gradient especially for BAND. They emphasized that none of the existing energy gradients are suitable for BAND's special algorithm. Since no one has reported academic works related to NMR or ESR calculations using BAND, the quality of their new functions are still doubtful. Although they test on the gradient method by comparing results from BAND and ADF, those models are just single atoms. From our work one can tell that the results from large paramagnetic systems are not reliable. Second, the integrations of A-tensor calculations are based on Wigner-Seitz (WS) cell. From Eq.100, one can tell that the gradient approach assumes that the spin density is localized inside the WS cell. If the WS cell is not large enough so the spin density is not all included inside, the interactions between the cells will affect the result significantly. It is also the reason that the user's guide of BAND suggests no diffuse functions should be included. This effect could be much more

impressive than the quality of integrations. That might explain why the density approach is more precise. Finally, we also noticed that despite the big differences between A_{iso} values of the two approaches, the qualities of anisotropic components are similar. In most cases, the gradient approach has slightly better consistency than the density approach. This also happens to the comparison of results from LDA and GGA functionals. These indicate that it is only a part of the integration in Eq.100 that affects the quality of this approach. While some inquiries had been sent to the technical group of SCM (producer of the software), no solutions have been found to solve this problem. More insights are needed in the future to help to improve the calculation quality.

4.4 Conclusion

By performing A-tensor calculations with various structures and exchange functionals, we have shown that the density approach is more precise than the gradient approach, especially for A_{iso} values. We also found that the LDA functional is good at optimization while the GGA functional produce better A-tensor results. Overall, BAND is a powerful tool to calculate A-tensors in periodic systems. It is also necessary to test more solid systems when experimental A-tensors are available.

Chapter 5 Conclusions and Future Work

NMR studies of paramagnetic compounds are challenging as expected. For solution-state NMR studies, our test on DFT calculations for $V(acac)_3$ on hyperfine coupling constant and diamagnetic shielding has produced accurate results as compared with experimental results. The application of the same computational method to other small vanadium compounds turned out to be successful. With the aid of quantum chemical calculations, we were able to predict every signal that could be obtained from NMR experiments. Furthermore, the experimental results are reasonable from every aspect, such as the extent of line broadenings based on the relaxation effects as well as the electron relaxation times, and the hyperfine shifts with respect to the distance of the nuclei from the paramagnetic center of vanadium ions. For example, we were only able to observe two NMR signals for $VO(acac)_2$ because the electron relaxation time is long for V(IV). The ^{1}H and ^{13}C signals from the methyl groups were observed because they have small hyperfine coupling constants, and the line broadening is significantly greater than those methyl groups signals from V(III) compounds. In addition, based on the different ^{1}H NMR signals we observed at different temperatures as well as the hyperfine constants calculated from variable temperature NMR experiments, we further proved the co-existence of both fac and mer structures for $VCl_3(MeCN)_3$ at low temperatures. Our success on studying the paramagnetic vanadium compounds shows the reliability of the theory and computational methods. ^{17}O NMR studies of paramagnetic proteins were even more difficult. Although it is proved that the ^{17}O signal can be obtained from oxygen atoms bonded to paramagnetic center, it turned out that it is not necessarily true for large molecules. We were

unable to detect ^{17}O NMR signal in OTF-V^{3+}-$[C_2{}^{17}O_4]^{2-}$ in solution. The low S/N ratio on our ^{17}O spectrum for OTF-V^{3+}-$[C_2{}^{17}O_4]^{2-}$ at a high magnetic field may be due to the line broadening with extreme short relaxation time for the macromolecule. It is also probably true that the previous work stating that OTF-V^{3+}-$[C_2{}^{17}O_4]^{2-}$ to be a stable compound is not correct. In the end, detecting ^{17}O NMR signals from large paramagnetic systems remains to be a challenge. For solid-state NMR studies, we have tested a periodic DFT software BAND using solid-state NMR data reported for Cu(DL-alanine)$_2$•H_2O. This is the first time that BAND is used to study paramagnetic molecular solids. Isotropic hyperfine constants computed with the gradient approach are not as precise as expected, but the density approach gives reliable results. Both approaches produce reasonable anisotropic A-tensor components. This study lays a solid foundation for further computational studies of other paramagnetic compounds in the solid-state. The problems aroused from our BAND calculations also show the fact that the computational theory for paramagnetic periodic systems are still not mature. For one thing, the program itself cannot deal with paramagnetic NMR shielding tensors. For another, the results of the isotropic A-tensors from the gradient approach were far less accurate from expectations. The differences in our test of the approach on this large periodic system and the test on systems of single molecules may show that the theory behind the gradient approach is not widely applicable. It also shows the fact that the implementation of theory is always not easy. Although the calculation from the gradient approach is supported by the theory via modifying the basis set, it is not implemented well.

In the future, more efforts will be made to solve the existing problems. Reasons

behind the unsuccessful ^{17}O NMR study of V^{3+}-binding transferrin are to be further examined. Furthermore, as solid-state ^{17}O NMR has become increasingly important for studying biological molecules,[154,155,156] it is also possible to extend it to paramagnetic metalloproteins. Since we already tested the applicability of the computational methods of BAND, we can use it for other paramagnetic periodic systems. It is also desirable to expand the test set for BAND in order to further prove its usefulness. For example, several works had reported the data of $CuCl_2 \cdot 2H_2O$, including the structural information,[157] the g-tensor components,[158] point dipole calculations[159] and single crystal data of hyperfine tensors.[160] In particular, Walder reported the method to determine the paramagnetic shifts of $CuCl_2 \cdot 2H_2O$ using 2D NMR.[161] Using the method they reported, the BAND calculations and the ^{17}O labeled sample $CuCl_2 \cdot 2H_2O$ in our lab, we can perform a series of studies on ^{17}O NMR. Another potential sample is MnO and CoO. Some experimental and computational data of ^{17}O NMR shifts had been reported before.[162] We can use their results as references to improve the data using BAND and high resolution solid-state NMR. We will also continue helping BAND with testing and improving the program for ESR and NMR calculations.

References

(1) Anthea, M.; Hopkins, J.; McLaughlin, C. W.; Johnson, S.; Warner, M. Q.; LaHart, D.; Wright, J. D. In *Human Biology and Health*. Englewood Cliffs, New Jersey, US: 1993.

(2) Linberg, R.; Conover, C. D.; Shum, K. L.; Shorr, R. G. Hemoglobin based oxygen carriers: how much methemoglobin is too much. *Artif Cells Blood Substit Immobil Biotechnol*. **1998**, *26*, 133-148.

(3) Keller, H. J.; Schwarzhans, K. E. Magnetic resonance of paramagnetic complexes. *Angew. Chem. Int. Ed*. **1970**, *9*, 196-205.

(4) Paula, Q. A.; de Batista, A. A.; Nascimento, O. R.; Costa-Filho; Antonio, J. D., Schultz, M. S.; Bonfadini, M. R.; Oliva, G. EPR and electrochemistry of $[NH_4]$trans-$[RuCl_4(DMSO)(L)]$ complexes (L = DMSO, py). X-ray molecular structure of $[pyH][RuCl_4(DMSO)(py)]$. *J. Braz. Chem. Soc.* **2000**, *11*, 530-536.

(5) Kihler, F. H. Paramagnetic complexes in solution: the NMR approach. In *eMagRes*. John Wiley: 2007.

(6) Bloch, F.; Hansen, W. W.; Packard, M. Nuclear induction. *Phys. Rev.* **1946**, *69*, 127-127.

(7) Purcell, E. M.; Torrey, H. C.; Pound, R. V. Resonance absorption by nuclear magnetic moments in a solid. *Phys. Rev.* **1946**, *69*, 37-37.

(8) Bloembergen, N.; Purcell, E. M.; Pound, R. V. Relaxation effects in nuclear resonance absorption. *Phys. Rev.* **1948**, *73*, 679-712.

(9) Bloembergen, N.; Dickinson, W. C. On the shift of the nuclear magnetic resonance in paramagnetic solutions. *Phys. Rev*. **1950**, *79*, 179-180.

(10) Dickinson, W. C. The time average magnetic field at the nucleus in nuclear magnetic resonance experiments. *Phys. Rev.* **1951**, *81*, 717-731.

(11) McConnell, H. M.; Holm, C. H. Proton resonance shifts in nickelocene. *J. Chem. Phys.* **1957**, *26*, 315-324.

(12) McConnell, H. M.; Robertson, R. E. Isotropic nuclear resonance shifts. *J. Chem. Phys.* **1958**, *29*, 1361-1365.

(13) McConnell, H. M.; Chesnut, D. B. Theory of isotropic hyperfine interactions in pi-electron radicals. *J. Chem. Phys.* **1958**, *28*, 107-117.

(14) Bernheim, R. A.; Brown, T. H.; Gutowsky, H. S.; Woessner, D. E. Temperature dependence of proton relaxation times in aqueous solutions of paramagnetic ions. *J. Chem. Phys.* **1959**, *30*, 950-956.

(15) Bloembergen, N.; Morgan, L. O. Proton relaxation times in paramagnetic solutions. Effects of electron spin relaxation. *J. Chem. Phys.* **1961**, *34*, 842-850.

(16) Fermi, E. Uber die Magnetischen Momente der Atomkerne. *Physik*. **1930**, *60*, 320-333.

(17) Bloembergen, N. Proton relaxation times in paramagnetic solutions. *J. Chem. Phys.*, **1955**, *27*, 572-573.

(18) Solomon, I. Relaxation processes in a system of two spins. *Phys. Rev.* **1955**, *99*, 559-565.
(19) Jesson, J. P. The paramagnetic shift. in *Ref. 5*. **1973**, 1-83.
(20) Jesson, J. P. Theory of isotropic nuclear resonance shifts in octahedral cozt systems. *J. Chem. Phys.* **1967**, *47*, 579-581.
(21) Kurland, R. J.; McGarvey, B. R. Isotropic NMR shifts in transition metal complexes: the calculation of Fermi contact and pseudocontact terms. *J. Magn. Reson*. **1970**, *2*, 230-286.
(22) Iwahara, J.; Tang, C.; Clore, G. M. Practical aspects of ^{1}H transverse paramagnetic relaxation enhancement measurements on macromolecules. *J. Magn. Reson.* **2007**, *184*, 185-195.
(23) Bertini, I.; Luchinat, C.; Parigi, G. Magnetic susceptibility in paramagnetic NMR. *Prog. Nucl. Magn. Reson. Spectrosc.* **2002**, *40*, 249-273.
(24) Bertini, I.; Janik, M. B.; Lee, Y. M.; Luchinat, C.; Rosato, A. Magnetic susceptibility tensor anisotropies for a lanthanide ion series in a fixed protein matrix. *J. Am. Chem. Soc.* **2001**, *123*, 4181-4188.
(25) Otting, G. Prospects for lanthanides in structural biology by NMR. *J. Biomol. NMR.* **2008**, *42*, 1-9.
(26) Tolman, J. R.; Al-Hashimi, H. M.; Kay, L. E.; Prestegard, J. H. Structural and dynamic analysis of residual dipolar coupling data for proteins. *J. Am. Chem. Soc.* **2001**, *123*, 1416-1424.
(27) Canales, A.; Jiménez-Barbero, J.; Martín-Pastor, M. Review: use of residual dipolar couplings to determine the structure of carbohydrates. *Magn. Reson. Chem.* **2012**, *50*, 80-85.
(28) Wohnert, J.; Franz, K. J.; Nitz, M.; Imperiali, B.; Schwalbe, H. Protein alignment by a coexpressed lanthanide-binding tag for the measurement of residual dipolar couplings. *J. Am. Chem. Soc.***2003**, *125*, 3338-3339.
(29) Wuthrich, K.; In *NMR in biological research: peptides and proteins*. North-Holland, Amsterdam: 1976.
(30) Mathias A. H.; Marcellus, U. Structure determination of protein–protein complexes with long-range anisotropic paramagnetic NMR restraints. *Curr. Opin. Struct. Biol*. **2014**, *24*, 45-53.
(31) McDonald, C. C.; Phillips, W. D. Perturbation of the PMR spectrum of lysozyme by Co^{2+}. *Biochem. Biophys. Res. Commun.* **1969**, *35*, 43-51.
(32) Zhang, Y.; Yamaguchi, T.; Kato, K. New NMR tools for characterizing the dynamic conformations and interactions of oligosaccharides. *Chem. Lett.* **2013**, *42*, 1455-1462.
(33) Chacko, V. P.; Ganapathy, S.; Bryant, R. G. ^{13}C CP-MAS NMR spectra of paramagnetic solids. *J. Am. Chem. Soc*. **1983**, *105*, 5491-5492.
(34) Ganapathy, S.; Chacko, V. P.; Bryant, R. G.; Etter, M. C. Carbon CP-MAS NMR and X-ray crystal-structure of paramagnetic lanthanide acetates. *J. Am. Chem. Soc.* **1986**, *108*, 3159-3165.

(35) Walter, T. H.; Oldfield, E. Magic-angle sample-spinning NMR spectroscopy of an antiferromagnetically coupled copper formate dimer. *J. Chem. Soc. Chem. Commun.* **1987**, 646-647.

(36) Nayeem, A.; Yesinowski, J. P. Calculation of magic-angle spinning nuclear magnetic resonance spectra of paramagnetic solids. *J. Chem. Phys.* **1988**, *89*, 4600-4608.

(37) Campbell, G. C.; Haw, J. F. Determination of magnetic and structural properties in solids containing antiferromagnetically coupled metal centers using NMR methods. Magneto-structural correlations in anhydrous copper(II) nbutyrate. *Inorg. Chem.* **1988**, *27*, 3706-3709.

(38) Groombridge, C. J.; Perkins, M. J. High resolution NMR of a solid organic free radical: ^{13}C, ^{2}H and ^{1}H magic angle spinning of 4-hydroxy-2,2,6,6- tetramethylpiperidine-1-oxyl (TEMPOL). *J. Chem. Soc. Chem. Commun.* **1991**, 1164-1166.

(39) Pintacuda, G.; Giraud, N.; Pierattelli, R.; Bockmann, A.; Bertini, I.; Emsley, L. Solid-state NMR spectroscopy of a paramagnetic protein: assignment and study of human dimeric oxidized CuII–ZnII superoxide dismutase (SOD). *Angew. Chem. Int. Ed.* **2007**, *46*, 1079–1082.

(40) Balayssac, S.; Bertini, I.; Lelli, M.; Luchinat, C.; Maletta, M. Paramagnetic ions provide structural restraints in solid-state NMR of proteins. *J. Am. Chem. Soc*. **2007**, *129*, 2218–2219.

(41) Andrew, E. R.; Bradbury, A.; Eades, R. G. Nuclear magnetic resonance spectra from a crystal rotated at high speed. *Nature*. **1958**, *182*, 1659-1659.

(42) Pine, A.; Gibby, M. G.; Waugh, J. S. Proton-enhanced NMR of dilute spins in solids. *J. Chem. Phys*. **1973**, *59*, 569-590.

(43) Knicker, H.; Lüdemann, H. D.; Haider, K. Incorporation studies of NH_4 during incubation of organic residues by ^{15}N-CPMAS-NMR-spectroscopy. *Eur. J. Soil. Sci.* **1997**, *48*, 431-441.

(44) Kong, X.; Terskikh, V.V.; Khade, R.L.; Yang, Liu.; Rorick, A.; Zhang, Y.; He, P.; Huang, Y.; Wu, G. Solid-State ^{17}O NMR spectroscopy of paramagnetic coordination compounds. *Angew. Chem. Int. Ed*. **2015**, *54*, 4753-4757.

(45) Barone, V.; Ciminob, P.; Pedonea, A. An integrated computational protocol for the accurate prediction of EPR and PNMR parameters of aminoxyl radicals in solution. *Magn. Reson. Chem.* **2010**, *48*, 11-22.

(46) Ramsey, N. F. Magnetic shielding of nuclei in molecules. *Phys. Rev.* **1950**, *78*, 699-703.

(47) McConnell, H. M.; Chesnut, D. B. Theory of isotropic hyperfine interactions in electron radicals. *J. Chem. Phys*. **1958**, *28*, 107-117.

(48) Kurland, R. J.; McGarvey, B. R. Isotropic NMR Shifts in transition metal complexes: the calculation of the Fermi contact and pseudocontact terms. *J. Magn. Reson*. **1970**, *2*, 286-301.

(49) Vaara, J., Chemical shift in paramagnetic systems. In *High resolution nuclear magnetic resonance parameters for understanding molecules and their electronic structure*. Science & Technology of Atomic, Molecular, Condensed Matter & Biological Systems, Elsevier, Amsterdam: 2013.

(50) Gendron, F.; Sharkas, K.; Autschbach, J. Calculating NMR chemical shifts for paramagnetic metal complexes from first-principles. *J. Phys. Chem. Lett.* **2015**, *6*, 2183–2188.

(51) Pilla, K. B.; Gaalswyk, K.; MacCallum, J. L. Molecular modeling of biomolecules by paramagnetic NMR and computational hybrid methods. *BBA-Proteins Proteom.* **2017**. *In press.*

(52) Bloembergen, N.; Purcell, E. M.; Pound, R. V. Relaxation effects in nuclear magnetic resonance absorption. *Phys. Rev*. **1948**, *73*, 670-746.

(53) Harris, R. K. In *Nuclear Magnetic Resonance Spectroscopy*. The Bath Press: 1986.

(54) Cohen, M. H.; Reif, F. Quadrupole effects in nuclear magnetic resonance studies of solids. *Solid State Phys.* **1957**, *5*, 321-438.

(55) Samoson, A.; Kundla, E.; Lippmaa, E. High resolution MAS-NMR of quadrupolar nuclei in powders. *J. Magn. Reson.* **1982**, *49*, 350-357.

(56) Behrens, H. J.; Schnabel, B. The second order influence of the nuclear quadrupole interaction on the central line in the NMR of quadrupolar nuclei using rapid sample spinning. *Physica B+C.* **1982**, *114*, 185-190.

(57) Andrew, E. R.; Bradbury, A.; Eades, R. G. Removal of dipolar broadening of nuclear magnetic resonance spectra of solids by specimen rotation. *Nature*. **1959**, *183*, 1802-1803.

(58) Hartmann, S. R.; Hahn, E. L. Nuclear double resonance in the rotating frame. *Phys. Rev*. **1962**, *128*, 2042–2053.

(59) Satterlee, J. D. Fundamental concepts of NMR in paramagnetic systems part 11: relaxation effects. *Concepts. Magn. Reson*. **1990**, *2*, 119-129.

(60) Abragam, A. In *The Principles of Nuclear Magnetism*; Oxford University Press: 1961.

(61) Gueron, M. Nuclear relaxation in macromolecules by paramagnetic ions: a novel mechanism. *J. Magn. Reson.* **1975**, *19*, 58-66.

(62) Vega, A. J.; Fiat, D. Nuclear relaxation processes of paramagnetic complexes: the slow-motion case. *Mol. Phys.* **1976**, *31*, 347-355.

(63) Bertini, I.; Luchinat, C. In *NMR of Paramagnetic Molecules in Biological Systems*; Menlo Park: 1986.

(64) Jackowski, K.; Wilczek, M.; Pecul, M.; Sadlej, J. Nuclear magnetic shielding and spin−spin coupling of 1,2-^{13}C-enriched acetylene in gaseous mixtures with xenon and carbon dioxide. *J. Phys. Chem. A.* **2000**, *104*, 5955-5958.

(65) Miller, J.A.; Klippenstein, S.J.; Robertson, S.H. A theoretical analysis of the reaction between vinyl and acetylene: quantum chemistry and solution of the master equation. *J. Phys. Chem. A.* **2000**, *104*, 9806-9806.

(66) Jackowski K.; Makulski, W. *Magn. Reson. Chem.* ^{13}C shielding scale for MAS NMR spectroscopy. **2011**, *49*, 600–602.

(67) Jameson, C.J.; Jameson, A.K.; Oppusunggu, D.; Wille, S.; Burrell, P.M.; Mason, J. ^{15}N nuclear magnetic shielding scale from gas phase studies. *J. Chem. Phys*. **1981**, *74*, 81-88.

(68) Wasylishen, R. E.; Bryce, D. L. A revised experimental absolute magnetic shielding scale for oxygen. *J. Chem. Phys*. **2002**, *117*, 10061-10066.

(69) Gaussian 09, Revision A.02. Gaussian, Inc., Wallingford CT, 2016.
(70) te Velde, G.; Bickelhaupt, F. M.; Baerends, E. J.; Guerra, C. F.; van Gisbergen, S. J. A.; Snijders, J. G.; Ziegler, T. Chemistry with ADF. *J. Comput. Chem.* **2001**, *22*, 931-967.
(71) Guerra, C. F.; Snijders, J. G.; te Velde, G.; Baerends, E. J. Towards an order-N DFT method. *Theor. Chem. Acc.* **1998**, *99*, 391-403.
(72) ADF2016, SCM, Theoretical Chemistry, Vrije Universiteit, Amsterdam, The Netherlands, http://www.scm.com.
(73) te Velde, G.; Baerends, E. J. Precise density-functional method for periodic structures. *Phys. Rev. B*. **1991**, *44*, 7888-7903.
(74) Wiesenekker, G.; Baerends, E. J. Quadratic integration over the three-dimensional Brillouin zone. *J. Phys. Condens. Matter 3*. **1991**, 6721-6742.
(75) Franchini, M.; Philipsen, P. H. T.; Visscher, L. The becke fuzzy cells integration scheme in the Amsterdam density functional program suite. *J. Comput. Chem.* **2013**, *34*, 1819-1827.
(76) Franchini, M.; Philipsen, P. H. T.; van Lenthe, E.; Visscher, L. Accurate Coulomb potentials for periodic and molecular systems through density fitting. *J. Chem. Theory Comput.* **2014**, *10*, 1994-2004.
(77) BAND2016, SCM, Theoretical Chemistry, Vrije Universiteit, Amsterdam, The Netherlands, http://www.scm.com.
(78) Hehre, W. J.; Stewart, R. F.; Pople, J. A. Self-consistent molecular orbital methods. 1. Use of Gaussian expansions of Slater-type atomic orbitals. *J. Chem. Phys*. **1969**, *51*, 2657-2664.
(79) Ditchfield, R.; Hehre, W. J.; Pople, J. A. Self-consistent molecular orbital methods. 9. extended Gaussian-type basis for molecular-orbital studies of organic molecules. *J. Chem. Phys*. **1971**, *54*, 724-728.
(80) Hehre, W. J.; Ditchfield, R.; Pople, J. A. Self-consistent molecular orbital methods. 12. further extensions of Gaussian-type basis sets for use in molecular-orbital studies of organic-molecules. *J. Chem. Phys*. **1972**, *56*, 2257-2261.
(81) Hariharan, P. C.; Pople, J. A. Influence of polarization functions on molecular-orbital hydrogenation energies. *Theor. Chem. Acc*. **1973**, *28*, 213-222.
(82) Hariharan, P. C.; Pople, J. A. Accuracy of AH equilibrium geometries by single determinant molecular-orbital theory. *Mol. Phys*. **1974**, *27*, 209-214.
(83) Gordon, M. S. The isomers of silacyclopropane. *Chem. Phys. Lett*. **1980**, *76*, 163-168.
(84) Francl, M. M.; Pietro, W. J.; Hehre, W. J.; Binkley, J. S.; DeFrees, D. J.; Pople, J. A.; Gordon, M. S. Self-consistent molecular orbital methods. 23. a polarization-type basis set for 2nd-row elements. *J. Chem. Phys.* **1982**, *77*, 3654-3665.
(85) Binning Jr., R. C.; Curtiss, L. A. Compact contracted basis-sets for 3rd-row atoms – Ga-Kr. *J. Comp. Chem*. **1990**, *11*, 1206-1216.
(86) Blaudeau, J. P.; McGrath, M. P.; Curtiss, L. A.; Radom, L. Extension of Gaussian-2 (G2) theory to molecules containing third-row atoms K and Ca. *J. Chem. Phys.* **1997**, *107*, 5016-5021.

(87) Rassolov, V. A.; Pople, J. A.; Ratner, M. A.; Windus, T. L. 6-31G* basis set for atoms K through Zn. *J. Chem. Phys.* **1998**, *109*, 1223-1229.
(88) Rassolov, V. A.; Ratner, M. A.; Pople, J. A.; Redfern, P. C.; Curtiss, L. A. 6-31G* basis set for third-row atoms. *J. Comp. Chem.* **2001**, *22*, 976-84.
(89) McLean, A. D.; Chandler, G. S. Contracted Gaussian-basis sets for molecular calculations. 1. 2nd row atoms, Z=11-18. *J. Chem. Phys.* **1980**, *72*, 5639-5648.
(90) Raghavachari, K.; Binkley, J. S.; Seeger, R.; Pople, J. A. Self-consistent molecular orbital methods. 20. Basis set for correlated wave-functions. *J. Chem. Phys.* **1980**, *72*, 650-654.
(91) Blaudeau, J. P.; McGrath, M. P.; Curtiss, L. A.; Radom, L. Extension of Gaussian-2 (G2) theory to molecules containing third-row atoms K and Ca. *J. Chem. Phys.* **1997**, *107*, 5016-5021.
(92) Wachters, A. J. H. Gaussian basis set for molecular wavefunctions containing third-row atoms. *J. Chem. Phys.* **1970**, *52*, 1033-1036.
(93) Hay, P. J. Gaussian basis sets for molecular calculations – representation of 3D orbitals in transition-metal atoms. *J. Chem. Phys.* **1977**, *66*, 4377-4384.
(94) Raghavachari, K.; Trucks, G. W.; Highly correlated systems: Excitation energies of first row transition metals Sc-Cu. *J. Chem. Phys.* **1989**, *91*, 1062-1065.
(95) Binning Jr., R. C.; Curtiss, L. A. Compact contracted basis-sets for 3rd-row atoms - Ga-Kr" *J. Comp. Chem.* **1990**, *11*, 1206-1216.
(96) McGrath, M. P.; Radom, L. Extension of Gaussian-1 (G1) theory to bromine-containing molecules. *J. Chem. Phys.* **1991**, *94*, 511-516.
(97) Curtiss, L. A.; McGrath, M. P.; Blaudeau, J. P.; Davis, N. E.; Binning Jr., R. C.; Radom, L.; Extension of Gaussian-2 theory to molecules containing third-row atoms Ga-Kr. *J. Chem. Phys.* **1995**, *103*, 6104-6013.
(98) Barone, V.; Chong, D. P.; In *Recent Advances in Density Functional Methods, Part I, Ed.* World Scientific Publ. Co.: 1996.
(99) Clark, T. Chandrasekhar, J. Spitznagel, G. W.; Schleyer, P. V. R. Efficient diffuse function-augmented basis-sets for anion calculations. 3. The 3-21+G basis set for 1st-row elements, Li-F. *J. Comp. Chem.* **1983**, *4*, 294-301.
(100) Hohenberg, P.; Kohn, W. Inhomogeneous Electron Gas. *Phys. Rev.* **1964**, *136*, B864-B871.
(101) Kohn, W.; Sham, L. J. Self-consistent equations including exchange and correlation effects. *Phys. Rev.* **1965**, *140*, A1133-A1138.
(102) Hartree, D. R. In *The Calculation of Atomic Structure*. John Wiley & Sons:1957.
(103) Fock, V. Näherungsmethode zur Lösung des quantenmechanischen Mehrkörperproblems. *Z. Physik.* **1930**, *61*, 126-148.
(104) Dirac, P. A. M. Note on exchange phenomena in the Thomas-Fermi atom. *Proc. Cambridge Phil. Roy. Soc.* **1930**, *26 (3)*, 376–385.
(105) Bloch, F. Bemerkung zur elektronentheorie des ferromagnetismus und der electrische leitfähigkeit. *Z. Phys.* **1929**, *57*, 545-555.

(106) Ceperley, D. M.; Alder, B. J. Ground state of the electron gas by a stochastic method. *Phys. Rev. Lett*. **1980**, *45*, 566-569.
(107) Perdew, J. P.; Chevary, J. A.; Vosko, S. H.; Jackson, K. A.; Pederson, M. R.; Singh, D. J; Fiolhais, C. Atoms, molecules, solids, and surfaces: applications of the generalized gradient approximation for exchange and correlation. *Phys. Rev. B*. **1992**, *46*, 6671-6687.
(108) Becke, A. D. Density-functional exchange-energy approximation with correct asymptotic behavior. *Phys. Rev. A*. **1988**, *38*, 3098-3100.
(109) Langreth, D. C.; Mehl, M. J. "Beyond the local-density approximation in calculations of ground-state electronic properties". *Phys. Rev. B.* **1983**, *28*, 1809-1834.
(110) Becke, A. D. Density-functional exchange-energy approximation with correct asymptotic behavior. *Phys. Rev. A.* **1988**, *38*, 3098-3100.
(111) Reiher, M.; Salomon, M. O.; Hess, B. A. Reparameterization of hybrid functionals based on energy differences of states of different multiplicity. *Theor. Chem. Acc*. **2001**, *107*, 48-55.
(112) Perdew, J. P. Density-functional approximation for the correlation energy of the inhomogeneous electron gas. *Phys. Rev. B*. **1986**, *33*, 8822-8824.
(113) van Lenthe, E.; van der Avoird, A.; Wormer, P. E. S. Density functional calculations of molecular hyperfine interactions in the zero order regular approximation for relativistic effects. *J. Chem. Phys*. **1998**, *108*, 4783-4796.
(114) Schreckenbach, G.; Ziegler, T. The calculation of NMR shielding tensors using GIAO's and modern density functional theory. *J. Phys. Chem*. **1995**, *99*, 606-611.
(115) Schreckenbach, G.; Ziegler, T. The calculation of NMR shielding tensors based on density functional theory and the frozen-core approximation. *Int. J. Quantum Chem*. **1996**, *60*, 753-766.
(116) Schreckenbach, G.; Ziegler, T. Calculation of NMR shielding tensors based on density functional theory and a scalar relativistic Pauli-type Hamiltonian. The application to transition metal complexes. *Int. J. Quantum Chem*. **1997**, *61*, 899-918.
(117) Wolff, S. K.; Ziegler, T. Calculation of DFT-GIAO NMR shifts with inclusion of spin-orbit coupling. *J. Chem. Phys*. **1998**, *109*, 895-905.
(118) Wolff, S. K.; Ziegler, T.; van Lenthe, E.; Baerends, E. J. Density functional calculations of nuclear magnetic shieldings using the zeroth-order regular approximation (ZORA) for relativistic effects: ZORA nuclear magnetic resonance. *J. Chem. Phys*. **1999**, *110*, 7689-7698.
(119) Autschbach, J. Zheng, S. Relativistic computations of NMR parameters from first principles: Theory and applications. *Annu. Rep. NMR Spectrosc*. **2009**, *67*, 1-95.
(120) van Lenthe, E.; Snijders, J. G.; Baerends, E. J. The zero-order regular approximation for relativistic effects: The effect of spin-orbit coupling in closed shell molecules. *J. Chem. Phys*. **1996**, *105*, 6505-6516.
(121) Autschbach, J.; Patchkovskii, S.; Pritchard, B. Calculation of hyperfine tensors and paramagnetic NMR shifts using the relativistic zeroth-order regular approximation and density functional theory. *J. Chem. Theory Comput.* **2011**, *7*, 2175-2188.

(122) Moon, S.; Patchkovskii, S. First-principles calculations of paramagnetic NMR shifts. In *Calculation of NMR and EPR Parameters*. Wiley, Weinheim: 2004.

(123) Hrobárik, P.; Reviakine, R.; Arbuznikov, A. V.; Malkina, O. L.; Malkin, V. G.; Köhler, F. H.; Kaupp, M. Density functional calculations of NMR shielding tensors for paramagnetic systems with arbitrary spin multiplicity: Validation on 3d metallocenes. *J. Chem. Phys*. **2007**, *126*, 024107.

(124) Kadantsev, E.S.; Ziegler, T. Implementation of a density functional theory-based method for the calculation of the hyperfine A-tensor in periodic systems with the use of numerical and slater type atomic orbitals: application to paramagnetic defects. *J. Phys. Chem. A*. **2008**, *112*, 4521–4526.

(125) Crichton, R. R.; Charloteaux-Wauters, M. Iron transport and storage. *Eur. J. Biochem*. **1987**, *164*, 485–506.

(126) Abdallah, F. B.; Chahine, J. M. Transferrins, the mechanism of iron release by ovotransferrin. *Eur. J. Biochem.* **1999**, *263*, 912–920.

(127) Mason, A. B., & Macgillivray, R. T. A. Transferrins. In *D. Templeton (Ed.), Molecular and cellular iron transport*. New York: Marcel Dekker, INC.:2002.

(128) Mason, A. B., & Macgillivray, R. T. A. (2002). Transferrins. In *D. Templeton (Ed.)*. Molecular and cellular iron transport. New York: Marcel Dekker, INC.

(129) Schade, A. L.; Caroline, L. Raw hen egg white and the role of iron in growth inhibition of Shigella dysenteriae, Staphylococcus aureus, Escherichia coli and Saccharomyces cerevisiae. *Science*. **1944**, *100*, 14–15.

(130) Wu, J.; Acero-Lopez, A. Ovotransferrin: Structure, bioactivities, and preparation. *Food. Res. Int.* **2012**, *46*, 480-487.

(131) Bertini, I.; Briganti, F.; Koenig, S. H.; Luchinatt, C. Magnetic relaxation of solvent protons by Cu^{2+} and VO^{2+} substituted transferrin: theoretical analysis and biochemical implications. *Biochem*. **1985**, *24*, 6287-6290.

(132) Li, Y.; Liu, B.; Ge, Z.; Yang, B. Spectroscopic analysis of the interaction between gallium(III) and apoovotransferrin. J. *Photochem. Photobiol. B: Biology*. **2008**, *91*, 137-142.

(133) Quarles Jr., C. D.; Brumaghim, J. L.; Marcus, R. K. Instrumental comparison of the determination of Cr^{3+} uptake by human transferrin. *Metallomics*. **2010**, *2*, 792–799.

(134) Saponja, J. A.; Vogel, H. J. Quadrupolar central transition (QCT) and ^{13}C NMR competition studies of metal ion binding to ovotransferrin. *Can. J. Chem*. **2011**, *89*, 779-788.

(135) Willcot, M. R. MestRe Nova. *J. Am. Chem. Soc.* **2009**, *131*, 13180–13180.

(136) Manzer, L. E. Tetragtdrfuran Complexes of Selected Early Transition Metals. Inorg. *Inorg. Synth*. **1982**, *21*, 135.

(137) Clark, R. J. H.; Nyholm, R. S.; Scaife, D. E. Tetrahedral and octahedral complexes of vanadium(III). *J. Chem. Soc. A*. **1966**, *0*, 1296-1302.

(138) Zhu, J.; Wu, G. Quadrupole central transition ^{17}O NMR spectroscopy of biological macromolecules in aqueous solution. *J. Am. Chem. Soc*. **2011**, *133*, 920–932.

(139) Bertini, I.; Canti, G.; Luchinat, C. Preparation and characterization of the vanadium-(III) derivative of transferrin. *Inorg. Chimica. Acta*. **1982**, *67*, 21-23.

(140) Cotton, F.A.; Duraj, S.A.; Powell, G.L.; Roth, W.J. Comparative structural studies of the first row early transition metal(III) chloride tetrahydrofuran solvates. *Inorg. Chimica. Acta*. **1986**, *113*, 81-85.

(141) Fedorova, E.V.; Rybakov, V.B.; Senyavin, V.M.; Anisimov, A.V.; Aslanov, L.A. Synthesis and structure of oxovanadium(IV) complexes[$VO(acac)_2$] and [VO(Sal : L-alanine)(H_2O)]. *Crystallogr. Rep*. **2005**, *50*, 224–229.

(142) Wickramasinghe, N.P.; Shaibat, M.A.; Jones, C.R.; Casabianca, L.B.; Dios, A.C.; Harwood, J.S.; Ishii, Y. Progress in ^{13}C and ^{1}H solid-state nuclear magnetic resonance for paramagnetic systems under very fast magic angle spinning. *J. Chem. Phys.* **2008**, *128*, 052210.

(143) Doddrell, D.M.; Gregson, A.K. Carbon-13 NMR studies of some paramagnetic transition-metal acetylacetonates some linewidth considerations. *Chem. Phys. Lett.* **1974**, *29*, 512-515.

(144) Duckworth, M. W.; Fowles, G. W. A.; Hoodless, R. A. Reaction of alkyl cyanides with chlorides and bromides of tervalent titanium and vanadium, and with vanadium(IV) chloride. *J. Chem. Soc*. **1963**, *0*, 5665-5673.

(145) Clark, R. J. H. Metal-halogen stretching frequencies in inorganic complexes. *Spectrochim. Acta*. **1965**, *21*, 955-963.

(146) O'Brien, J.F. fac-mer equilibrium in solutions of VCl_3 in acetonitrile. *Inorg. Chem*. **1987**, *26*, 3266-3273.

(147) Wachters, A. J. H. Gaussian basis set for molecular wavefunctions containing third - row atoms. *J. Chem. Phys.* **1970**, *52*, 1033-1036.

(148) Weigend, F. Accurate Coulomb-fitting basis sets for H to Rn. *Phys. Chem. Chem. Phys*. **2006**, *8*, 1057-1065.

(149) Harris, W.R. Binding of vanadate to human serum transferrin. *J. Inorg. Biochem*. **1984**, *22*, 201-218.

(150) Zhang, Y.; Sun, H.; Oldfield, E. Solid-state NMR Fermi contact and dipolar shifts in organometallic complexes and metalloporphyrins. *J. Am. Chem. Soc.* **2005**, *127*, 3652-3653.

(151) Ishii, Y.; Wickramasinghe, N. P.; Chimon, S. A new approach in 1D and 2D ^{13}C high-resolution solid-state NMR spectroscopy of paramagnetic organometallic complexes by very fast magic-angle spinning. *J. Am. Chem. SOC.* **2003**, *125*, 3438-3439.

(152) Liu, K.; Ryan, D.; Nakanishi, K.; McDermott, A. Solid state NMR studies of paramagnetic coordination complexes: a comparison of protons and deuterons in detection and decoupling. *J. Am. Chem. SOC*. **1995**, *117*, 6897-6906.

(153) Kadantsev, E. S.; Klooster, R.; de Boeij, P. L.; Ziegler, T. The formulation and implementation of analytic energy gradients for periodic density functional calculations with STO/NAO Bloch basis set. *Mol.Phys*. **2007**, *105*, 2583-2596.

(154) Wu, G. Solid-state ^{17}O NMR studies of organic and biological molecules. *Prog. Nucl. Magn. Reson. Spectrosc.***2008**, *52*, 118-169.

(155) Zhu, J.; Ye, E.; Terskikh, V.; Wu, G. Solid-state ^{17}O NMR spectroscopy of large protein-ligand complexes. *Angew. Chem. Int. Ed.* **2010**, *49*, 8399-8402.

(156) Wu, G. Solid-state ^{17}O NMR studies of organic and biological molecules: recent advances and future directions. *Solid. State. Nucl. Magn. Reson.* **2016**, *73*, 1-14.
(157) Engberg, A. An X-Ray Refinement of the Crystal Structure of Copper(II) Chloride Dihydrate. *Acta Chem. Scand*. **1970**, *24*, 3510-3526.
(158) Buluggiu, E.; Dascola, G.; Giori, D. C.; Vera, A. ESR studies of covalent copper complexes with a rhombic arrangement. *J. Chem. Phys.* **1971**, *54*, 2191-2196.
(159) Rundle, R. E. Antiferromagnetic ordering and electronic structure of $CuCl_2 \cdot 2H_2O$ as determined from nuclear magnetic resonance. *J. Am. Chem. Soc*. **1957**, *79*, 3372-3374.
(160) Poulis, N. J.; Hardeman, G. E. G. Nuclear magnetic resonance in an anti ferromagnetic single crystal. Part I. *Physica.* **1952,** *18*, 201-220.
(161) Walder, B. J.; Dey, K. K.; Davis, M. V.; Baltisberger, J. H.; Grandinetti, P. J. Two-dimensional NMR measurement and point dipole model prediction of paramagnetic shift tensors in solids. *J. Chem. Phys*. **2015**, *142*, 014201.
(162) O'Reilly, D. E.; Tsang, T. Oxygen-17 nuclear magnetic resonance in paramagnetic MnO and CoO. *J. Chem. Phys.* **1964**, *40*, 734-736.

Appendix I Calculated Anisotropic A-tensor Components of vanadium compounds

Table A-1. ADF results of anisotropic A-tensor components of $V(acac)_3$ in MHz.[a]

	DZ			TZP			TZ2P			QZ4P			jcpl		
Atoms	A_{11}	A_{22}	A_{33}	A_{11}	A_{22}	A_{33}	A_{11}	A_{22}	A_{33}	A_{11}	A_{22}	A_{33}	A_{11}	A_{22}	A_{33}
V-^{17}**O**	2.98	-0.62	-2.35	2.87	-0.63	-2.24	2.84	-0.61	-2.23	2.85	-0.61	-2.24	2.82	-0.62	-2.20
^{13}**C**=O	-1.73	0.21	1.52	-1.77	0.19	1.58	-1.81	0.19	1.63	-1.83	0.18	1.65	-1.79	0.20	1.60
C-^{13}**C**-C	-0.91	-0.30	1.21	-0.87	-0.30	1.18	-0.86	-0.31	1.17	-0.87	-0.31	1.17	-0.85	-0.31	1.17
^{13}**C**-H_3	-0.23	-0.15	0.38	-0.23	-0.14	0.37	-0.23	-0.14	0.37	-0.23	-0.13	0.36	-0.23	-0.14	0.37
C-^{1}**H**	-0.92	-0.77	1.69	-0.93	-0.78	1.71	-0.93	-0.78	1.72	-0.93	-0.78	1.72	-0.93	-0.78	1.72
C-^{1}**H**$_3$	-0.78	-0.73	1.51	-0.72	-0.68	1.45	-0.80	-0.73	1.48	-0.78	-0.72	1.49	-0.78	-0.72	1.49

Note: [a]$V(acac)_3$ was used as a standard systems to test the basis sets. The rest systems only used one basis set combination.

Table A-2. ADF results of anisotropic A-tensor components of $VCl_3(THF)_3$ using jcpl basis set.

Atoms	A_{11}	A_{22}	A_{33}
V-^{17}**O**(eq)	1.29	0.39	-1.68
V-^{17}**O**(ax)	0.62	0.11	-0.73
^{13}**C**-O(eq)	-0.50	-0.43	0.93
^{13}**C**-O(ax)	-0.76	-0.64	1.40
^{13}**C**-C(eq)	-0.46	-0.41	0.87
^{13}**C**-C(ax)	-0.21	-0.21	0.42
O-C-^{1}**H**(eq)	-1.42	-1.37	2.78
O-C-^{1}**H**(ax)	-2.18	-2.09	4.27
C-C-^{1}**H**$_3$(eq)	-1.33	-1.31	2.64
C-C-^{1}**H**$_3$(ax)	-0.61	-0.60	1.21

Table A-3. ADF results of anisotropic A-tensor components of $VCl_3(MeCN)_3$ using jcpl basis set.

	Mer structure			Fac structure		
Atoms	A_{11}	A_{22}	A_{33}	A_{11}	A_{22}	A_{33}
^{13}**C**-N(eq)	-1.58	0.42	1.16	-0.81	-0.13	0.94
^{13}**C**-N(18)(ax)	-1.19	-0.75	1.94			
^{13}**C**-C(eq)	-0.17	-0.15	0.33	-0.19	-0.14	0.33
^{13}**C**-C(19)(ax)	-0.19	-0.14	0.32			
C-^{1}**H**(eq)	-0.65	-0.61	1.27	-0.58	-0.55	1.13
C-^{1}**H**(20)(ax)	-0.58	-0.54	1.13			

Table A-4. ADF results of anisotropic A-tensor components of $VO(acac)_2$ using jcpl basis set.

Atoms	A_{11}	A_{22}	A_{33}
V=**O**	3.03	1.81	-4.84
V-**O**	2.69	0.94	-3.63
C=O	-1.11	-1.04	2.15
C-**C**-C	-0.70	-0.55	1.25
C-H3	-0.23	-0.20	0.43
C-**H**	-1.00	-0.93	1.93
C-$\mathbf{H}_3$	-0.85	-0.79	1.65

Appendix II Chemical shifts vs. 1/T plots of variable temperature solution-state NMR experiments

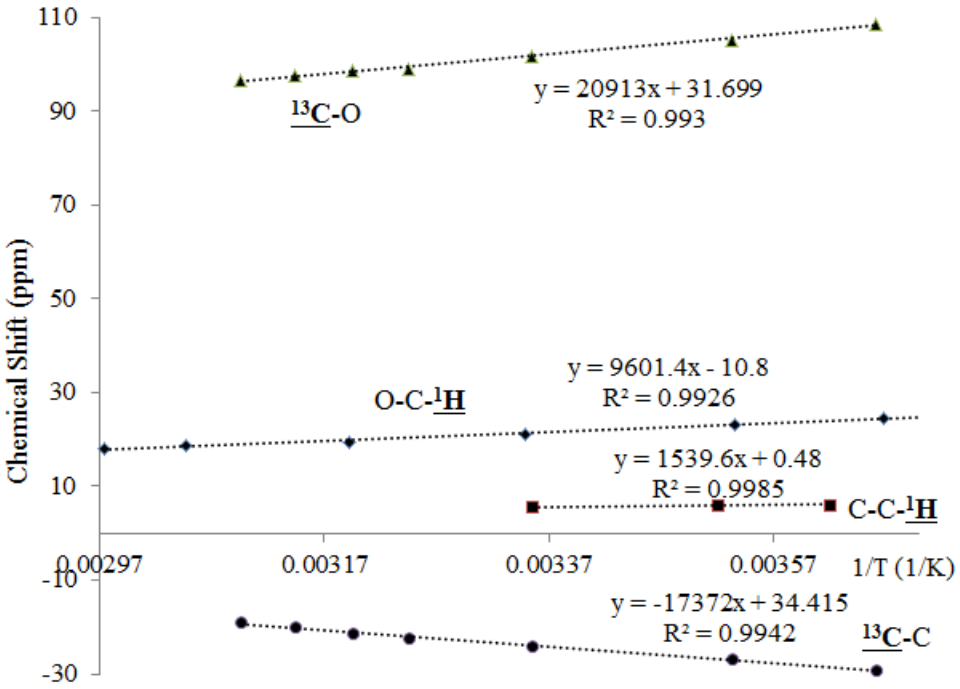

Figure A-1. $\delta(^{1}H)$ and $\delta(^{13}C)$ vs. 1/T plot of $VCl_3(THF)_3$.

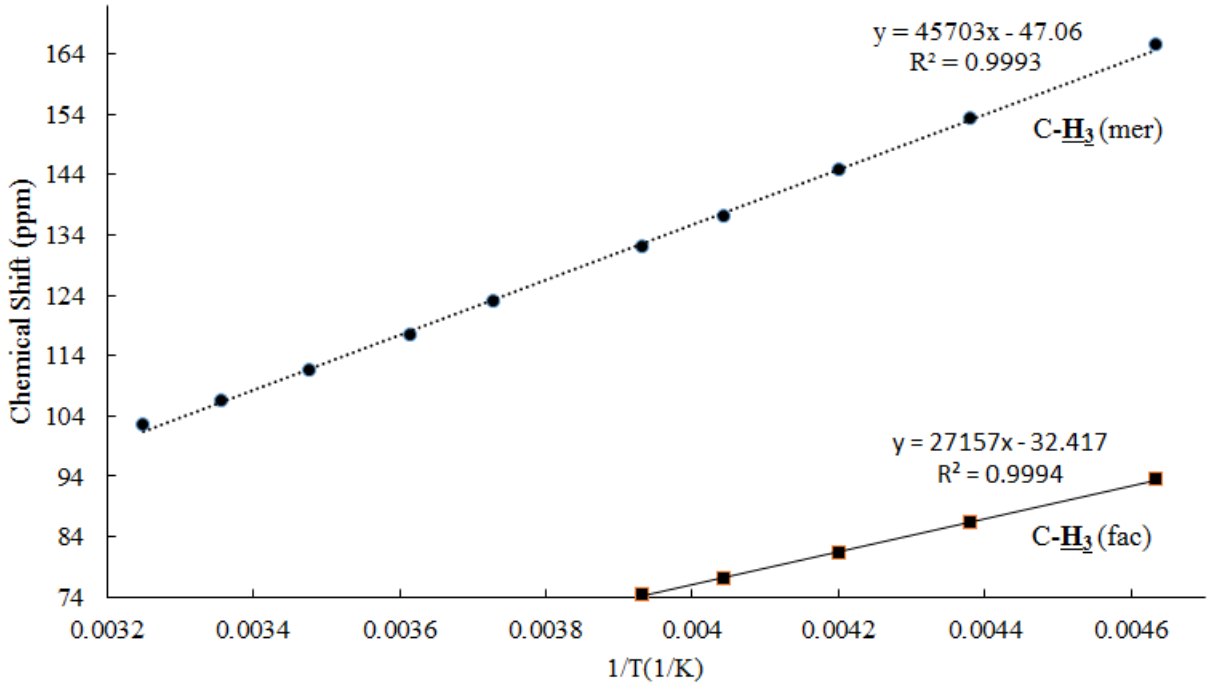

Figure A-2. $\delta(^{1}H)$ vs. 1/T plot of $VCl_3(MeCN)_3$.

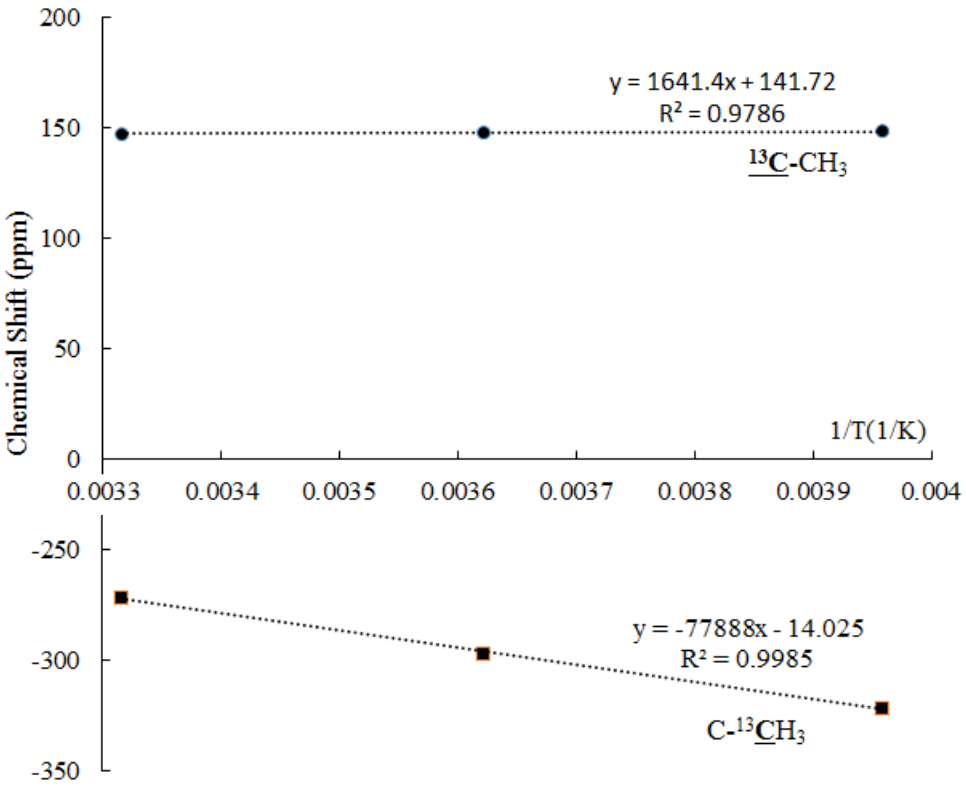

Figure A-3. $\delta(^{13}C)$ vs. 1/T plot of $VCl_3(MeCN)_3$.

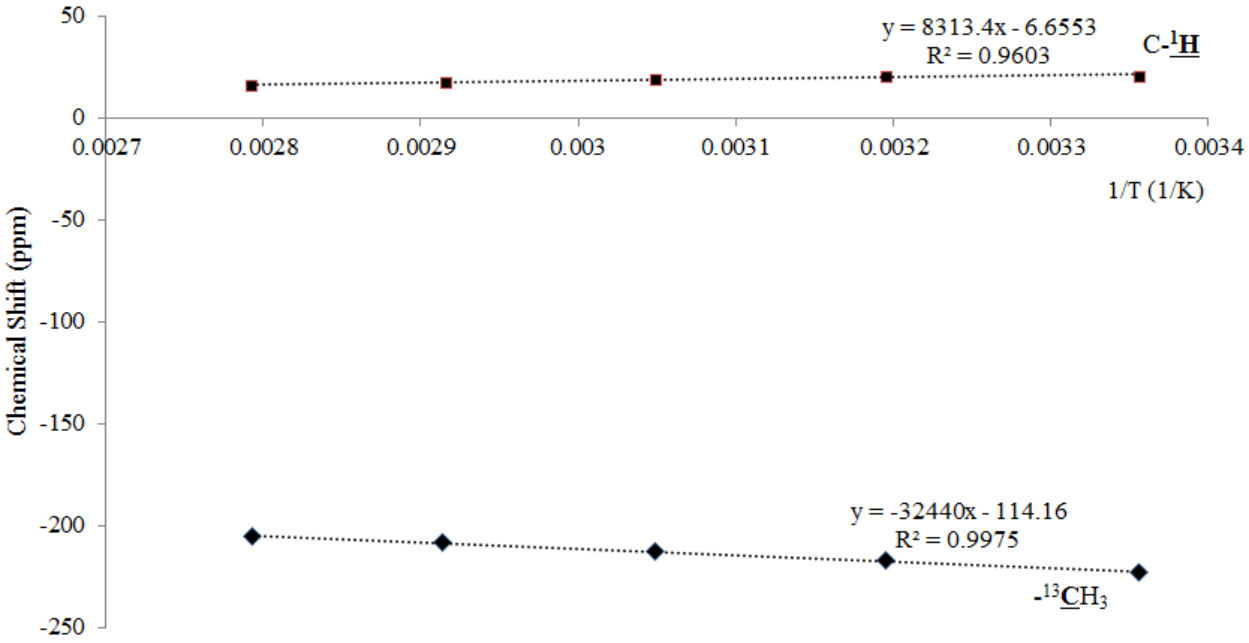

Figure A-4. $\delta(^{1}H)$ and $\delta(^{13}C)$ vs. 1/T plot of $VO(acac)_2$.

Appendix III Calculation results of A_{iso} of Cu(DL-Alanine)$_2$·H_2O

Table A-5. Calculation results of A_{iso} of Cu(DL-Alanine)$_2$·H_2O.

Structure	Method	Atoms[a]	VWN	BP86x	PBEx	mPBE	BLYP	revPBE	Exp.
Original	Gradient	**Cu**	-271.00[b]	-326.06	-323.81	-332.38	-296.76	-347.97	251.80
		Cu-**O**	-32.32	-33.67	-34.61	-34.61	-35.62	-33.95	
		C=**O**	-0.26	-0.49	-0.74	-0.74	-0.85	-0.60	-1.80
		H_2**O**	3.12	3.49	3.55	3.55	3.67	3.50	1.50
		C=O	-7.77	-7.35	-7.22	-7.22	-7.30	-7.28	-3.76
		C-**C**-H	-5.06	-5.21	-5.09	-5.11	-5.06	-5.19	-3.27
		C-H_3	-0.09	0.00	0.00	0.01	0.10	0.01	1.89
		N-**H**	-14.16	-15.62	-15.40	-15.51	-15.51	-15.78	-6.70
		N-**H**	-13.19	-14.70	-14.51	-14.62	-14.59	-14.88	-5.70
		C-**H**	-7.39	-7.40	-7.44	-7.45	-7.44	-7.46	0.32
		C-**H**$_3$	-4.09	-4.44	-4.48	-4.53	-4.37	-4.61	1.18
		H$_2$O	-8.09	-8.35	-8.35	-8.37	-8.34	-8.41	0.90
	Density	**Cu**	269.24	187.99	185.40	170.99	250.69	145.75	251.80
		Cu-**O**	-27.72	-29.98	-32.22	-32.10	-32.28	-30.71	
		C=**O**	-0.26	-0.34	-0.83	-0.81	-0.77	-0.54	-1.80
		H_2**O**	1.97	2.32	2.41	2.41	2.53	2.34	1.50
		C=O	-5.52	-5.02	-4.87	-4.87	-4.97	-4.93	-3.76
		C-**C**-H	-3.37	-3.47	-3.33	-3.36	-3.30	-3.43	-3.27
		C-H_3	1.47	1.60	1.62	1.63	1.71	1.63	1.89
		N-**H**	-4.47	-5.64	-5.38	-5.47	-5.53	-5.72	-6.70
		N-**H**	-3.97	-5.23	-4.99	-5.08	-5.11	-5.32	-5.70
		C-**H**	-0.19	0.00	-0.01	0.01	-0.02	0.02	0.32
		C-**H**$_3$	2.31	2.13	2.11	2.08	2.20	2.02	1.18

		H$_2$O	-0.09	-0.12	-0.09	-0.09	-0.10	-0.11	0.90
LDA VWN optimized	Gradient	**Cu**	-134.63	-197.71	-245.24	-249.45	-223.13	-258.39	251.80
		Cu-**O**	-40.04	-40.58	-41.85	-41.76	-42.79	-40.97	
		C=**O**	-0.41	-0.57	-0.79	-0.78	-0.83	-0.67	-1.80
		H$_2$**O**	1.63	2.08	2.12	2.15	2.19	2.16	1.50
		C=O	-7.61	-7.20	-7.02	-7.02	-7.12	-7.06	-3.76
		C-**C**-H	-5.45	-5.56	-5.38	-5.40	-5.36	-5.48	-3.27
		C-H$_3$	0.95	0.93	0.96	0.97	1.03	0.96	1.89
		N-**H**	-15.00	-16.25	-16.02	-16.12	-16.28	-16.39	-6.70
		N-**H**	-13.91	-15.07	-14.85	-14.95	-15.06	-15.20	-5.70
		C-**H**	-8.16	-8.15	-8.17	-8.18	-8.16	-8.18	0.32
		C-**H**$_3$	-3.92	-4.28	-4.35	-4.39	-4.22	-4.48	1.18
		H$_2$O	-7.50	-7.82	-7.77	-7.80	-7.77	-7.84	0.90
	Density	**Cu**	461.49	369.31	140.59	141.00	209.47	133.12	251.80
		Cu-**O**	-35.88	-37.25	-40.39	-40.19	-40.37	-38.70	
		C=**O**	-0.38	-0.73	-1.16	-1.14	-1.05	-0.93	-1.80
		H$_2$**O**	0.70	1.06	1.09	1.11	1.18	1.13	1.50
		C=O	-5.21	-4.72	-4.52	-4.52	-4.63	-4.56	-3.76
		C-**C**-H	-3.59	-3.65	-3.46	-3.48	-3.45	-3.56	-3.27
		C-H$_3$	2.61	2.62	2.66	2.67	2.72	2.66	1.89
		N-**H**	-4.94	-5.90	-5.64	-5.72	-5.95	-5.96	-6.70
		N-**H**	-3.61	-4.47	-4.26	-4.34	-4.51	-4.56	-5.70
		C-**H**	-0.33	-0.11	-0.11	-0.10	-0.12	-0.08	0.32
		C-**H**$_3$	2.84	2.66	2.60	2.57	2.70	2.50	1.18
		H$_2$O	-0.18	-0.29	-0.24	-0.25	-0.27	-0.27	0.90
		Cu	-265.07	-311.69	-306.67	-310.72	-285.54	-319.63	251.80
		Cu-**O**	-34.12	-34.93	-35.86	-35.80	-36.72	-35.09	

GGA BP86 optimized	Gradient	C=**O**	-0.21	-0.39	-0.60	-0.59	-0.64	-0.49	-1.80
		H_2**O**	2.40	2.86	2.87	2.89	2.96	2.89	1.50
		C=O	-7.48	-7.06	-6.93	-6.94	-7.04	-6.99	-3.76
		C-**C**-H	-5.30	-5.37	-5.24	-5.26	-5.23	-5.34	-3.27
		C-H_3	0.75	0.77	0.76	0.76	0.84	0.76	1.89
		N-**H**	-14.34	-15.49	-15.28	-15.39	-15.53	-15.64	-6.70
		N-**H**	-13.32	-14.40	-14.23	-14.34	-14.43	-14.57	-5.70
		C-**H**	-7.76	-7.75	-7.80	-7.81	-7.79	-7.82	0.32
		C-**H**$_3$	-3.86	-4.23	-4.29	-4.34	-4.16	-4.43	1.18
		H$_2$O	-7.39	-7.67	-7.70	-7.73	-7.70	-7.77	0.90
	Density	**Cu**	4.62	-2.14	31.35	30.88	101.80	19.70	251.80
		Cu-**O**	-30.05	-31.85	-34.07	-33.91	-33.98	-32.52	
		C=**O**	-0.13	-0.50	-0.91	-0.89	-0.81	-0.69	-1.80
		H_2**O**	1.45	1.85	1.83	1.85	1.94	1.85	1.50
		C=O	-5.19	-4.70	-4.56	-4.56	-4.67	-4.60	-3.76
		C-**C**-H	-3.53	-3.56	-3.41	-3.43	-3.41	-3.50	-3.27
		C-H_3	2.36	2.41	2.42	2.43	2.49	2.42	1.89
		N-**H**	-4.68	-5.55	-5.29	-5.37	-5.58	-5.59	-6.70
		N-**H**	-3.38	-4.18	-3.95	-4.03	-4.19	-4.24	-5.70
		C-**H**	-0.26	-0.05	-0.06	-0.05	-0.06	-0.03	0.32
		C-**H**$_3$	2.69	2.50	2.47	2.43	2.57	2.37	1.18
		H$_2$O	-0.22	-0.31	-0.29	-0.30	-0.33	-0.33	0.90

[a] Results are averaged from all equivalent positions. [b] All values are reported in MHz.

Appendix IV Calculation Results of Anisotropic A-tensor components of $Cu(DL\text{-}Alanine)_2 \cdot H_2O$

Table A-6. Calculation Results of Anisotropic A-tensor components of $Cu(DL\text{-}Alanine)_2 \cdot H_2O$

Structure	Method	Atoms[a]	Tensor Comp.	VWN	PW86x	PBEx	mPBE	BLYP	revPBE	Exp
Original	Gradient	**Cu**	T_{11}	-327.74	-337.01	-337.48	-337.68	-340.41	-337.86	
			T_{22}	100.63	102.02	102.17	102.11	103.49	101.96	
			T_{33}	227.10	234.99	235.31	235.57	236.91	235.90	
		Cu-**O**	T_{11}	18.01	17.81	17.59	17.56	17.91	17.54	
			T_{22}	16.77	16.74	16.60	16.56	16.88	16.50	
			T_{33}	-34.78	-34.56	-34.20	-34.12	-34.78	-34.04	
		C=**O**	T_{11}	4.91	4.55	4.54	4.52	4.52	4.49	2.39
			T_{22}	3.35	3.14	3.13	3.11	3.08	3.09	0.42
			T_{33}	-8.26	-7.69	-7.67	-7.63	-7.60	-7.58	-2.81
		H_2**O**	T_{11}	0.78	0.80	0.81	0.81	0.82	0.81	
			T_{22}	-0.30	-0.29	-0.30	-0.30	-0.30	-0.29	
			T_{33}	-0.48	-0.51	-0.51	-0.51	-0.52	-0.52	
		C=O	T_{11}	-3.15	-3.07	-3.06	-3.06	-3.06	-3.06	-3.3
			T_{22}	0.33	0.26	0.26	0.26	0.25	0.25	1.65
			T_{33}	2.81	2.81	2.80	2.80	2.81	2.81	1.65
		C-**C**-H	T_{11}	-0.92	-0.95	-0.97	-0.97	-0.97	-0.97	-1.6
			T_{22}	-0.30	-0.29	-0.28	-0.28	-0.27	-0.29	0.8
			T_{33}	1.22	1.24	1.25	1.25	1.25	1.26	0.8
		C-H_3	T_{11}	-1.17	-1.16	-1.16	-1.16	-1.16	-1.16	-0.27
			T_{22}	0.04	0.07	0.08	0.08	0.08	0.08	-0.27
			T_{33}	1.13	1.10	1.09	1.08	1.08	1.08	0.55
		N-**H**	T_{11}	-9.83	-9.85	-9.79	-9.80	-9.83	-9.83	-7.63

			T_{22}	-2.64	-2.60	-2.62	-2.62	-2.68	-2.63	-2.43
			T_{33}	12.47	12.45	12.40	12.42	12.51	12.46	10.05
			T_{11}	-11.50	-11.51	-11.45	-11.47	-11.49	-11.50	-6.76
		N-**H**	T_{22}	0.34	0.31	0.28	0.27	0.26	0.27	-2.72
			T_{33}	11.16	11.20	11.17	11.19	11.23	11.23	9.48
			T_{11}	-4.53	3.39	-4.63	-4.64	-4.62	-4.65	-3.9
		C-**H**	T_{22}	-0.53	4.75	-0.56	-0.56	-0.57	-0.56	1.1
			T_{33}	5.06	6.66	5.20	5.20	5.19	5.21	2.8
			T_{11}	-4.18	-4.26	-4.27	-4.28	-4.26	-4.29	-2.49
		C-**H**$_3$	T_{22}	0.94	0.97	0.97	0.97	0.96	0.98	0
			T_{33}	3.24	3.30	3.30	3.31	3.30	3.31	2.49
			T_{11}	-4.90	-5.05	-5.07	-5.07	-5.05	-5.10	
		H$_2$O	T_{22}	0.67	0.71	0.73	0.73	0.74	0.73	
			T_{33}	4.23	4.33	4.34	4.34	4.31	4.37	
	Density		T_{11}	-319.81	-328.87	-329.35	-329.57	-332.30	-329.78	
		Cu	T_{22}	149.71	152.93	153.09	153.03	154.77	152.87	
			T_{33}	170.10	175.94	176.26	176.54	177.52	176.91	
			T_{11}	18.02	17.83	17.61	17.57	17.92	17.55	
		Cu-**O**	T_{22}	16.41	16.38	16.24	16.19	16.52	16.14	
			T_{33}	-34.44	-34.21	-33.85	-33.76	-34.44	-33.69	
			T_{11}	4.59	4.21	4.20	4.18	4.19	4.15	2.39
		C=**O**	T_{22}	3.49	3.29	3.28	3.26	3.22	3.24	0.42
			T_{33}	-8.08	-7.50	-7.48	-7.44	-7.41	-7.39	-2.81
			T_{11}	0.24	0.25	0.24	0.24	0.22	0.25	
		H_2**O**	T_{22}	0.07	0.07	0.07	0.07	0.08	0.07	
			T_{33}	-0.31	-0.31	-0.31	-0.31	-0.31	-0.31	
		C=O	T_{11}	-2.54	-2.43	-2.41	-2.41	-2.42	-2.41	-3.3

			T_{22}	0.18	0.11	0.11	0.11	0.10	0.11	1.65
			T_{33}	2.36	2.32	2.30	2.30	2.31	2.30	1.65
			T_{11}	-0.63	-0.64	-0.63	-0.63	-0.64	-0.63	-1.6
		C-**C**-H	T_{22}	-0.16	-0.15	-0.15	-0.15	-0.15	-0.15	0.8
			T_{33}	0.79	0.78	0.79	0.78	0.79	0.78	0.8
			T_{11}	-0.70	-0.65	-0.65	-0.64	-0.64	-0.63	-0.27
		C-H_3	T_{22}	-0.40	-0.36	-0.35	-0.34	-0.34	-0.34	-0.27
			T_{33}	1.09	1.01	0.99	0.98	0.99	0.97	0.55
			T_{11}	-9.87	-9.78	-9.71	-9.72	-9.76	-9.74	-7.63
		N-**H**	T_{22}	-0.10	0.20	0.22	0.23	0.06	0.23	-2.43
			T_{33}	9.97	9.59	9.49	9.49	9.70	9.51	10.05
			T_{11}	-9.78	-9.69	-9.61	-9.62	-9.66	-9.64	-6.76
		N-**H**	T_{22}	-0.65	-0.39	-0.37	-0.37	-0.52	-0.37	-2.72
			T_{33}	10.43	10.07	9.98	9.98	10.19	10.01	9.48
			T_{11}	-1.83	-1.83	-1.83	-1.83	-1.84	-1.83	-3.9
		C-**H**	T_{22}	-0.37	-0.37	-0.37	-0.37	-0.37	-0.37	1.1
			T_{33}	2.19	2.20	2.20	2.20	2.21	2.20	2.8
			T_{11}	-1.11	-1.10	-1.09	-1.09	-1.10	-1.09	-2.49
		C-**H**$_3$	T_{22}	-0.19	-0.20	-0.20	-0.20	-0.21	-0.20	0
			T_{33}	1.30	1.30	1.30	1.30	1.30	1.30	2.49
			T_{11}	-1.77	-1.78	-1.78	-1.79	-1.78	-1.79	
		H$_2$O	T_{22}	0.05	0.05	0.05	0.05	0.05	0.05	
			T_{33}	1.72	1.74	1.74	1.74	1.73	1.74	
			T_{11}	-332.25	-342.76	-348.41	-348.82	-351.25	-349.36	
		Cu	T_{22}	97.67	99.11	100.64	100.61	101.94	100.53	
			T_{33}	234.58	243.65	247.77	248.20	249.31	248.83	
		Cu-**O**	T_{11}	17.58	17.37	17.02	16.97	17.37	16.93	

LDA VWN	Gradient		T_{22}	16.31	16.31	16.03	15.98	16.33	15.90	
			T_{33}	-33.89	-33.68	-33.04	-32.95	-33.69	-32.83	
		C=**O**	T_{11}	4.22	3.95	3.89	3.87	3.89	3.84	2.39
			T_{22}	2.68	2.57	2.50	2.48	2.47	2.46	0.42
			T_{33}	-6.91	-6.52	-6.38	-6.35	-6.36	-6.29	-2.81
		H_2**O**	T_{11}	0.75	0.79	0.80	0.80	0.80	0.80	
			T_{22}	-0.35	-0.35	-0.34	-0.33	-0.33	-0.33	
			T_{33}	-0.39	-0.44	-0.46	-0.47	-0.46	-0.48	
		C=O	T_{11}	-3.02	-2.97	-2.94	-2.94	-2.95	-2.95	-3.3
			T_{22}	0.27	0.21	0.22	0.22	0.21	0.22	1.65
			T_{33}	2.75	2.76	2.72	2.72	2.74	2.72	1.65
		C-**C**-H	T_{11}	-0.99	-1.03	-1.04	-1.04	-1.04	-1.04	-1.6
			T_{22}	-0.32	-0.33	-0.31	-0.31	-0.31	-0.32	0.8
			T_{33}	1.31	1.35	1.35	1.35	1.34	1.35	0.8
		C-H_3	T_{11}	-1.20	-1.18	-1.17	-1.17	-1.16	-1.17	-0.27
			T_{22}	0.02	0.04	0.06	0.06	0.05	0.06	-0.27
			T_{33}	1.18	1.15	1.12	1.11	1.11	1.11	0.55
		N-**H**	T_{11}	-8.35	-8.39	-8.30	-8.31	-8.32	-8.34	-7.63
			T_{22}	-2.75	-2.77	-2.88	-2.88	-2.92	-2.89	-2.43
			T_{33}	11.10	11.16	11.18	11.19	11.24	11.23	10.05
		N-**H**	T_{11}	-9.50	-9.49	-9.39	-9.41	-9.41	-9.44	-6.76
			T_{22}	-0.97	-1.00	-1.01	-1.01	-1.06	-1.02	-2.72
			T_{33}	10.47	10.50	10.40	10.42	10.47	10.46	9.48
		C-**H**	T_{11}	-4.69	-4.80	-4.80	-4.81	-4.79	-4.82	-3.9
			T_{22}	-0.77	-0.80	-0.82	-0.82	-0.82	-0.82	1.1
			T_{33}	5.47	5.60	5.62	5.63	5.61	5.64	2.8
		C-**H**$_3$	T_{11}	-4.31	-4.40	-4.40	-4.41	-4.39	-4.42	-2.49
			T_{22}	0.86	0.89	0.89	0.89	0.88	0.89	0

			T_{33}	3.45	3.51	3.52	3.52	3.51	3.53	2.49
			T_{11}	-5.41	-5.54	-5.54	-5.55	-5.51	-5.57	
		H$_2$O	T_{22}	-1.10	-1.10	-1.10	-1.10	-1.09	-1.10	
			T_{33}	6.51	6.64	6.64	6.65	6.60	6.67	
			T_{11}	-317.20	-326.93	-333.23	-333.60	-336.21	-334.08	
		Cu	T_{22}	131.68	133.23	133.35	133.21	135.14	132.92	
			T_{33}	185.52	193.70	199.88	200.39	201.08	201.16	
			T_{11}	17.58	17.38	17.02	16.97	17.37	16.93	
		Cu-**O**	T_{22}	15.95	15.94	15.65	15.60	15.96	15.53	
			T_{33}	-33.53	-33.31	-32.67	-32.58	-33.33	-32.46	
			T_{11}	3.93	3.65	3.58	3.56	3.59	3.52	2.39
		C=**O**	T_{22}	2.77	2.66	2.59	2.57	2.56	2.55	0.42
			T_{33}	-6.71	-6.31	-6.17	-6.13	-6.15	-6.07	-2.81
			T_{11}	0.43	0.39	0.37	0.37	0.36	0.37	
		H$_2$**O**	T_{22}	0.17	0.13	0.12	0.11	0.11	0.11	
	Density		T_{33}	-0.60	-0.51	-0.49	-0.48	-0.47	-0.48	
			T_{11}	-2.50	-2.41	-2.38	-2.38	-2.39	-2.38	-3.3
		C=O	T_{22}	0.22	0.16	0.16	0.16	0.15	0.16	1.65
			T_{33}	2.29	2.25	2.22	2.22	2.24	2.22	1.65
			T_{11}	-0.68	-0.69	-0.68	-0.68	-0.69	-0.68	-1.6
		C-**C**-H	T_{22}	-0.16	-0.16	-0.16	-0.16	-0.16	-0.16	0.8
			T_{33}	0.84	0.85	0.84	0.84	0.85	0.84	0.8
			T_{11}	-0.69	-0.64	-0.62	-0.62	-0.62	-0.61	-0.27
		C-H$_3$	T_{22}	-0.43	-0.39	-0.37	-0.37	-0.37	-0.36	-0.27
			T_{33}	1.12	1.02	1.00	0.99	0.99	0.98	0.55
			T_{11}	-8.56	-8.47	-8.38	-8.38	-8.41	-8.40	-7.63
		N-**H**	T_{22}	-0.75	-0.51	-0.47	-0.47	-0.62	-0.47	-2.43

			T_{33}	9.31	8.99	8.85	8.85	9.03	8.88	10.05
		N-**H**	T_{11}	-7.33	-7.27	-7.19	-7.20	-7.22	-7.22	-6.76
			T_{22}	-1.00	-0.78	-0.79	-0.78	-0.90	-0.77	-2.72
			T_{33}	8.34	8.06	7.98	7.98	8.12	7.99	9.48
		C-**H**	T_{11}	-1.92	-1.93	-1.93	-1.93	-1.94	-1.93	-3.9
			T_{22}	-0.33	-0.33	-0.33	-0.33	-0.33	-0.33	1.1
			T_{33}	2.24	2.25	2.25	2.25	2.26	2.25	2.8
		C-**H**$_3$	T_{11}	-1.10	-1.08	-1.08	-1.08	-1.08	-1.08	-2.49
			T_{22}	-0.25	-0.26	-0.26	-0.26	-0.27	-0.26	0
			T_{33}	1.35	1.35	1.35	1.34	1.35	1.34	2.49
		H$_2$O	T_{11}	-1.91	-1.90	-1.90	-1.90	-1.89	-1.90	
			T_{22}	-0.14	-0.12	-0.11	-0.11	-0.10	-0.11	
			T_{33}	2.05	2.02	2.01	2.01	1.99	2.01	
GGA BP86	Gradient	**Cu**	T_{11}	-331.01	-342.52	-342.99	-343.38	-345.72	-343.87	
			T_{22}	96.85	98.32	98.41	98.35	99.74	98.22	
			T_{33}	234.16	244.20	244.58	245.02	245.98	245.64	
		Cu-**O**	T_{11}	17.23	17.01	16.80	16.76	17.14	16.73	
			T_{22}	15.91	15.89	15.76	15.72	16.06	15.65	
			T_{33}	-33.14	-32.90	-32.56	-32.47	-33.20	-32.38	
		C=**O**	T_{11}	4.21	3.93	3.91	3.89	3.92	3.87	2.39
			T_{22}	2.65	2.50	2.49	2.47	2.47	2.45	0.42
			T_{33}	-6.86	-6.43	-6.40	-6.37	-6.38	-6.31	-2.81
		H_2**O**	T_{11}	0.81	0.84	0.85	0.85	0.85	0.85	
			T_{22}	-0.40	-0.37	-0.37	-0.36	-0.36	-0.36	
			T_{33}	-0.41	-0.47	-0.48	-0.48	-0.48	-0.49	
		C=O	T_{11}	-2.99	-2.93	-2.91	-2.91	-2.92	-2.92	-3.3
			T_{22}	0.36	0.30	0.29	0.29	0.29	0.29	1.65

			T_{33}	2.63	2.63	2.62	2.62	2.63	2.62	1.65
		C-**C**-H	T_{11}	-0.96	-1.00	-1.02	-1.02	-1.02	-1.02	-1.6
			T_{22}	-0.26	-0.26	-0.26	-0.26	-0.25	-0.26	0.8
			T_{33}	1.22	1.26	1.27	1.28	1.26	1.28	0.8
		C-H_3	T_{11}	-1.17	-1.15	-1.15	-1.15	-1.14	-1.15	-0.27
			T_{22}	0.02	0.05	0.06	0.06	0.05	0.06	-0.27
			T_{33}	1.14	1.10	1.09	1.09	1.09	1.09	0.55
		N-**H**	T_{11}	-8.27	-8.27	-8.23	-8.24	-8.26	-8.27	-7.63
			T_{22}	-2.83	-2.84	-2.85	-2.86	-2.90	-2.86	-2.43
			T_{33}	11.10	11.11	11.08	11.09	11.16	11.13	10.05
		N-**H**	T_{11}	-9.54	-9.50	-9.45	-9.46	-9.47	-9.49	-6.76
			T_{22}	-0.71	-0.72	-0.74	-0.75	-0.80	-0.76	-2.72
			T_{33}	10.25	10.22	10.20	10.21	10.27	10.25	9.48
		C-**H**	T_{11}	-4.59	-4.69	-4.71	-4.72	-4.70	-4.73	-3.9
			T_{22}	-0.61	-0.63	-0.64	-0.64	-0.64	-0.64	1.1
			T_{33}	5.20	5.32	5.34	5.36	5.34	5.37	2.8
		C-**H**$_3$	T_{11}	-4.22	-4.30	-4.32	-4.32	-4.30	-4.33	-2.49
			T_{22}	0.86	0.89	0.90	0.90	0.89	0.91	0
			T_{33}	3.36	3.41	3.42	3.42	3.41	3.43	2.49
		H$_2$O	T_{11}	-5.10	-5.22	-5.23	-5.25	-5.20	-5.26	
			T_{22}	-1.21	-1.21	-1.21	-1.21	-1.20	-1.22	
			T_{33}	6.31	6.44	6.45	6.46	6.40	6.48	
	Density	**Cu**	T_{11}	-321.25	-332.13	-332.70	-333.06	-335.60	-333.49	
			T_{22}	132.47	135.09	135.28	135.24	137.02	135.11	
			T_{33}	188.78	197.04	197.42	197.82	198.57	198.38	
		Cu-**O**	T_{11}	17.26	17.04	16.83	16.79	17.18	16.76	
			T_{22}	15.59	15.56	15.43	15.38	15.73	15.31	

			T_{33}	-32.85	-32.60	-32.26	-32.17	-32.91	-32.07	
		C=**O**	T_{11}	3.90	3.58	3.57	3.55	3.58	3.52	2.39
			T_{22}	2.78	2.64	2.63	2.61	2.60	2.59	0.42
			T_{33}	-6.67	-6.22	-6.20	-6.16	-6.18	-6.11	-2.81
		H_2**O**	T_{11}	0.40	0.36	0.35	0.35	0.33	0.35	
			T_{22}	0.14	0.10	0.10	0.10	0.09	0.09	
			T_{33}	-0.54	-0.46	-0.45	-0.44	-0.43	-0.44	
		C=O	T_{11}	-2.42	-2.31	-2.29	-2.29	-2.30	-2.29	-3.3
			T_{22}	0.22	0.16	0.15	0.15	0.15	0.16	1.65
			T_{33}	2.19	2.15	2.14	2.13	2.15	2.13	1.65
		C-**C**-H	T_{11}	-0.66	-0.66	-0.66	-0.66	-0.67	-0.66	-1.6
			T_{22}	-0.16	-0.17	-0.17	-0.17	-0.17	-0.17	0.8
			T_{33}	0.82	0.83	0.83	0.83	0.84	0.83	0.8
		C-H_3	T_{11}	-0.70	-0.65	-0.64	-0.63	-0.63	-0.63	-0.27
			T_{22}	-0.43	-0.39	-0.38	-0.37	-0.37	-0.37	-0.27
			T_{33}	1.14	1.03	1.02	1.01	1.01	0.99	0.55
		N-**H**	T_{11}	-8.49	-8.37	-8.31	-8.31	-8.35	-8.33	-7.63
			T_{22}	-0.60	-0.35	-0.32	-0.32	-0.47	-0.32	-2.43
			T_{33}	9.09	8.72	8.63	8.63	8.82	8.65	10.05
		N-**H**	T_{11}	-7.37	-7.29	-7.23	-7.23	-7.27	-7.26	-6.76
			T_{22}	-0.96	-0.73	-0.73	-0.72	-0.84	-0.72	-2.72
			T_{33}	8.34	8.02	7.96	7.96	8.11	7.97	9.48
		C-**H**	T_{11}	-1.85	-1.85	-1.85	-1.85	-1.86	-1.86	-3.9
			T_{22}	-0.32	-0.32	-0.32	-0.32	-0.32	-0.32	1.1
			T_{33}	2.16	2.17	2.17	2.17	2.18	2.17	2.8
		C-**H**$_3$	T_{11}	-1.09	-1.08	-1.07	-1.07	-1.07	-1.07	-2.49
			T_{22}	-0.22	-0.23	-0.23	-0.23	-0.24	-0.23	0

			T_{33}	1.31	1.31	1.31	1.31	1.31	1.30	2.49
			T_{11}	-1.98	-1.97	-1.97	-1.97	-1.96	-1.97	
		H$_2$O	T_{22}	-0.04	-0.02	-0.02	-0.02	-0.01	-0.02	
			T_{33}	2.02	1.99	1.99	1.99	1.97	1.99	

[a]Results are averaged from all equivalent positions. [b] All values are reported in MHz.